Polyploid cardiomyocytes define disease-specific transcriptional states in the mammalian heart

Authors: Paul Kiessling[1#], Mehdi Joodaki[2,3#], Daryna Pikulska[1#], Emilia Scheidereit[1#], Giulia Cesaro[4#], Mayra Ruiz[2,3], Damin Kühn[3,5], Kai Peng[2,3], Osman Goni[1], Sebastian Foecking[1], Samaneh Samiei[1], Xian Liao[1], Kai Li[1], Zihao Feng[1], Delin Wang[1], Lampros Mavrommatis[1], Anna-Maria Vllaho[1], Merwan Rombach[1], Giulia Cucinella[1], Mingbo Cheng[2], Till Lautenschläger[6,7,8], David Rodriguez Morales[6,7,8], Rogier J. A. Veltrop[9,10,11,12,13], Leon J. Schurgers[1,9], Moritz von Scheidt[14,15], Barbara Mara Klinkhammer[16], Florian Kahles[17], Jennifer Kranz[18,19], Aitor Aguirre[20], Anne Loft[21,22], Niklas Klümper[23,24], Markus Eckstein[25], Thomas Seidel[26], Giancarlo Forte[27,28,29], Rik Westland[30], Man Zhang[31], Heng Zhao[31], Feng Ren[31,32], Sikander Hayat[1,33,34], Junedh Amrute[35] , Benjamin Kopecky[36], Rebekka K. Schneider[37,38,39], Hind Medyouf[40], Pierre-Louis Tharaux[41], Peter Boor[16], Rafael Kramann[1,42], Linda W. van Laake[43], Annelotte Vos[44], Bernadette S. de Bakker[45,46], Jermo Hanemaaijer-van der Veer[45,46], Kory Lavine[35], Nikolaus Marx[17], Karin Klingel[47], Michael T. Schaub[3,5, 48], Stefanie Dimmeler[6,7,8], Alex Zhavoronkov[31,32, 49], Hendrik Milting[50*], Ivan Costa[2,3*] and Christoph Kuppe[1,3,9*]

Affiliations:

[1]Division of Nephrology and Clinical Immunology, RWTH Aachen University, Medical Faculty, Aachen, Germany.
[2]Institute of Computational Genomics, RWTH Aachen University, Medical Faculty, Aachen, Germany.
[3]Center for Computational Life Sciences, RWTH Aachen University, Aachen, Germany
[4]Department of Information Engineering, University of Padova, Padova, Italy
[5]Department of Computer Science, RWTH Aachen University, Aachen, Germany.
[6]Institute of Cardiovascular Regeneration, Goethe University Frankfurt, Frankfurt am Main 60590, Germany.
[7]German Center for Cardiovascular Research (DZHK), Partner Site Rhine-Main, Germany.
[8]Cardio-Pulmonary Institute (CPI), Frankfurt, Germany.
[9]Department of Biochemistry, Cardiovascular Research Institute Maastricht (CARIM), Maastricht University, Maastricht, the Netherlands
[10]Department of Cardiology, Division of Heart and Lungs, University Medical Center Utrecht, Utrecht University, Heidelberglaan 100, 3584 CX Utrecht, The Netherlands.
[11]Regenerative Medicine Center Utrecht and Circulatory Health Research Center, University Medical Center Utrecht, Utrecht University, Heidelberglaan 8, 3584 CS Utrecht, The Netherlands.
[12]LMNAcardiac.org, LMNA Patient Organization, Vredehofstraat 13761, HA Soest, The Netherlands.
[13]Netherlands Heart Institute, Holland Heart House, Moreelsepark 1, 3511 EP Utrecht, The Netherlands.
[14]Department of Cardiology, TUM Klinikum Deutsches Herzzentrum, Technical University Munich, Munich, Germany.
[15]Deutsches Zentrum für Herz- und Kreislaufforschung (DZHK), Partner Site Munich Heart Alliance, Munich, Germany.
[16]Institute of Pathology, RWTH Aachen University Hospital, Aachen, Germany.
[17]Department of Internal Medicine I-Cardiology, University Hospital Aachen, RWTH Aachen University, Pauwelsstraße 30, D-52074 Aachen, Germany.
[18]Department of Urology and Pediatric Urology, University Hospital RWTH Aachen, Aachen, Germany
[19]Department of Urology and Kidney Transplantation, Martin-Luther-University, Halle, Germany

[20]Institute for Quantitative Health Science and Engineering, Michigan State University, East Lansing, MI, USA; Department of Biomedical Engineering, Michigan State University, East Lansing, MI, USA.
[21]Center for Functional Genomics and Tissue Plasticity (ATLAS), Department of Biochemistry and Molecular Biology, University of Southern Denmark (SDU), Odense, Denmark.
[22]The Novo Nordisk Foundation Center for Genomic Mechanisms of Disease, Broad Institute of MIT and Harvard, Cambridge, MA, USA.
[23]Department of Urology and Pediatric Urology, University Hospital Bonn, Bonn, Germany.
[24]Institute of Experimental Oncology, University Hospital Bonn, Bonn, Germany.
[25]Institute of Pathology, Universitätsklinikum Erlangen, Friedrich-Alexander-Universität Erlangen-Nürnberg (FAU), Erlangen, Germany; Comprehensive Cancer Center Erlangen-EMN (CCC ER-EMN), Erlangen, Germany; Comprehensive Cancer Center Alliance WERA (CCC WERA), Erlangen, Germany; Bavarian Cancer Research Center (BZKF), Erlangen, Germany.
[26]Institute of Cellular and Molecular Physiology, Friedrich-Alexander-Universität Erlangen-Nürnberg, Erlangen, Germany.
[27]International Clinical Research Center (ICRC), St Anne's University Hospital, Brno, Czech Republic.
[28]Faculty of Medicine, Masaryk University, Brno, Czech Republic.
[29]School of Cardiovascular and Metabolic Medicine and Sciences, King's College London, London, UK.
[30]Department of Pediatric Nephrology, Amsterdam UMC-Emma Children's Hospital, Location University of Amsterdam, Meibergdreef 9, 1105 AZ, Amsterdam, The Netherlands.
[31]Insilico Medicine Shanghai Ltd., Shanghai, China.
[32]Insilico Medicine Hong Kong Ltd., Hong Kong SAR, China.
[33]Cardiovascular Research Institute and Department of Medicine, Icahn School of Medicine at Mount Sinai, New York, NY, USA
[34]Windreich Department of Artificial Intelligence and Human Health, Icahn School of Medicine at Mount Sinai, New York, NY, USA
[35]Center for Cardiovascular Research, Division of Cardiology, Department of Medicine, Washington University in St. Louis School of Medicine, St. Louis, MO, USA
[36]Department of Medicine, Division of Cardiology, University of Colorado Anschutz Medical Campus, Aurora, CO, USA.
[37]Department of Developmental Biology Erasmus Medical Center Rotterdam The Netherlands.
[38]Oncode Institute Erasmus Medical Center Cancer Institute Rotterdam The Netherlands.
[39]Department of Cell and Tumor Biology, Faculty of Medicine University Hospital RWTH Aachen Aachen Germany.
[40]Department of Hematology, Oncology, Hemostaseology, Stem Cell Transplantation, Medical Faculty, Center for Integrated Oncology (CIO) RWTH Aachen University Aachen Germany.
[41]Université Paris Cité, INSERM, Paris Cardiovascular research Center (PARCC), Paris, France
[42]Department of Internal Medicine, Nephrology and Transplantation, Erasmus Medical Center, Rotterdam, The Netherlands.
[43]Department of Cardiology, Division of Heart & Lungs, University Medical Centre Utrecht and Utrecht University, Utrecht, the Netherlands
[44]Department of Pathology, University Medical Center Utrecht, Utrecht, The Netherlands.
[45]Amsterdam UMC location University of Amsterdam, Dept. of Obstetrics and Gynecology, Amsterdam, The Netherlands
[46]Amsterdam Reproduction and Development research institute, Amsterdam, The Netherlands
[47]Cardiopathology, Institute for Pathology and Neuropathology, University Hospital Tübingen, Tübingen, Germany.
[48]Department of Biology, RWTH Aachen University, Aachen, Germany.
[49]Insilico Medicine US Inc., Cambridge, MA, USA.
[50]Heart- and Diabetescenter NRW, Erich and Hanna Klessmann-Institute for Cardiovascular Research and Development, University Hospital of the Ruhr University Bochum, Georgstr. 11, 32545, Bad Oeynhausen, Germany.

#co-first authors, *co-senior authors
Correspondence to:
Ivan Costa, PhD

Institute of Computational Genomics
Medical Faculty RWTH Aachen University,
Pauwelsstrasse 30, 52074 Aachen, Germany
Phone: +49-241-80-89760
E-mail: igesteiracostafilho@ukaachen.de

Christoph Kuppe, MD, PhD
Division of Nephrology and Clinical Immunology,
Medical Faculty RWTH Aachen University,
Pauwelsstrasse 30, 52074 Aachen, Germany
Phone: +49-241-80-37308
E-mail: christoph.kuppe@googlemail.com

Abstract

The adult mammalian heart has a limited regenerative capacity. Following injury, cardiomyocytes undergo a hypertrophic response accompanied by polyploidization, which has been described as a barrier to proliferation and regeneration of the heart[1,2]. However, the unique molecular programs of polyploidy, or genome multiplied cardiomyocytes, and their influence on the disease-related myocardial remodelling process remains unclear. Here, we integrate single-nuclei and high-resolution spatial multi-omics across human, rat, and mouse hearts to define novel cardiac cell states and their tissue niches in ischemic and non-ischemic heart disease. Computational analysis across scales allowed us to generate detailed networks of the cardiac tissue remodelling process as well as tissue and sub-cellular environments uniquely enriched in polyploid cardiomyocytes or their diploid origins. We identify a conserved, dichotomous transcriptional program distinguishing diploid from polyploid cardiomyocytes. Polyploid cardiomyocytes demonstrated rewired metabolic and chromatin-remodeling transcriptional programs and recapitulate the gene signature of immature human fetal cardiomyocytes. Importantly, they showed selective enrichment for established heart-failure therapy targets including the mineralocorticoid receptor, β1-adrenergic receptor, and glucagon-like peptide-1 receptor. We further identified TNIK, a Wnt-pathway regulator expressed in polyploid cardiomyocytes across species, as a potential therapeutic target and demonstrate that pharmacological TNIK inhibition improves cardiac function after myocardial infarction in rats. Together, this species-spanning, disease-resolved study redefines cardiomyocyte heterogeneity in heart disease and suggests a therapeutic path to heart failure treatment by targeting polyploid cardiomyocytes.

Results

Heart failure represents a major global health burden, affecting nearly half a billion individuals worldwide and causing more deaths than most forms of cancer[3]. Despite significant treatment advancements, current therapies typically address the symptoms and systemic consequences of heart failure, but do not directly target maladaptive or regenerative cardiac disease pathways[4]. The human heart possesses a minimal intrinsic regenerative capacity[5] compared to other species such as zebrafish[6] and neonatal mice[7]. Human cardiomyocytes (CMs) originate from proliferative mesodermal precursors during embryogenesis but rapidly lose their regenerative capacity shortly after birth, coinciding with a metabolic shift from glycolysis to fatty acid oxidation and the initiation of polyploidization[1,8,9]. The adult human heart predominantly responds to injury with maladaptive remodeling, stress-associated gene activation, concomitant fibrosis, and progressive functional loss[10,11]. This stress response is typically associated with upregulated expression of the genes NPPB and NPPA, which are co-regulated by an evolutionarily conserved enhancer cluster[12,13] and induced by mechanical stress. Recent studies suggest that metabolic perturbations, specifically inhibition of fatty acid oxidation, induce a fetal cell state shift in CMs and can induce cardiomyocyte proliferation and regeneration highlighting the influence of metabolic states on cardiomyocyte cell state plasticity[14]. It remains unclear whether additional CM cell states, beyond the NPPB/NPPA stress-response, exist in the human heart, which could potentially drive cardiac tissue remodelling.

Polyploidization, characterized by increased genome copy numbers or multinucleation in cardiomyocytes, emerges postnatally as the heart matures[15]. It represents a fundamental cell growth principle in biology, utilized by different organisms and is common in plants and in salivary glands of insects[16–18]. Polyploid cell types can be found in various tissues, including heart[19], muscle[20], liver[21] and pancreas[22] and have been suggested to play a role in tissue repair and regeneration[21]. While several mechanisms like cell fusion, mitotic slippage, and endocycling have been identified as polyploid mechanisms, endocycling has been identified as the major mechanism in the heart, which is particularly linked to mitochondrial function[23]. Polyploidization has been hypothesized to serve as a barrier to CM proliferation, thereby limiting cardiac regeneration[2]. This appears paradoxical given that polyploidy is beneficial in other organs, such as the liver[24], where it supports tissue regeneration[24] and protects against genotoxic stress[25,26]. Despite extensive research[27], the functional and molecular distinctions between diploid and polyploid cardiomyocytes in the mammalian heart, especially regarding their disease-modifying relevance in the human heart, have remained elusive.

Here, we present a single-cell and spatial multi-omics analysis of over 4.5 million cardiac cells from healthy and diseased hearts across 105 human, 16 rat, and 16 mouse donors.

182 This includes a temporal map of mouse myocardial infarction (MI) and the evaluation of
183 a novel therapeutic approach targeting polyploid CMs in a rat model. Selection of samples
184 was performed based on pathologist assessment and aided by the UNI vision
185 transformer[28]. Samples were measured using probe-based single-nucleus (snRNA, Flex
186 - 10x Genomics) and spatial transcriptomics (MERFISH - Vizgen and Xenium - 10x
187 Genomics) techniques using fixed-frozen or formalin-fixed paraffin-embedded (FFPE)
188 cardiac tissue. An advanced computational framework exploring histology and sample
189 level spatial information identified several novel disease-associated cell states and
190 profibrotic tissue niches in ischemic and non-ischemic heart disease. To take full
191 advantage of the subcellular resolution of our spatial transcriptomic measurements, we
192 studied patterns in the position of individual transcripts across cardiomyocytes. We
193 identify multiple cell state-specific subcellular patterns, among others a specific signature
194 enriched in the intercalated disk (ICD) region, the cardiomyocyte-cardiomyocyte
195 interface. In summary, our study provides a high-resolution, cross-species dataset that
196 distinguishes polyploid from diploid CM states, resolves their interactions with other
197 cardiac cell types, and delineates the regulatory networks underlying myocardial
198 remodeling in ischemic and non-ischemic failing human myocardium. Based on our data,
199 we identify polyploid CMs as key regulators of maladaptive cardiac remodelling and TNIK
200 (TRAF2 and NCK interacting kinase), selectively expressed in polyploid CMs, as a novel
201 therapeutic target in cardiac remodelling.

202 **Spatial multi-omics analysis of human heart disease**

203 To characterize cellular heterogeneity and tissue remodelling in ischemic and non-
204 ischemic human heart disease, we analysed heart tissue of 105 adult and fetal human
205 donors and 16 rat and mouse samples each (**Fig. 1a-c**), using snRNA-seq (Flex) and
206 high-resolution spatial transcriptomics (ST; MERFISH/Xenium) (**Fig. 1d**, **Extended Data**
207 **Fig. 1a-b; Supplementary Table 1**). In total, the snRNA-seq dataset includes 997,362
208 nuclei and the ST dataset 3,593,941 nuclei (**Fig. 1d**). Human samples were obtained from
209 left ventricular and septal walls, encompassing controls from non-failing donor hearts and
210 patients with ischemic cardiomyopathy (ICM), non-ischemic dilated cardiomyopathy
211 (DCM) of idiopathic etiology, and acute myocardial infarction (ICM_AMI) to capture a wide
212 range of tissue remodelling dynamics (**Supplementary Table 1**). The tissue specimens
213 were collected at heart transplantation or during implantation of a cardiac assist device.
214 The five fetal heart tissue samples were obtained from human fetuses from terminated
215 pregnancies between 12 and 21 post-conception weeks (p.c.w.) (**Fig. 1a**) from the Dutch
216 Fetal Biobank. In addition, we analyzed heart tissues following drug treatment during the
217 cardiac tissue remodelling phase (**Fig. 1b)** in rats (total n=52, n=16 for snRNA-seq) and
218 following myocardial infarction (MI) at five different time points (**Fig. 1c, Extended Data**
219 **Fig. 1a; Supplementary Table 1**) in mice (n=16, snRNA-seq + Xenium). For each cardiac
220 sample, we obtained a 25 µm tissue section from either fixed-frozen or FFPE tissue

specimens for nuclei isolation. We optimized our probe-based snRNA-seq isolation protocol to achieve high data quality and the lowest possible background from ambient RNA. 5 µm tissue sections were sectioned for high-resolution spatial transcriptomics (**Fig. 1d**, **Methods**). From each sample, an H&E staining was performed and evaluated by an expert cardiac pathologist.

For snRNA dataset annotation we followed a two-step approach. An initial graph-based clustering[29] and annotation based on marker genes resulted in the annotation of 20 major cell types across the three datasets (**Supplementary Table 2**). Each major cell type was then subclustered into detailed dataset-specific cell states with a focus on cross-species cardiomyocyte diversity (**Fig. 1e-g**, **Supplementary Fig. 1-3)**. Our snRNA-seq data contained a median of 2,358 UMIs and 1,403 detected genes per nucleus for the adult human, 1,190 UMIs and 612 detected genes per nucleus for rat, and 1,512 UMIs and 1,051 detected genes per nucleus for mouse (**Supplementary Table 2**).

Altogether, our cross-species snRNA data identified several novel CM cell states, as well as cell types not captured in previous studies, such as neutrophils (**Fig. 1e-g**). The enhanced recovery originates from a nuclei-isolation protocol optimized for fixed heart tissue that reduces ambient-RNA bias and minimizes loss of nuclei with atypical morphology (e.g., neutrophils)[30,31]. While the transcriptomic complexity (genes detected per UMI) was comparable to our previous polyA-3'-enriched snRNA dataset[11], our new data achieves substantially higher gene detection rate (up to 14,452 genes vs 6,202 genes) and deeper sequencing coverage (2,534 vs 2,117 median UMIs per cell), indicating improved capture efficiency and transcriptome sampling (all values for the human dataset, **Extended Data Fig. 1c)**.

Marker gene analysis identified two primary CM clusters conserved across three mammalian species, each containing distinct subclusters (**Fig. 1e-h**). The first major group was characterized by *DES* expression and included two specific CM subpopulations: one defined by *NPPA* and *NPPB* expression, and another human-specific subcluster defined by *DES*$^{+}$/*SYNPO*$^{+}$ expression. These *DES*$^{+}$/*SYNPO*$^{+}$ CMs displayed a transcriptional program enriched for cytoskeletal remodeling genes—including *SYNPO*, *SYNPO2L*, and *SYNPO2*—alongside increased *TAZ* (*WWTR1*) expression, consistent with a mechano-adaptive, disease-associated state (**Extended data Fig. 1d**). The second major CM group was defined by the expression of *CFLAR* and *MYH7B* (or *Myh7b* in rodents). *MYH7B* represents an ancient member of the myosin heavy chain motor protein family, and its expression has not previously been described in a unique adult human CM subpopulation[32]. Unlike the alpha and beta myosin heavy chains (encoded by *MYH6* and *MYH7*), *MYH7B* does not produce a full-length protein due to

261 post-transcriptional exon-skipping[33]; instead, it functions as a long non-coding RNA that
262 regulates the ratio of alpha to beta myosin heavy chains and modulates the expression
263 of other sarcomeric genes[32]. Within this second group, we also identified a small, human-
264 specific subfraction of CMs expressing *HAND2*, a cardiac-enriched transcription factor
265 essential for lineage specification during development whose reactivation in adult cells is
266 linked to stress- and remodeling-associated gene programs. *CFLAR* (also known as c-
267 FLIP), an apoptotic regulator with a reported role in beneficial cardiac remodeling[34],
268 serves as an additional key marker for this novel CM group in humans (Fig. 1h). Notably,
269 these novel CM states were not detectable in two previously published datasets[11,35]
270 utilizing polyA-3' snRNA technology (**Extended data Fig. 1e-f**), highlighting the technical
271 sensitivity required to resolve these populations.

272 In human hearts, CMs were approximately evenly distributed between the CFLAR$^+$ and
273 DES$^+$ groups at the cohort level, however, substantial inter-individual variability was
274 observed. Across patients, the percentage of CFLAR$^+$ CMs ranged from 20% to 80%.
275 (**Extended Data Fig. 1g**). The proportion of CFLAR$^+$ CM was higher in ICM and DCM
276 than in ICM_AMI (**Extended Data Fig. 1g**). Notably, variation in the CFLAR$^+$/DES$^+$
277 distribution was not associated with clinical measures of cardiac function, including left
278 ventricular ejection fraction (Spearman's $\rho = 0.23$, $p = 0.17$, $n = 36$) or left-ventricular end-
279 diastolic diameter (LVEDD) (Spearman's $\rho = -0.27$, $p = 0.10$, $n = 36$), in samples with
280 available metadata.

281 To further resolve disease-associated compositional changes, we analyzed cell
282 abundance shifts in our human snRNA data (**Extended Data Fig. 1h**). ICM_AMI samples
283 exhibited a pronounced increase in immune cell populations, including SPP1$^+$
284 macrophages, monocytes, plasma cells, and mast cells, alongside expansion of
285 myofibroblasts and CTHRC1$^+$ fibroblasts (**Extended Data Fig. 1h)**. CM sub-states also
286 showed disease-specific remodeling patterns. CFLAR$^+$ cardiomyocytes were significantly
287 expanded in ICM and DCM, whereas ICM_AMI was characterized by a reduction of
288 multiple CMs states, including DES$^+$, SLC25A4$^+$, and specific CFLAR$^+$ CM substates (0,
289 3, and 4) (**Extended Data Fig. 1h**). Additionally, perivascular and ELN$^+$ fibroblasts
290 increased significantly only in ICM and DCM, while in ICM_AMI myofibroblast and
291 CTHCR1$^+$ fibroblasts were significantly increased, highlighting divergent stromal
292 remodeling programs between chronic and acute cardiac injuries (**Extended Data Fig.
293 1h**).

294 We used consecutive FFPE sections to perform spatial transcriptomic experiments with
295 probe sets covering 500 (MERFISH) or up to 5,100 (Xenium) genes (**Extended Data
296 Fig.1b**). Panel design was based on multiple publicly available datasets (**Methods**). In
297 larger cells like cardiomyocytes, this allowed us to recover up to 10,000 transcripts per

cell, while across all cell-types 175 to 306 median genes per segmented cell/nuclei were detected (**Fig. 1i-j**, **Extended data Fig. 2a**). Out of 150 biosamples (human, mouse and rat), some 50% were measured in both snRNA and spatial modalities (**Extended Data Fig. 1a**).

Segmentation of CMs is an unsolved challenge, impeded by their elongated and irregular shape. We fine-tuned a Cellpose[36] model based on expert annotated sections of our MERFISH data. This approach demonstrated superior performance relative to other state-of-the-art algorithms (**Extended Data Fig. 2b-c; Methods)**. Due to the lower signal-to-noise ratio of cell membrane staining in Xenium, we opted for nuclei segmentation using CellPose for the processing of those samples (**Extended Data Fig. 2d)**. For our subcellular analysis of one tissue microarray (TMA) with 26 samples, we performed a post-Xenium IF staining with wheatgerm agglutinin (WGA)[37] and DAPI, which allowed us to confidently segment cells and nuclei (**Extended data Fig. 2e**).

We annotated each spatial dataset by transferring cell state labels from the corresponding species-matched snRNA-seq dataset. To ensure robust annotations, we used five state-of-the-art label transfer tools[38–42] and assigned each cell the label predicted by the majority of tools. The level of disagreement between tools served as a measure of annotation confidence, indicating which cell states could be reliably distinguished in the spatial data despite capturing only a fraction of the genes measured in the whole-transcriptome snRNA-seq datasets. When tools disagreed, cell types were merged into broader categories until at least three out of five tools agreed. This resulted in comparable cell type proportions between the spatial and snRNA-seq datasets from the same donor (Spearman's $\rho > 0.8$).

The inclusion of histology (e.g., H&E staining) provided an additional modality that enabled an integrative, cross-species analysis of the spatial data (**Fig. 1i+j**). To analyze the H&E stainings, we employed a deep learning model specialized in heart tissue[28]. We divided the images into small patches and used the model to classify them based on their histological features (**Extended Data Fig. 3a**). This method successfully distinguished several specific tissue compartments, effectively bridging the analysis between human and mouse samples (**Extended Data Fig. 3b**). The identified tissue compartments effectively captured the transition from the healthy heart (myocardium, adipose tissue) through stress (damaged myocardium 1,2 and 3), major damage (fresh infarct with demarcation,granulation tissue, necrotic tissue) and chronic damage (fibrotic tissue, scar tissue) (**Fig. 1i,Extended Data Fig. 3b**).

While the majority of tissue compartments were consistent with the pathologist's annotation, we observed patch sub-clusters (damaged myocardium 1, 2 and 3), that were

338 not readily identifiable by the experts (**Extended Data Fig. 3c**). To uncover compositional
339 differences we related the cell types identified in our spatial transcriptomic measurement
340 (Xenium measurement of human TMAs) to the H&E-derived annotation. We detected
341 differences in the CM composition of different areas (**Fig. 1k**). While CFLAR$^+$ CMs were
342 enriched in myocardium, damaged myocardium 1 and granulation tissue, DES$^+$ CMs
343 enriched in damaged myocardium 2 together with DES-SYNPO$^+$ CMs, which were also
344 found in fibrotic and scar tissue regions. NPPA-NPPB$^+$ CMs (border-zone stressed
345 cardiomyocyte signature) were found in high levels in the patches annotated as
346 myocardium damaged 3 in both human and mouse. We could identify an enrichment of
347 immune cells (macrophages, monocytes) in the fibrotic and granulation tissue (**Extended**
348 **Data Fig. 3d**). Myofibroblasts were localized especially in damaged myocardium 2 and 3
349 and fibrotic scar tissue regions. Comparing the different disease groups (ICM_AMI, ICM,
350 DCM) we were able to identify an enrichment of myocardium and damaged myocardium
351 1 in controls whereas damaged myocardium 3 was enriched in DCM as well as
352 fibrotic/scar tissue (**Fig. 1l**). Quantitative analysis of nearest-neighbor counts revealed
353 that DES+ cardiomyocytes form more cohesive spatial clusters, while CFLAR+
354 cardiomyocytes are more spread out (**Extended Data Fig. 3e**), supporting the model of
355 distinct spatial patterning of CM states in the diseased human myocardium (MERFISH v2
356 data, n=13).
357
358 Together, these analyses establish a spatially resolved, cross-species dataset integrating
359 single-nucleus transcriptomics, spatial gene expression, and histology-based tissue
360 annotation. We identify novel CM (CFLAR$^+$, DES$^+$, DES-SYNPO$^+$, SLC25A4$^+$) beyond
361 the established stressed NPPA-NPPB$^+$ CM state. By anchoring transcriptomic states to
362 specific morphological zones—ranging from healthy myocardium to chronic scar—we
363 demonstrate that novel CM states (CFLAR$^+$, DES$^+$, etc.) are not transient signatures but
364 are tied to specific stages of pathological remodeling.

365 **Spatial niches of human heart disease**

366 While the histology-based compartments provided a macro-scale framework of tissue
367 injury, they represent broad morphological zones rather than precise functional units.
368 Cellular colocalization serves as a proxy for the complex communication networks that
369 operate at different length scales to maintain homeostasis or drive pathology. To bridge
370 the gap between these large-scale regions and cellular behavior, we moved from tissue
371 compartments to spatial niches—repeating tissue structures with co-localized cells—and
372 characterized how they differed across patients and disease conditions (ICM_AMI, ICM,
373 or DCM).
374 We performed a sample level cell–cell colocalization analysis using a framework
375 combining NicheSphere and PILOT[43] (**Extended Data Fig. 4a, Methods**). We identified
376 six distinct niches in the cell interaction networks in the contrast control vs. ICM samples

(**Fig. 2a**). Similar to the H&E spatial data analysis, our spatial transcriptomic analysis revealed that CM states were localized in separate niches e.g. CFLAR$^+$ and SLC25A4$^+$ CM together with macrophages, pericytes and lymphatic endothelial cells in niche 4. Cells comprising this niche, characteristic of healthy myocardium, showed diminished spatial colocalization in ICM. Regarding niches with increased colocalization in ICM, niche 3 includes CM cell states (DES$^+$, NPPA_NPPB$^+$ and DES_Synpo$^+$). Niche 1 includes myofibroblasts clustered together with proinflammatory macrophages, monocytes and and fibroblasts forming a unique profibrotic and proinflammatory tissue niche (**Fig. 2a**). Focusing on colocalization statistics associated with the different novel CM subtypes, only myofibroblasts increase their colocalization with all CM subtypes (**Fig. 2b**). However we also noted distinct differences between CFLAR$^+$ and SLC25A4$^+$ CMs compared to the other CMs. These CM states lost their colocalization to macrophages, pericytes and mast cells,, whereas DES_SYNPO$^+$ CMs uniquely increased their localization to tissue resident macrophages (**Fig. 2b**). We next compared the spatial niches (based on spatial transcriptomics) with our identified patch clusters (based on H&E staining) and observed strong concordance between the two approaches. (**Extended Data Fig. 4b**). The niche 4 (CFLAR+,SLC25A4+ CMs) was related to healthy myocardium, whereas niche 3 (DES,NPPA-NPPB-CMs) was significantly enriched in damaged myocardium 1-3 (**Extended Data Fig. 4b**). By resolving the cellular neighborhoods of each CM state, we demonstrate that cardiac remodeling involves the formation and dissolution of specific multicellular niches: loss of homeostatic CFLAR$^+$/SLC25A4$^+$-macrophage-pericyte networks in ICM parallels emergence of profibrotic DES$^+$/myofibroblast assemblies, revealing niche-level reorganization as a hallmark of disease progression.

To study the dynamical changes of spatial niches, we performed a sample level trajectory analysis using PILOT (**Fig. 2c**). A statistical analysis on niche changes over the trajectory indicated a decline of niche 4 (CFLAR myocardium) and expansion of niches 1,2,5 (macrophage, myofibroblast, lymphoid cell, and resident immune niches), as well as a transient increase of niche 3 with DES-CMs (**Fig. 2d; Extended Data Fig. 4c**). Selected cores display changes in niche, patches, cells and genes among the disease trajectory (**Fig. 2e)**. For example, CCDC80 was identified as a gene with a significant increase in expression in PILOT's trajectory for fibroblasts and myofibroblast cells (**Fig. 2e**). We further found this gene was highly expressed in fibroblasts (not shown) particularly in the CTHRC1$^+$ fibroblast subpopulation in the snRNA-seq data **(Extended data Fig. 4d)**. Other trajectory-related genes for CFLAR-CMs include CM contractile genes (*TNNT2*, *MYBPC3*) showing a reduction, whereas *TTN*, *PDE4DIP* and *DST* have an increased expression during disease progression (**Fig. 2e; Extended data Fig. 4e**). Thus, PILOT trajectory analysis reveals that CFLAR$^+$ CMs in ICM undergo a transition from a sarcomere-rich contractile state toward a stress-adaptive, cytoskeletal, and ECM-anchored (extracellular matrix) phenotype (based on the DST and PDE4DIP gene

417 changes)[44,45] which is accompanied by increasing activation and presence of ECM-
418 secreting fibroblast subsets.
419
420 Comparing controls vs. DCM we identified five cardiac tissue niches (**Extended data Fig.**
421 **4f-h**). Two niches had similar cell types and changes to ICM niches, i.e. decrease in
422 colocalization of cells in the CM-rich CFLAR myocardium (niche 4) and increase of
423 colocalization of cells in myofibroblast and macrophages (niche 2) (**Extended Data Fig.**
424 **4f**). However, our analysis revealed that the DES_Synpo$^+$ CM state constituted their own
425 cardiac niche in DCM with endothelial and dendritic cells (niche 3) (**Extended data Fig.**
426 **4f-g**). Similar to ICM, all CMs increased their spatial colocalization with myofibroblasts
427 (**Extended Data Fig. 4g**). Interestingly, the DES_Synpo$^+$ CMs demonstrated more spatial
428 interactions with other cell-types compared to ICM, indicating a potential unique role in
429 DCM. Moreover, in DCM samples, niche 3 with DES-SYNPO$^+$ CM was highly enriched in
430 fibrotic tissue patches (**Extended Data Fig. 4i**). A visual inspection of the distribution of
431 niches in ICM vs DCM samples (**Fig. 2e vs Extended Data Fig. 4j**) indicates that ICM
432 niches cover larger and uniform areas, while DCM niches are more scattered and small,
433 which suggest a more gradual and fine course cellular remodelling process in DCM**.** In
434 CFLAR$^+$ CMs of contrast control vs. DCM samples, mature contractile genes (*TNNT2*,
435 *MYBPC3*) decline early as in ICM (**Extended Data Fig. 4k**), while *TTN*, *OBSCN* and the
436 NMD kinase *SMG1* increase, indicating a CM-intrinsic program of sarcomere scaffold
437 realignment. Comparative niche analysis (ICM vs. DCM) demonstrates conserved
438 localization of CFLAR$^+$ and NPPA_NPPB$^+$ CMs in distinct cardiac tissue niches across
439 cardiomyopathy etiologies, contrasted by disease-specific redistribution of DES-SYNPO$^+$
440 CM states (**Extended Data Fig. 5a**). For the controls vs. ICM_AMI contrast, we detected
441 six tissue niches using NicheSphere (**Extended Data Fig. 5b**). Niche 1 contained all CM
442 substates and represented the niche losing colocalization interactions across other cell
443 types (**Extended Data Fig. 5b**). Interestingly, an increased colocalization is observed
444 between myofibroblasts and CFLAR$^+$ CM cells as in other contrasts (**Extended Data Fig.**
445 **5b**). Among the niches with increased colocalization in ICM_AMI condition, we also
446 observe a fibrotic niche (niche 4) and a tissue resident (niche 6) with increase in ICM_AMI
447 (**Extended Data Fig. 5d**). The latter niche included SPP1$^+$ tissue-resident macrophages,
448 which represent the cell type with the highest amount of ICM_AMI specific interactions,
449 recapitulating our previous findings[11].

450 **Subcellular features of human cardiomyocytes**

451 Next we analyzed the subcellular localization patterns of RNA molecules across individual
452 human CMs using BENTO[46]. An initial unsupervised clustering revealed four distinct sub-
453 cellular domains, micrometer-scale, recurring expression patterns **(Fig. 2f-j).** Enrichment
454 analysis of these domains based on known subcellular organelle mRNA signatures from
455 APEXseq[47] confirmed a nuclear (domain 1), perinuclear (domain 3), and two cytoplasmic

456 domains (domain 2, 4) **(Fig. 2f-h, Extended Data Fig. 5e).** The two cytoplasmic domains
457 were enriched for very different mRNA molecules (**Fig. 2i-j, Extended Data Fig. 5e**). We
458 hypothesized that the cytoplasmic domain 2 could correspond to CMs-CMs cell contacts,
459 the area where the ICD supports the synchronized contraction of the heart also based on
460 previous reports[48]. This CM-CM junction specificity was confirmed by overlay with WGA
461 CM cell boundary staining (**Fig. 2h-h', Extended Data Fig. 5e-h**). The ICD domain was
462 enriched with genes related to membrane-cytoskeleton linkage like *CMYA5*, an important
463 regulator of the cardiac dyad architecture[49] (**Extended data Fig. 5h**). Notably, the RNA-
464 level presence of the RNA-binding protein *SAMD4A*[50] and of the translation initiation
465 factor *EIF3A*[51] is consistent with localized post-transcriptional regulation and translational
466 activity, raising the possibility of spatially organized protein synthesis in proximity to the
467 ICD **(Fig. 2i)**. After identifying genes with specific subcellular expression patterns we
468 explored their expression levels in our human snRNA data (**Fig. 2k**). Our analysis shows
469 an enrichment of ICD-related (domain 2) transcripts in DES_SYNPO$^+$ cardiomyocytes
470 and of nuclear and perinuclear genes (domain 1 and 3) in CFLAR$^+$ CM clusters **(Fig. 2k)**.
471 In summary, we define distinct subcellular mRNA domains in human CMs and
472 demonstrate that their utilization differs systematically across our novel CM cell states,
473 with ICD-associated transcripts preferentially enriched in DES_SYNPO$^+$ CMs and nuclear
474 transcripts in CFLAR$^+$ CMs, consistent with divergent adaptive subcellular RNA
475 localization programs in human heart disease.

476 **Novel human cardiomyocyte cell states**

477 Next, we analyzed the molecular differences of the CM cell-states (**Fig. 3a-b**). We based
478 our annotation of the CMs clusters on unique marker gene expression (**Figure 3b**).
479 Desmin (*DES* gene), as intermediate filament in CMs, has important structural roles; it
480 connects several CMs organelles like the ICD complexes with mitochondria and the
481 nucleus[52,53]. HAND2$^+$ CMs represented the least represented CM cell state with 1.77%
482 (**Supplementary table 2**). The re-expression of *HAND2*, an fetal CM transcription
483 factor[54], combined with *MYH7B* points towards an fetal gene expression shift. *CFLAR*, or
484 *c-FLIP*, a direct Casp8 inhibitor and master anti-apoptotic regulator[55], is uniquely highly
485 expressed in human CMs when compared to mouse and rat snRNA-seq (**Fig. 3b, Fig.**
486 **1h**). It has been demonstrated that the gene *CFLAR* protects CMs from cell death in MI[56].
487 Based on the apparent specificity of CFLAR$^+$ marker genes to enlarged nuclei we
488 hypothesized that the novel HAND2$^+$ and CFLAR$^+$ CMs states could be related to
489 polyploid, or genome duplicated CM cell states. Nuclear DAPI stainings have been used
490 to identify polyploid nuclei in tissues previously[57]. To confirm our hypothesis we extracted
491 morphometric properties (using CellProfiler[58]) of CMs nuclei from our spatial
492 transcriptomics Xenium dataset and checked for association with our transcriptomically
493 defined CM cell state identities. This analysis showed a large degree of heterogeneity in
494 nuclear appearance for the different CM states (**Fig. 3c-d, Extended data Fig. 6a-d**), and

495 especially between CFLAR$^+$ and DES$^+$ CMs. Differences in DAPI texture and nuclei size
496 were also visibly distinct upon visual inspection (**Fig. 3d, Extended data Fig. 6a**). Among
497 the most distinct nuclear features in CFLAR$^+$ CMs were the area of the nuclei followed by
498 features related to DAPI intensity, edge intensity, entropy and granularity, consistent with
499 differences in polyploidy between the analyzed CM states and potentially linked to
500 chromatin changes **(Extended data Fig. 6b-c).** A machine learning model trained on
501 these nuclei images was able to differentiate CFLAR$^+$ and DES$^+$ CM based on both
502 CellProfiler morphometrics as well as vision model (Dinov3) features (**Extended data**
503 **Fig. 6d, Methods**).
504
505 To validate this result we next performed FANS (fluorescent activated nuclei sorting)
506 based on DAPI staining and resorted the nuclei to confirm the successful enrichment of
507 diploid (2N), tetraploid (4N) and octaploid (8N) nuclei (**Fig. 3e, Extended data Fig. 6e-i**).
508 We performed this experiment on tissue material of four patients, which we sorted for 2N,
509 4N and 8N DAPI content respectively, when enough material was available. This yielded
510 eight enriched snRNAseq datasets (see schematic in **Extended Data Fig. 6e**). A median
511 UMI count per nuclei of 3,233 and median of 1,640 genes per nuclei indicated that the
512 FACS procedure did not have a negative impact on data quality (**Supplementary Table**
513 **1**). Non-CM cells were mainly found in the diploid (2N) nuclei fraction, while 95% of nuclei
514 in the polyploid fraction consisted of CM (**Extended Data Fig. 6f**). Clustering of all CMs
515 across fractions revealed two distinct CM populations (**Extended Data Fig. 6g**). To
516 connect this data to our main non-FANS snRNA dataset we performed enrichment
517 analysis. The 8N fraction was strongly enriched for the CFLAR$^+$ CM signature, while the
518 2N fraction scored high for the DES$^+$ signature (**Fig. 3e, Extended Data Fig. 6i**). Nuclei
519 in the 4N fraction were split into high DES+ and high CFLAR scorers, which might indicate
520 a transitional cell state (**Fig. 3e, Extended Data Fig. 6h-i**). Taken together the DAPI and
521 FANS experiments confirmed that the CFLAR$^+$ CM gene signature is linked to ploidy state
522 of the CMs, while the DES$^+$ CM gene signature was more indicative of diploid CM.
523
524 While we could not identify the novel CM signatures in two previously published 3' based
525 snRNA datasets (**Extended data Fig. 1e+f**), we searched for scRNA-seq or snRNA-seq
526 studies of human heart tissue which identified similar heterogeneous CM states, which
527 were not related to atrial vs. ventricular phenotypes. The only exception being a dataset
528 from Wehrens et al.[59], where such CM clusters are described derived from human HCM
529 patients after septal myectomy and whole CM sequencing using SORT-seq (**Extended**
530 **data Fig. 6j**). When we mapped the CFLAR$^+$ CM and DES$^+$ CM gene scores in the
531 Wehrens scRNA-seq dataset, we could identify a clear enrichment and separation of the
532 two scores, fitting to our observation of novel CM states in ICM and DCM patient samples
533 (**Extended data Fig. 6k**). To increase our confidence in this mapping we employed a two-
534 pronged approach. Using ClusterFoldSimilarity[60] we calculated similarity scores between

535 the two datasets, based on differential genes expressed for each cluster. In addition we
536 performed a hyper geometric test (500 genes per cluster), which confirmed an overlap of
537 expression patterns between Wehrens cluster 5 and our polyploid HAND2$^+$ and CFLAR$^+$
538 CMs (**Extended data Fig. 6l**).
539
540 We next mapped structural, proliferative, metabolic and chromatin programs across CM
541 states (**Fig. 3f+g, Extended data Fig. 7a-j**). Contractile sarcomere genes diverged in a
542 CM state-resolved manner: thin-filament and titin/Z-disc gene sets separated clearly
543 across subtypes, indicating remodeling of the sarcomere. In particular *OBSCN*, *LDB3* and
544 *TTN* were upregulated in HAND2$^+$ and CFLAR$^+$ CMs (**Fig. 3f**). Metabolic pathway
545 analysis revealed a coordinated metabolic re-wiring (**Fig. 3g, Extended Data Fig. 7a-d**).
546 Diploid DES$^+$ CMs demonstrated upregulated β-oxidation genes, whereas polyploid
547 HAND2$^+$/CFLAR$^+$ states showed increase in glycolytic and glutaminolysis gene
548 expression (**Fig. 3g, Extended data Fig. 7a-c**). Over representation analysis comparing
549 DES$^+$ and CFLAR$^+$ CMs revealed significant enrichment of mitochondrial, oxidative
550 phosphorylation, and aerobic respiration–related gene sets in DES$^+$ CM (**Extended data**
551 **Fig. 7d**). We next compared the expression of cell-cycle regulatory genes (**Extended**
552 **data Fig. 7e-f**). In adult CMs three reactivation modes emerged. HAND2$^+$ CMs exhibited
553 G1/S-associated gene expression (*MYC*, *CDK4*, *CDK6*, *CCNE1*, *CCNE2*), with relative
554 enrichment for S-phase signatures compared to other states. Polyploid CFLAR$^+$ CMs re-
555 expressed late G2/M genes (*CDK1*, *CCNB1*, *AURKA*, *PRC1*, *HMMR*) in the absence of
556 G1/S induction, a pattern compatible with endoreplication-like genome duplication without
557 productive cytokinesis (**Extended data Fig. 7e-f**). DES_SYNPO$^+$ CMs also upregulated
558 cell-cycle associated genes, including *CCND1*/*CCND2* (G1), *MKI67* (pan-proliferation),
559 *TOP2A* (S/G2), and *CDK1* (mitotic entry)-consistent with partial engagement of cell-cycle
560 transcriptional programs (**Extended data Fig. 7e-f**).
561
562 Ion-channel programs segregated sharply by CM state (**Extended data Fig. 7g**).
563 Polyploid CFLAR$^+$ subsets showed the strongest pacemaker/diastolic-depolarization
564 signature (*HCN1*) together with an L-type Ca^{2+} module (*CACNA1C* with *CACNB2*) and
565 broad TRP upregulation (*TRPC1, TRPC3, TRPM4, TRPM7*) (**Extended data Fig. 7g**). In
566 contrast, diploid subtypes (NPPA_NPPB$^+$, SLC25A4$^+$, DES$^+$) preferentially expressed the
567 noncanonical connexin GJA3 (C*X*46), whereas polyploid CM states expressed GJC1
568 (CX45), indicating a potential junctional coupling shift at the ICD. Together, these patterns
569 point to a polyploid-biased increase in depolarizing drive (*HCN1*), Ca^{2+} influx capacity
570 (*CACNA1C*/*CACNB2*), mechanosensitive entry (*TRPM4*/*7*; *TRPC1/3*), and an ICD
571 connexin switch (*GJA3*→*GJC1*) (**Extended data Fig. 7g**). Chromatin and nuclear stability
572 gene programs were likewise CM state-specific (**Extended data Fig. 7h**). Polyploid
573 CFLAR$^+$ CMs, particular the HAND2$^+$ state, were enriched for histone
574 acetylation/methylation genes, chromatin-remodeling factors, and nuclear-stability

575 components, consistent with broad epigenomic reorganization accompanying metabolic
576 shift (**Extended data Fig. 7h)**. This was further supported by the unique upregulation of
577 nuclear receptor gene expression involved in metabolism in CMs, like *PPARα and PPARγ*
578 (**Extended data Fig. 7i).**
579
580 Gene set analysis revealed a clear enrichment of cardiac disease terms in polyploid
581 cardiomyocytes (CFLAR$^+$ and HAND2$^+$) including hypertrophic cardiomyopathy (HCM)
582 and dilatative cardiomyopathy terms (DCM) as well as the associated maladaptive cell
583 signalling pathways in cardiac remodelling including WNT signalling pathway (**Fig. 3h,**
584 **Extended data Fig. 7j**). NPPA-NPPB$^+$ CMs demonstrated enrichment in systolic heart
585 failure gene signature and cardiac hypertrophic response. DES$^+$ diploid cardiomyocytes
586 enriched in metabolic terms oxidative phosphorylation and fatty acid metabolism as well
587 as myogenesis and cardiac muscle contraction (**Figure 3h, Extended Data Fig. 7d and**
588 **7j**).

589 Next, we integrated the CM snRNA data with our previous CM snATAC data[11]. Based on
590 single-nucleus-resolved RNA expression and open chromatin information from our
591 previous work[11] we constructed an enhancer based gene regulatory network (eGRN) with
592 scMEGA[61].The estimated eGRN detected two main regulatory modules **(Supplementary**
593 **Table 4)**. One associated with low pseudo-time cells (DES$^+$ CMs) and one associated
594 with high pseudo-time cells (CFLAR$^+$, DES-SYMPO$^+$ and NPPA-NPPB$^+$ CMs). *CTCF*,
595 which is crucial in chromatin organization of the developing heart[62], was the most well
596 connected transcription factor (TF) (highest pagerank) in the GRN module related to
597 DES$^+$ CMs (**Supplementary Table 4**). The integrated dataset was then used to construct
598 a cell differentiation tree with PHLOWER[63]. By using DES+ CM cells as root, PHLOWER
599 indicated branches leading to DES-SYNPO$^+$ CMs and another branching leading to
600 CFLAR$^+$ or NPPA-NPPB$^+$ CMs (**Fig. 3i**). We observe lower TF activity of *CTCF* in disease
601 related CM sub-states such as CFLAR$^+$, NPPA_NPPB+ and DES_SYNPO$^+$ CMs
602 (**Extended Data Fig. 7k**). Along this trajectory, CFLAR$^+$ CMs displayed dynamic
603 regulation of WNT pathway modulators, including a decrease expression of the WNT
604 antagonist *DKK3* (**Fig. 3j**) and *SFRP1* (**Fig. 3k**), alongside induction of canonical WNT
605 target genes such as *AXIN2* and the kinase *TNIK* (**Fig. 3k**). The main transcription factor
606 regulated to DES-SYNPO$^+$ branch was *WT1* (**Supplementary Table 4**), which is a known
607 epicardial regulator[64] and is known to directly regulate synaptopodin gene expression e.g.
608 in podocytes in the kidney[65]. Its knock-out is known in zebrafish to lead to a loss of CM
609 expression programs and upregulation of epicardial gene expression[66]. For CFLAR$^+$
610 CMs, predicted regulators include the sonic hedgehog pathway TF *GLI3*, which has a
611 known muscle repair–associated angiogenesis role in myocytes[67] and *NR2C2* (or *TR4*),
612 a reporter repressor of PPARα nuclear receptor signaling[68] (**Supplementary Table 4**).

613 We next analyzed the expression of ligands and receptors of known canonical fetal cell-
614 cell communication pathways and fibrosis related pathways in cardiomyocytes
615 (**Extended Fig. Data 8a-c**). CFLAR$^+$ and HAND2$^+$ CMs showed the highest expression
616 among CMs of receptor and ligands associated with maladaptive remodelling including
617 the receptor *NOTCH2* and ligands *JAG2*, *DLL1* together with non-canonical WNT ligands
618 (*WNT5A*, *WNT11*). Among these, HAND2$^+$ uniquely presented upregulated *SHH*
619 expression, whereas CFLAR$^+$ CM states demonstrated high *PTCH1/SMO* levels. In
620 contrast, DES$^+$, NPPA_NPPB$^+$, and SLC25A4$^+$ CMs preferentially expressed WNT
621 antagonists (*DKK3*, *SFRP1*/*2*) and showed generally attenuated Notch/HH signatures,
622 consistent with a contractile/stress-adapted phenotype that restrains canonical Wnt
623 activity (**Extended Fig. data 8a**). We next analyzed fibrogenic cell-cell-communication
624 pathways (TGFβ, PDGF, endothelin, *VEGF*/*ANGPT*, FGF/NRG axes) across CM states
625 (**Extended Fig. data 8b**). DES$^+$, NPPA_NPPB$^+$, SLC25A4$^+$, and especially
626 DES_SYNPO$^+$ were enriched for distinct profibrotic and proinflammatory ligands,
627 including *TGFB* isoforms, *PDGFR-A/B*, *VEGFB* and *VEGFC*, *IL6* and *CXCL12* consistent
628 with a CM-derived "injury signal" that can activate fibroblasts and vascular/perivascular
629 cells (**Extended Fig. data 8b-c**). In contrast, CFLAR$^+$ and HAND2$^+$ CMs preferentially
630 expressed growth-factor receptors (*TGFBR1/2*) together with *ERBB2/ERBB4* and the
631 profibrotic ligands EDN1 and FGF2, indicating a divergent send-receiver profibrotic
632 phenotype between CM states (**Extended Fig. Data 8b-c**).
633
634 In order to consider both cell-cell colocalization and changes in ligand-receptor
635 expression across disease conditions, we performed a cell-cell communication analysis
636 with scSeqComm[69] and CrossTalkeR[70] by focusing on colocalized cell pairs predicted by
637 NicheSphere (**Fig. 2a; Methods**). We first used CrossTalkeR pagerank to identify highly
638 influential cell types in ICM disease. This indicates the importance (higher communication
639 in ICM) of diploid CM clusters (SLC25A4$^+$, DES_SYNPO$^+$, DES+$^+$) with a highest score
640 for the SLC25A4$^+$ CMs and immune cells like neutrophils, macrophages (**Extended Data
641 Fig. 8d**). We next analyzed differences in intracellular signalling in CM from disease
642 samples. scSeqComm calculates differential cellular communication scores, which reflect
643 how cell-cell communication affects down-stream pathways and transcriptional
644 regulation.
645 This indicates an upregulated activity of WNT, NOTCH and Hedgehog signalling in
646 CFLAR$^+$ CMs in the ICM vs. control contrast (**Fig. 3l**). If we consider the signals related
647 to WNT activation towards CFLAR (**Fig. 3m-n**), we observe increased signalling from
648 myofibroblasts including *CTHRC1*[71]*, CCN2 and WNT11* (**Fig. 3m**). These predictions are
649 consistent with our prior spatial analysis showing interaction of CFLAR$^+$ CM with
650 myofibroblast in all disease conditions and indicates the activation of WNT signalling in
651 CFLAR$^+$ CM cells. In ICM myofibroblasts secreted *CTHRC1*[71] can bind *FZD6* on CFLAR$^+$
652 CMs to potentiate non-canonical Wnt signaling. Reciprocally, CFLAR$^+$ CM show an

653 increased secretion of VEGFA towards myofibroblasts (**Fig. 3n**). Other signals that drive
654 the fibrotic niche created by CFLAR+ CMs are *AREG*, *DLL1* and *FAT4* (**Extended data**
655 **Fig. 8e-f**). For the DCM vs control contrast, our colocalization analysis (**Fig. 2g**) indicated
656 an unique role of DES-SYNPO$^+$ CMs. Moreover, DES-SYNPO$^+$ CMs had the strongest
657 proinflammatory gene signatures including IL6, CCL2 and CXCL8 (**Extended data Fig.**
658 **8c**). We identified a reciprocal signalling axis of neutrophils and NK cells to DES-SYNPO$^+$
659 CMs involving *GNAI2* and *CCL5* highlighting a distinct immune-CM axis in DCM
660 (**Extended data Fig. 8h-i**). Overall CFLAR$^+$ CM presented stronger WNT signalling in the
661 disease contrast particularly for DCM vs. control (**Fig. 3o**). Collectively, our results reveal
662 distinct CM states characterized by polyploidy linked remodeling of contractile,
663 electrophysiological, metabolic, and chromatin programs. These CM state-specific
664 programs converge further on specific trajectories, positioning cardiomyocyte genome
665 multiplications as a central organizing principle of CM-linked remodeling in human heart
666 disease.

667 **Fetal vs. adult human cardiomyocytes**

668 A central observation in cardiac transcriptomic analysis is that postnatal hearts adopt a
669 fetal-like transcriptional state, also referred to as the "fetal gene hypothesis" in response
670 to stress or chronic injury[72]. Given the expression of cardiac fetal genes like *MYH7B* and
671 *TNNT1* in polyploid CMs, we next addressed how conserved this gene expression
672 signature is. To this end, we generated snRNA data using fresh frozen human fetal heart
673 tissues from five timepoints conserved in RNAlater solution (p.c.w. 12 - 22) (**Figure 4a**).
674 In total we recovered 146,025 nuclei (**Extended Data Fig. 9a**). In the median they
675 contained 3,531 UMIs and expressed over 1,886 median genes. Our analysis focused on
676 CMs of the left ventricle and identified six major cell states, which recapitulated divergent
677 CFLAR$^+$-DES$^+$ CM expression observed in adult human cardiomyocytes (**Figure 4b-c**, all
678 cells shown in **Extended Data Fig. 9a-b** and **Supplementary table 2**).
679
680 Compared to other fetal heart datasets[73,74], our data for the first time revealed all stages
681 of fetal CM proliferation (**Fig. 4d**). The subclusters cycling and proliferating CMs mapped
682 to the cell-cycle S-phase and G2/M-phase respectively (**Fig. 4d**, **Extended Data Fig. 9b**).
683 We next compared our novel human adult CM states with the cell-cycle scores (S and
684 G2/M) of our human fetal snRNA data (**Extended Data Fig. 9c-d**). While we found the
685 vast majority of adult human CMs in G1-phase and 1% in G2M, none of them were
686 enriched in cell cycle genes to the same level as the proliferating cells in the fetal heart
687 (**Extended data Fig. 9d**).
688
689 In addition to these cell-cycle cardiomyocytes, which we grouped for downstream
690 analysis, we were able to identify CM in multiple stages of maturation based on the
691 canonical maturation markers *HOPX*[75] and *TCAP*[76] (**Fig. 4b**, **Extended Data Fig. 9e**).

692 Gene-set enrichment analysis revealed an increase of cell-proliferation terms in cycling
693 CMs, WNT pathway terms and glycolysis for immature CMs and myofibril-assembly and
694 cardiac contraction for mature CMs (**Extended Data Fig. 9f**), which corroborated our
695 annotation. Interestingly, we could detect a similar shift in sarcomere gene expression of
696 fetal immature vs. mature cardiomyocytes (**Fig. 4e**) and changes in β-oxidation and
697 glycolysis regulating genes compared to adult human CFLAR$^+$DES$^+$ and DES$^+$CFLAR$^+$
698 CM (**Fig. 4f**). In order to study the spatial arrangement of these fetal CM states we
699 mapped their location in the tissue using a publicly available spatial transcriptomics
700 dataset[74]. We saw the expected enrichment of our atrial and trabecular cells in their
701 respective compartments (**Extended Data Fig. 9g-h**). Immature and mature CM were
702 more evenly spread throughout the heart, although there was a higher level of immature
703 cells around the right ventricle and a higher level of mature cells in AV-plane papillary
704 muscle, which might relate to different mechanical strain in these distinct tissue regions
705 (**Fig. 4g, Extended Data Fig. 9g**).
706
707 Next we investigated gene expression changes during CM maturation. We subsetted our
708 data to immature, differentiating and mature CMs and calculated a diffusion map, to
709 visualize the continuous trajectory of the maturation process (**Fig. 4h**). By assigning cells
710 a pseudo-temporal ordering we were then able to study expression trends along this
711 trajectory. We found that an increase of the DES$^+$ and a decrease of CFLAR$^+$ signatures,
712 derived from the adult snRNA dataset, were among the most significant results (**Fig. 4i**).
713 Maturation was also accompanied by increased cellular respiration and oxidative
714 phosphorylation (**Fig. 4i**).
715
716 In the next step we used ClusterFoldSimilarity[60] and a hypergeometric test to compare
717 the embryo subclusters to the adult human CMs. We found that adult HAND2$^+$ and
718 CFLAR$^+$ were significantly enriched in proliferating fetal CMs (**Fig. 4j**). Mapping of fetal
719 cell types into the PHLOWER cell differentiation tree based on adult CMs confirmed that
720 immature LV-CMs are related to the CFLAR+ CM branch **(Extended Data Fig. 9i**).
721
722 Overall, our data uncover a conserved fetal differentiation trajectory of CMs that provides
723 a reference framework for adult CM states in human heart disease. Polyploid HAND2$^+$
724 and CFLAR$^+$ CMs transcriptionally revert toward immature fetal programs, whereas
725 diploid DES$^+$ and DES–SYNPO$^+$ CMs represent terminally differentiated, contractile end
726 states. Notably, polyploid CMs do not reacquire fetal proliferative signatures, supporting
727 a model of incomplete fetal reprogramming rather than regenerative proliferation.

728 **Temporal disease association and HF targets in CMs**

729 To study the novel CM heterogeneity and their dynamics with spatiotemporal resolution,
730 we performed snRNA-seq and Xenium in mice after LAD ligation across four post-MI time

731 points from day 3 to day 28 (**Fig. 5a**). In total, we recovered 75,825 nuclei from snRNA-
732 seq and 543,586 nuclei from spatial transcriptomics (**Fig. 1g; Supplementary Table 2**),
733 which allowed the detection of six transcriptionally distinct cardiomyocyte states (**Fig. 5b**).
734 Marker-gene expression of the novel human CM clusters demonstrated conservation in
735 the mouse dataset (**Fig. 5c, Extended Data Fig. 10a**), with a major cluster high in *Des*
736 and a second one expressing fetal genes like *Myh7b*, although *Cflar* was expressed at
737 much lower levels than in the human.

738 We next quantified shifts in CM state abundances across the post-MI time course[77]. Both
739 Des$^+$ and Myh7b$^+$ CMs were reduced at day 3 following the acute MI, whereas
740 NPPA_NPPB$^+$ CMs represented the only CM population that increased at this early injury
741 time point (**Fig. 5d, Extended data Fig. 10b**). By day 7, the trajectories of Des$^+$ and
742 Myh7b$^+$ CMs diverged: Des$^+$ CMs remained low, while Myh7b$^+$ CMs expanded
743 progressively and became the dominant CM population at later stages (**Fig. 5d**). This
744 delayed but pronounced enrichment of Myh7b$^+$ CMs after injury highlights them as an
745 adaptive CM state that emerges during post-ischemic remodelling.

746 To link mouse and human CM states, we applied ClusterFoldSimilarity[60] and enrichment
747 test, which showed that the Des$^+$ CM nuclei from mouse overlapped in their expression
748 with diploid cardiomyocytes of the adult human heart (DES$^+$, SLC25A4$^+$, DES_SYNPO$^+$,
749 NPPA_NPPB$^+$), whereas the Myh7b$^+$ CM mouse nuclei were more similiar to the in the
750 human polyploid HAND2$^+$ and CFLAR$^+$ CM nuclei (**Fig. 5e**). Nppa$^+$ mouse CMs
751 overlapped significantly with NPPA$^+$ human CMs but also shared markers with human
752 HAND2$^+$ and CFLAR$^+$ CMs (**Fig. 5e**). We then compared the mouse clusters to our fetal
753 human data. Des+ CM were most similar to terminally differentiated CM, while Myh7b$^+$
754 CM showed correspondence to fetal immature MYH7B+ cells, a similar trend to what we
755 observed in our adult to fetal comparison (**Extended Data Fig. 10c**).

756 Next we compared transcriptional programs between mouse CM subtypes (**Fig. 5f-g and**
757 **Extended Data Fig. 10d–i**). Sarcomere-associated genes, including *Obscn*, *Ldb3*, *Ttn*
758 and *Mybpc3*, were significantly upregulated in Myh7b$^+$ CMs, whereas genes involved in
759 β-oxidation regulation where upregulated in Des$^+$ CMs mirroring the human polyploid
760 pattern (**Fig. 3f-g, 5f-g**). Analyses of glycolytic and glutaminolysis genes (**Extended Data**
761 **Fig. 10d-e**) showed that Myh7b$^+$ CMs demonstrated reduced gene expression consistent
762 with a metabolically rewired, stress-adapted state, whereas Des$^+$ CMs maintained a more
763 oxidative, metabolic increased profile (**Extended Data 10d-f**). Because our human data
764 implicated polyploid CMs in fibrotic and developmental signalling, we next systematically
765 assessed these pathways in the mouse model (**Extended data Fig. 10g-i**). Our analysis
766 shows that canonical profibrotic ligands and receptors including Tgfb isoforms, *Tgfbr1/2,*
767 *Pdgfa/b, Pdgfra/b, Edn1/Ednra/Ednrb*, *Vegfa* and *Il6/11*,were strongly enriched in Nppa$^+$
768 and Myh7b$^+$ CMs compared to Des$^+$ CMs, while Des+ CMs preferentially expressed

769 *Vegfb* and *Vegfc* (**Extended Data Fig. 10g-i**). This pattern is only partially concordant
770 with the human heart, where polyploid CFLAR+/HAND2+ CMs demonstrated higher
771 upregulated gene expression of fibrosis signalling ligands and receptors (**Extended Data**
772 **Fig. 8b, 10g-i**). However a marked bias of WNT (particularly WNT5/11) and Hedgehog
773 signaling components towards Myh7b$^+$ CMs remained: Myh7b$^+$ cells expressed multiple
774 WNT ligands and receptors, NOTCH ligands and receptors, and Sonic hedgehog
775 pathway members, whereas Des$^+$ CMs predominantly expressed inhibitory modulators
776 such as *Sfrp1* and *Dkk3* (**Extended data Fig. 8g+i).**

777 Intracellular pathway analysis of mouse CM states revealed notable differences
778 compared to human CMs (**Extended Data Fig. 10j**). Specifically, WNT, TGFβ, and Notch
779 signaling were predominantly upregulated in murine Nppa+ CMs rather than Myh7b+
780 CMs, highlighting a species- or model-dependent divergence in signaling. Despite this,
781 the general functional stratification was conserved: the adaptive Nppa+ state in mice
782 concentrated profibrotic and developmental signaling capacities, whereas Des+ CMs
783 retained a restrained, homeostatic profile similar to that of humans (**Extended Data Fig.**
784 **10j**).

785 Next, we performed spatial colocalization analysis, using NicheSphere of Xenium mouse
786 data, contrasting controls and ICM conditions (days 7,14 and 28), which detected six
787 major tissue niches (**Fig. 5h**). In the mouse heart, Des$^+$ and Myh7b$^+$ CMs largely shared
788 a common myocardial niche (niche 6 - myocardium) indicating that diploid and polyploid
789 CMs coexist within the same anatomical compartments (**Fig. 5h-i**). Cells in this niche
790 tended to lose their colocalization to other cell-types upon diseases. By contrast, NPPA$^+$
791 CMs dominated a distinct niche that showed a gain of colocalization with myofibroblasts
792 in ICM, consistent with their transcriptional injury response program (**Fig. 5i**). This
793 organisation differs from the human heart, where Des$^+$ and polyploid CFLAR$^+$/HAND2$^+$
794 CMs segregate into two spatially distinct niches suggesting that niche partitioning of
795 diploid versus polyploid CMs is, at least in part, time- and species-dependent. NPPA$^+$
796 mouse CMs in niche 2 mapped predominantly to the "damaged myocardium 3" region in
797 the heart patch atlas, in which also the human NPPA_NPPB CMs enriched (**Fig. 5j**). This
798 underscores conserved features of the injury-associated NPPA+ states across
799 myocardial tissue from different mammalian species. Next we performed a PILOT
800 trajectory analysis on spatial niches, which indicates the decrease of myocardium (niche
801 1) and increase of Nppa+ (niche 2) and the myofibroblast_enriched niche (niche 3) among
802 others and revealing an overall increase in periostin expression fitting to our previous data
803 (**Fig. 5i, Extended Data Fig. 11a-b**).

804 Finally, we analyzed the expression of heart failure drug targets in our mouse snRNA
805 data (**Extended Data Fig. 11c**). This revealed a conserved, dichotomous expression
806 pattern: three out of four major heart-failure targets, β1-adrenergic receptor (*Adrb1*),

807 mineralocorticoid receptor (*Nr3c2*) and angiotensin II receptor (*Agtr1*) were predominantly
808 expressed in Myh7b$^+$ CMs, while *Pde5a* and *Gucy1a1* were enriched in pericytes and
809 vascular smooth muscle cells (**Extended Data Fig. 11c**). *Glp1r* expression was mainly
810 restricted to T cells. Adrenoceptor (β1) expression overall was higher in Myh7b$^+$ than in
811 Des$^+$ CMs. Comparing the dynamics of mineralocorticoid receptor (*Nr3c2*) expression,
812 we noted a marked expression dynamics only in Myh7b+ CMs (**Fig. 5k).** We next asked
813 if this pattern of HF drug target expression is recapitulated in our human snRNA data and
814 curated a panel of established drug targets and well-supported HF mediators and profiled
815 their expression across all cardiac cell subtypes (**Fig. 5l**). Of the four standard of care
816 drugs - β1-blockers, ACEi/ARB, mineralocorticoid-receptor (MR) antagonists, and SGLT2
817 inhibitors, we observed a selective enrichment of transcripts encoding two these targets
818 in polyploid CMs (HAND2+/CFLAR+) (**Fig. 5l).** Additionally, we found a significant
819 enrichment of *GLP1R* in polyploid CMs, which in mice was restricted to Treg and CD8-T-
820 cells (**Fig. 5l, Extended Data 11d**). *AGTR1* was primarily expressed in cardiac pericytes
821 and fibroblasts (**Fig. 5l**) as well as transcripts for *PDE5A* and the soluble guanylyl cyclase
822 α1 subunit (*GUCY1A1*). Together, our HF target gene analysis indicates that polyploid
823 CMs constitute a major previously unrecognized target cell for heart failure therapies.
824 Additionally, the pharmacologic control points for the cGMP pathway are predominantly
825 enriched in the vascular/perivascular compartment, not the endothelium. In sum, our
826 analysis suggests a compartment-specific division of therapeutic action in human heart
827 failure treatment, with polyploid CMs as a major myocardial drug-addressable population.

828 **TNIK inhibition ameliorates maladaptive remodelling by targeting polyploid CMs**

829 Based on prior evidence implicating TNIK in WNT-dependent fibrotic programmes[78], we
830 examined TNIK expression across our multispecies snRNA-seq atlas and observed
831 consistent enrichment in CFLAR+ or Myh7b+ CMs across human, mouse, and rat
832 (**Extended data Fig. 12a-d**). While TNIK expression was not strictly CM-restricted, being
833 detectable in human mast cells and select murine T-cell populations, the rat heart
834 displayed the highest CM specificity (**Extended data Fig. 12d**). This enrichment
835 suggested a potential role for TNIK in regulating polyploid CM states.

836 To investigate the functional consequences of TNIK inhibition in CMs, we assessed its
837 effects both *in vitro* using human iPSC-derived CMs (**Fig. 6a-g)** and *in vivo* in a rat MI
838 model (**Fig. 6h-p, Extended Data Fig. 12e-j**). Long-term differentiated beating CMs from
839 two independent iPSC lines were treated for seven days with the TNIK inhibitor NCB-
840 0846[79] or vehicle and profiled by snRNA-seq. Unsupervised clustering identified two
841 major CM populations (**Fig. 6b**), which we annotated as mature and immature based on
842 enrichment analysis (**Fig. 6c**). The more immature CM showed the fetal-like CLFAR
843 signature, while the mature cluster closely resembled DES$^+$ CM. ClusterFoldSimilarity[60]
844 and a hypergeometric test verified the similarity to DES$^+$ and CFLAR+ clusters from the

adult dataset (**Fig. 6d)**. Cell-type abundance analysis revealed a significant increase in mature CM states following TNIK inhibition (**Fig. 6e**). Gene set enrichment analysis demonstrated a marked reduction in hypoxia-associated transcriptional programmes, metabolic changes and changes in RNA transport and splicing after TNIK inhibition (**Fig. 6f**). Although global WNT pathway activity was not significantly altered (**Extended Data Fig 12g**), TNIK inhibition resulted in coordinated expression changes of non-canonical WNT components, including decreased *WNT11* and *NFATC4* expression and induction of the WNT antagonists *SFRP1* and *SFRP5* (**Fig. 6g**). Together, these findings indicate that TNIK inhibition promotes maturation-associated CM states alongside reduced hypoxia signalling and selective remodelling of WNT-related transcriptional programmes.

Discussion

In this study, we provide a multi-scale, multimodal view of how CM heterogeneity, ploidy state and microenvironmental context shape cardiac remodeling in human heart disease. We integrate single-nucleus transcriptomics, chromatin profiling, high-resolution spatial transcriptomics and histology across ischemic and non-ischemic cardiomyopathies, human development, and in three mammalian species. Our analysis revealed that disease progression is not only encoded in changes of cell-type composition and fibrosis, but in the emergence of distinct diploid and polyploid cardiomyocyte states that shape spatial niches and drive cardiac remodeling.

We systematically dissect diploid versus polyploid cardiomyocytes in the human heart. Using DAPI-based nuclear profiling, FANS-enriched ploidy fractions and integrative snRNA-seq, we show that polyploid cardiomyocytes form distinct transcriptional states, marked by CFLAR and HAND2, which are enriched in 4N/8N nuclei, engage specific metabolic and chromatin-remodeling programs, and display a disease-biased remodeling signature. In contrast, predominantly diploid DES^{+} CMs preserve oxidative phosphorylation–dominated metabolic profiles and mature sarcomere programs. Direct comparison to human fetal hearts indicates that HAND2^{+} and CFLAR^{+} polyploid CMs align with proliferating and immature fetal states, whereas DES^{+} and DES_SYNPO^{+} CMs resemble terminally differentiated, contractile end states. Together, these findings refine the fetal gene hypothesis by demonstrating that developmental reactivation in human heart disease is partial, selective, and strongly shaped by CM ploidy, rather than representing a generic fetal-like state.

At the tissue level, CM states organize into distinct spatial niches that differ between ischemic and non-ischemic cardiomyopathies. Polyploid CFLAR^{+}/HAND2^{+} CMs preferentially localize to myocardium and damaged myocardium, whereas DES^{+} and DES_SYNPO^{+} states colocalize with myofibroblasts and tissue-resident macrophages in fibrotic and chronically remodeled regions. The use of deep learning models for histology

882 analysis revealed distinct damaged cardiomyocyte regions conserved in both mouse and
883 human, which could not be identified by expert pathologists. These distinct areas have
884 differences in both their level of damaged NPPA_NPPB CMs and lymphocyte cells.
885 Subcellular spatial transcriptomics further reveals a discrete ICD transcriptome
886 compartment, enriched for junctional regulators, cytoskeletal linkers and local mRNA-
887 regulatory components. Differential analysis of this ICD program across cardiomyocyte
888 states and ploidy suggests that altered mRNA localization and junctional remodeling may
889 contribute to conduction and mechanical dysfunction in heart disease. As resources, we
890 provide machine learning models that allow researchers to segment CM in their own
891 microscopy or spatial transcriptomic data, as well as classifiers that detect regions of
892 interest in H&E stains and polyploidy in DAPI images.

893 Ligand–receptor and drug-target mapping position these CMs states within a structured
894 signaling and therapeutic landscape. Polyploid CFLAR^{+} and HAND2^{+} cardiomyocytes act
895 as major receivers and sender of distinct developmental and fibrotic cues, with enriched
896 Notch, non-canonical Wnt and Hedgehog receptors, as well as TGFβ and ERBB signaling
897 components. More differentiated DES^{+}, NPPA_NPPB^{+} and SLC25A4^{+} CMs preferentially
898 express Wnt antagonists. Analysis of heart failure drug targets demonstrated that
899 molecular targets of standard-of-care therapies, such as β-blockers and mineralocorticoid
900 receptor antagonists, show marked enrichment in polyploid CMs. These data suggest a
901 compartmentalized division of therapeutic action and highlight polyploid CMs as a major
902 drug-addressable myocardial population in patients.

903 This study is limited by the observational nature of human end-stage cardiac tissues,
904 targeted spatial gene panels, and reliance on transcript-based inference for signaling and
905 drug-target activity. In addition, ploidy assignment is based on DAPI content and
906 enrichment rather than direct lineage tracing. Furthermore, our pharmacological
907 perturbation of TNIK in in vivo model is not CM-subtype specific. Future work combining
908 CM-subtype-specific genetic perturbations, higher-plex spatial profiling, and functional
909 assays of electrophysiology and force generation will be required to test causal roles of
910 individual CM states and to define how genome multiplication mechanistically
911 constrains—or enables—cardiomyocyte plasticity.

912 Finally, through cross-species analyses we nominated TNIK as a nodal kinase in
913 polyploid cardiomyocyte remodeling. TNIK inhibition in a rodent model of myocardial
914 infarction ameliorated remodelling, reduced fibrosis and improved myocardial function.
915 We anticipate that these insights will serve as a reference to dissect when and how diploid
916 cardiomyocytes transition into maladaptive polyploid states, and to guide the design of
917 interventions enabling the development of novel cardiac therapeutic strategies, such as
918 TNIK inhibition, that selectively reprogram pathological CM states to restore essential
919 myocardial function.

Methods

Detailed methods description is provided in a separate file.

Data availability

All data will be shared at the time of publication. Sequencing data will be deposited to the European Genome-phenome Archive (EGA) and ArrayExpress. Processed anndata files will be shared on Cell x Gene. Spatial transcriptomic datasets will be shared through the BioImage Archive. The data will additionally be presented in an interactive viewer at heartatlas.kuppelab.org.

Code availability

Analysis code will be made available from https://github.com/kuppe-lab/polyploid-heart.

Acknowledgements

This project has been funded by the German Research Foundation received by C.K. (CRU344-417911533, CRU5011-445703531, Emmy Noether EN-459969915); received

947 by I.C. (DFG; 3888802535, CRU5011-445703531) by the the German Ministry of
948 Science, Technology and Space (BMFTR) consortia Graphs4Patients for C.K., M. S. and
949 I.C and E:MED Fibromap and CureFib for I.C. and R.K. This work was further supported
950 by grants to CK from the European Research Council (ERC-StG-101040726), the
951 Boehringer Ingelheim Foundation, Else Kroener Fresenius Foundation (EKFS, Physician
952 Scientist Professorship CK) and the Aventis Foundation. R.K. received support from the
953 German Research Foundation (DFG: SFBTRR219 322900939, CRU344
954 4288578857858, CRU5011 445703531, KR4073/18-1 (561848128) & INST 222/1582-1),
955 the European Research Council (ERC-CoG 101043403 & 101001791, ERC-PoC
956 101212974 and 10104303), the Leducq Foundation (ImmunoFibHF 20CVD02 and
957 COMET 24CVD02). G.C. was partially supported by Fondazione Ing. Aldo Gini. Views
958 and opinions expressed are those of the authors only and do not necessarily reflect those
959 of the European Union or the European Research Council Executive Agency. Neither the
960 European Union nor the granting authority can be held responsible for them. We thank
961 Dr. Igor Efimov from the Northwestern University, Chicago, IL, USA, for providing fixed
962 human donor heart samples. NM is supported by the Deutsche Forschungsgemeinschaft
963 (German Research Foundation; TRR 219; Project-ID 322900939. We thank the IZKF
964 Aachen Genomics Core facility for sequencing experiments. The Dutch Fetal Biobank
965 received funding from Amsterdam UMC (Innovation Impuls) and the Amsterdam
966 Reproduction and Development research institute.
967
968 We thank all supporting centers, physicians, midwives and nurses for the information they
969 have provided to parents who considered donating their fetuses to science and in
970 particular to the DFB. Most importantly, we express our gratitude to all mothers and
971 couples who have donated their most precious gift to the scientific community.
972
973 This study is part of the UCC-UNRAVEL biobank (www.unravelrdp.nl). The study was
974 approved by the local institutional ethics review board (University Medical Center Utrecht,
975 protocol UCC-UNRAVEL #12-387 and TCBio 25-242) ERN UNRAVEL is Member of the
976 European Reference Network for rare, low prevalence and complex diseases of the heart:
977 ERN GUARD-Heart (ERN GUARD HEART; http://guardheart.ern-net.eu)
978
979 The data used in this publication was managed using the research data management
980 platform Coscine with storage space granted by the Research Data Storage (RDS) of the
981 DFG and Ministry of Culture and Science of the State of North Rhine-Westphalia (DFG:
982 INST222/1261-1 and MKW: 214-4.06.05.08 - 139057).
983
984 The authors gratefully acknowledge the computing time provided to them at the NHR
985 Center NHR4CES at RWTH Aachen University (project number p0020567). This is
986 funded by the Federal Ministry of Education and Research, and the state governments

987 participating on the basis of the resolutions of the GWK for national high performance
988 computing at universities (www.nhr-verein.de/unsere-partner).
989
990 The authors wish to thank the many other people who assisted in the completion of the
991 manuscript. Among them Louis Kümmerle for helping with spatial transcriptomic panel
992 design, Clarence K. Mah for his advice on BENTO and Beth Cimini for input on cell
993 segmentation and image alignment. In addition we thank Vizgen, Inc. for giving us early
994 access to MERFISH v2 chemistry and technical support by Marc Reudelsterz and 10x
995 Genomics, Inc. for giving us access to FLEX rat probes.

996 **Competing Interest**

997 CK received honoria from within the last 2 years from BAYER and received research
998 funding from Insilico for this study to perform rat snRNA-sequencing experiments. RK
999 acknowledges the following outside of the submitted work, he is founder and board
1000 member of Sequantrix GmbH, received honoraria from Bayer, Chugai, Pfizer, Roche,
1001 Genentech, Eli Lilly, and GSK, AMGEN, Sobi, Hybridize Therapeutic, Valerio
1002 Therapeutics, Exigent Therapeutics for advisory board meetings and received research
1003 funding from Travere Therapeutics, Galapagos, Chugai, Novo Nordisk, and Ask Bio.
1004
1005 F.R., H.Z., M.Z., and A.Z. are employees of Insilico Medicine, which develops generative
1006 artificial intelligence and related technologies for drug discovery, drug development, and
1007 aging research. Insilico Medicine has ongoing therapeutic programs, including rentosertib
1008 (INS018_055) in fibrotic and other disease areas.
1009
1010 The remaining authors declare no competing interests.
1011
1012 **References**

1013 1. Koopmans, T. & van Rooij, E. Molecular gatekeepers of endogenous adult
1014 mammalian cardiomyocyte proliferation. *Nat. Rev. Cardiol.* (2025)
1015 doi:10.1038/s41569-025-01145-y.
1016 2. González-Rosa, J. M. *et al.* Myocardial polyploidization creates a barrier to heart
1017 regeneration in zebrafish. *Dev. Cell* **44**, 433–446.e7 (2018).
1018 3. Global Burden of Cardiovascular Diseases and Risks 2023 Collaborators. Global,
1019 regional, and national burden of cardiovascular diseases and risk factors in 204
1020 countries and territories, 1990-2023. *J. Am. Coll. Cardiol.* (2025)
1021 doi:10.1016/j.jacc.2025.08.015.
1022 4. Bozkurt, B. Contemporary pharmacological treatment and management of heart
1023 failure. *Nat. Rev. Cardiol.* **21**, 545–555 (2024).
1024 5. Derks, W. *et al.* A latent cardiomyocyte regeneration potential in human heart
1025 disease. *Circulation* **151**, 245–256 (2025).
1026 6. Poss, K. D., Wilson, L. G. & Keating, M. T. Heart regeneration in zebrafish. *Science*

1027 **298**, 2188–2190 (2002).
1028 7. Wang, Z. *et al.* Mechanistic basis of neonatal heart regeneration revealed by
1029 transcriptome and histone modification profiling. *Proc. Natl. Acad. Sci. U. S. A.* **116**,
1030 18455–18465 (2019).
1031 8. Swift, S. K. *et al.* Cardiomyocyte ploidy is dynamic during postnatal development
1032 and varies across genetic backgrounds. *Development* **150**, (2023).
1033 9. Paredes, A. *et al.* γ-Linolenic acid in maternal milk drives cardiac metabolic
1034 maturation. *Nature* **618**, 365–373 (2023).
1035 10. Kanemaru, K. *et al.* Spatially resolved multiomics of human cardiac niches. *Nature*
1036 **619**, 801–810 (2023).
1037 11. Kuppe, C. *et al.* Spatial multi-omic map of human myocardial infarction. *Nature* **608**,
1038 766–777 (2022).
1039 12. Man, J. C. K. *et al.* Genetic dissection of a super enhancer controlling the Nppa-
1040 Nppb cluster in the heart. *Circ. Res.* **128**, 115–129 (2021).
1041 13. Sergeeva, I. A. *et al.* Identification of a regulatory domain controlling the Nppa-
1042 Nppb gene cluster during heart development and stress. *Development* **143**, 2135–
1043 2146 (2016).
1044 14. Li, X. *et al.* Inhibition of fatty acid oxidation enables heart regeneration in adult
1045 mice. *Nature* **622**, 619–626 (2023).
1046 15. Derks, W. & Bergmann, O. Polyploidy in cardiomyocytes. *Circ. Res.* **126**, 552–565
1047 (2020).
1048 16. Schoenfelder, K. P. & Fox, D. T. The expanding implications of polyploidy. *J. Cell*
1049 *Biol.* **209**, 485–491 (2015).
1050 17. Gjelsvik, K. J., Besen-McNally, R. & Losick, V. P. Solving the polyploid mystery in
1051 health and disease. *Trends Genet.* **35**, 6–14 (2019).
1052 18. Pandit, S. K., Westendorp, B. & de Bruin, A. Physiological significance of
1053 polyploidization in mammalian cells. *Trends Cell Biol.* **23**, 556–566 (2013).
1054 19. Gan, P., Patterson, M. & Sucov, H. M. Cardiomyocyte polyploidy and implications
1055 for heart regeneration. *Annu. Rev. Physiol.* **82**, 45–61 (2020).
1056 20. Peterson, N. G. & Fox, D. T. Communal living: the role of polyploidy and syncytia in
1057 tissue biology. *Chromosome Res.* **29**, 245–260 (2021).
1058 21. Sladky, V. C., Eichin, F., Reiberger, T. & Villunger, A. Polyploidy control in hepatic
1059 health and disease. *J. Hepatol.* **75**, 1177–1191 (2021).
1060 22. Matondo, R. B. *et al.* Atypical E2f functions are critical for pancreas
1061 polyploidization. *PLoS One* **13**, e0190899 (2018).
1062 23. Bischof, C. *et al.* Mitochondrial-cell cycle cross-talk drives endoreplication in heart
1063 disease. *Sci. Transl. Med.* **13**, eabi7964 (2021).
1064 24. Matsumoto, T., Wakefield, L., Tarlow, B. D. & Grompe, M. In vivo lineage tracing of
1065 polyploid hepatocytes reveals extensive proliferation during liver regeneration. *Cell*
1066 *Stem Cell* **26**, 34–47.e3 (2020).
1067 25. Zhang, S. *et al.* The polyploid state plays a tumor suppressive role in the liver.
1068 *bioRxiv* (2017) doi:10.1101/149799.
1069 26. Hayashi, K. *et al.* Polyploidy mitigates the impact of DNA damage while
1070 simultaneously bearing its burden. *Cell Death Discov.* **10**, 436 (2024).
1071 27. Yekelchyk, M., Guenther, S., Preussner, J. & Braun, T. Mono- and multi-nucleated
1072 ventricular cardiomyocytes constitute a transcriptionally homogenous cell

population. *Basic Res. Cardiol.* **114**, 36 (2019).
28. Chen, R. J. *et al.* Towards a general-purpose foundation model for computational pathology. *Nat. Med.* **30**, 850–862 (2024).
29. Traag, V. A., Waltman, L. & van Eck, N. J. From Louvain to Leiden: guaranteeing well-connected communities. *Sci. Rep.* **9**, 5233 (2019).
30. Elz, A. E. *et al.* Evaluating the practical aspects and performance of commercial single-cell RNA sequencing technologies. *bioRxivorg* (2025) doi:10.1101/2025.05.19.654974.
31. De Simone, M. *et al.* A comprehensive analysis framework for evaluating commercial single-cell RNA sequencing technologies. *Nucleic Acids Res.* **53**, (2025).
32. Broadwell, L. J. *et al.* Myosin 7b is a regulatory long noncoding RNA (lncMYH7b) in the human heart. *J. Biol. Chem.* **296**, 100694 (2021).
33. Lee, L. A., Broadwell, L. J., Buvoli, M. & Leinwand, L. A. Nonproductive splicing prevents expression of MYH7b protein in the mammalian heart. *J. Am. Heart Assoc.* **10**, e020965 (2021).
34. Giampietri, C. *et al.* c-Flip overexpression reduces cardiac hypertrophy in response to pressure overload. *J. Hypertens.* **26**, 1008–1016 (2008).
35. Reichart, D. *et al.* Pathogenic variants damage cell composition and single cell transcription in cardiomyopathies. *Science* **377**, eabo1984 (2022).
36. Stringer, C. & Pachitariu, M. Cellpose3: one-click image restoration for improved cellular segmentation. *Nat. Methods* **22**, 592–599 (2025).
37. Greiner, J. *et al.* A deep learning-enabled toolkit for the 3D segmentation of ventricular cardiomyocytes. *J. Physiol.* (2025) doi:10.1113/JP288557.
38. Danaher, P. *et al.* Insitutype: likelihood-based cell typing for single cell spatial transcriptomics. *Bioinformatics* (2022).
39. Cable, D. M. *et al.* Robust decomposition of cell type mixtures in spatial transcriptomics. *Nat. Biotechnol.* **40**, 517–526 (2022).
40. Mages, S. *et al.* TACCO unifies annotation transfer and decomposition of cell identities for single-cell and spatial omics. *Nat. Biotechnol.* **41**, 1465–1473 (2023).
41. Aran, D. *et al.* Reference-based analysis of lung single-cell sequencing reveals a transitional profibrotic macrophage. *Nat. Immunol.* **20**, 163–172 (2019).
42. Mao, J., Deng, Y. & Lê Cao, K.-A. Φ-Space: Continuous phenotyping of single-cell multi-omics data. *Bioinformatics* (2024).
43. Joodaki, M. *et al.* Detection of PatIent-Level distances from single cell genomics and pathomics data with Optimal Transport (PILOT). *Mol. Syst. Biol.* **20**, 57–74 (2024).
44. Yoshioka, N. *et al.* Isoform-specific mutation in Dystonin-b gene causes late-onset protein aggregate myopathy and cardiomyopathy. *Elife* **11**, (2022).
45. Granzier, H. L. & Labeit, S. Discovery of titin and its role in heart function and disease. *Circ. Res.* **136**, 135–157 (2025).
46. Mah, C. K. *et al.* Bento: A toolkit for subcellular analysis of spatial transcriptomics data. *bioRxiv* 2022.06.10.495510 (2023) doi:10.1101/2022.06.10.495510.
47. Fazal, F. M. *et al.* Atlas of Subcellular RNA Localization Revealed by APEX-Seq. *Cell* **178**, 473–490.e26 (2019).
48. Scarborough, E., Uchida, K., Kehat, I. & Prosser, B. RNAs are localized and

1119 translated at discrete cardiomyocyte microdomains. *J. Mol. Cell. Cardiol.* **173**, S163
1120 (2022).
1121 49. Lu, F. *et al.* CMYA5 establishes cardiac dyad architecture and positioning. *Nat.*
1122 *Commun.* **13**, 2185 (2022).
1123 50. Baez, M. V. *et al.* Smaug1 mRNA-silencing foci respond to NMDA and modulate
1124 synapse formation. *J. Cell Biol.* **195**, 1141–1157 (2011).
1125 51. Hinnebusch, A. G. eIF3: a versatile scaffold for translation initiation complexes.
1126 *Trends Biochem. Sci.* **31**, 553–562 (2006).
1127 52. West, G., Sedighi, S., Agnetti, G. & Taimen, P. Intermediate filaments in the heart:
1128 The dynamic duo of desmin and lamins orchestrates mechanical force
1129 transmission. *Curr. Opin. Cell Biol.* **85**, 102280 (2023).
1130 53. Tsikitis, M. *et al.* Molecular insights into the role of desmin intermediate filament
1131 network in chromatin landscape, cardiomyocyte differentiation, and maturation. *Cell*
1132 *Death Dis.* **16**, 723 (2025).
1133 54. George, R. M. *et al.* Single cell evaluation of endocardial Hand2 gene regulatory
1134 networks reveals HAND2-dependent pathways that impact cardiac morphogenesis.
1135 *Development* **150**, (2023).
1136 55. Yang, C.-Y. *et al.* Reverse hierarchical DED assembly in the cFLIP-procaspase-8
1137 and cFLIP-procaspase-8-FADD complexes. *Nat. Commun.* **15**, 8974 (2024).
1138 56. Liu, D. *et al.* Cellular FADD-like IL-1β-converting enzyme-inhibitory protein
1139 attenuates myocardial ischemia/reperfusion injury via suppressing apoptosis and
1140 autophagy simultaneously. *Nutr. Metab. Cardiovasc. Dis.* **31**, 1916–1928 (2021).
1141 57. Russell, N. J. *et al.* Spatial ploidy inference using quantitative imaging. *Cell Rep.*
1142 *Methods* **5**, 101249 (2025).
1143 58. Stirling, D. R. *et al.* CellProfiler 4: improvements in speed, utility and usability. *BMC*
1144 *Bioinformatics* **22**, 433 (2021).
1145 59. Wehrens, M. *et al.* Single-cell transcriptomics provides insights into hypertrophic
1146 cardiomyopathy. *Cell Rep.* **39**, 110809 (2022).
1147 60. González-Velasco, O. *et al.* Identifying similar populations across independent
1148 single cell studies without data integration. *NAR Genom. Bioinform.* **7**, lqaf042
1149 (2025).
1150 61. Li, Z., Nagai, J. S., Kuppe, C., Kramann, R. & Costa, I. G. scMEGA: single-cell
1151 multi-omic enhancer-based gene regulatory network inference. *Bioinform Adv* **3**,
1152 vbad003 (2023).
1153 62. Gomez-Velazquez, M. *et al.* CTCF counter-regulates cardiomyocyte development
1154 and maturation programs in the embryonic heart. *PLoS Genet.* **13**, e1006985
1155 (2017).
1156 63. Cheng, M. *et al.* PHLOWER leverages single-cell multimodal data to infer complex,
1157 multi-branching cell differentiation trajectories. *Nat. Methods* **22**, 2328–2336 (2025).
1158 64. Velecela, V. *et al.* Epicardial cell shape and maturation are regulated by Wt1 via
1159 transcriptional control of Bmp4. *Development* **146**, dev178723 (2019).
1160 65. Ettou, S. *et al.* Epigenetic transcriptional reprogramming by WT1 mediates a repair
1161 response during podocyte injury. *Sci. Adv.* **6**, eabb5460 (2020).
1162 66. Marques, I. J. *et al.* Wt1 transcription factor impairs cardiomyocyte specification
1163 and drives a phenotypic switch from myocardium to epicardium. *Development* **149**,
1164 (2022).

1165 67. Renault, M.-A. *et al.* Gli3 regulation of myogenesis is necessary for ischemia-
1166 induced angiogenesis. *Circ. Res.* **113**, 1148–1158 (2013).
1167 68. Sakamoto, T. *et al.* A critical role for estrogen-related receptor signaling in cardiac
1168 maturation. *Circ. Res.* **126**, 1685–1702 (2020).
1169 69. Baruzzo, G., Cesaro, G. & Di Camillo, B. Identify, quantify and characterize cellular
1170 communication from single-cell RNA sequencing data with scSeqComm.
1171 *Bioinformatics* **38**, 1920–1929 (2022).
1172 70. Nagai, J. S., Leimkühler, N. B., Schaub, M. T., Schneider, R. K. & Costa, I. G.
1173 CrossTalkeR: analysis and visualization of ligand-receptorne tworks. *Bioinformatics*
1174 **37**, 4263–4265 (2021).
1175 71. Ruiz-Villalba, A. *et al.* Single-cell RNA sequencing analysis reveals a crucial role for
1176 CTHRC1 (collagen triple helix repeat containing 1) cardiac fibroblasts after
1177 myocardial infarction. *Circulation* **142**, 1831–1847 (2020).
1178 72. Razeghi, P. *et al.* Metabolic gene expression in fetal and failing human heart.
1179 *Circulation* **104**, 2923–2931 (2001).
1180 73. Farah, E. N. *et al.* Spatially organized cellular communities form the developing
1181 human heart. *Nature* **627**, 854–864 (2024).
1182 74. Lázár, E. *et al.* Spatiotemporal gene expression and cellular dynamics of the
1183 developing human heart. *Nat. Genet.* **57**, 2756–2771 (2025).
1184 75. Friedman, C. E. *et al.* Single-cell transcriptomic analysis of cardiac differentiation
1185 from human PSCs reveals HOPX-dependent cardiomyocyte maturation. *Cell Stem*
1186 *Cell* **23**, 586–598.e8 (2018).
1187 76. Knöll, R. *et al.* Telethonin deficiency is associated with maladaptation to
1188 biomechanical stress in the mammalian heart. *Circ. Res.* **109**, 758–769 (2011).
1189 77. Buettner, M., Ostner, J., Mueller, C. L., Theis, F. J. & Schubert, B. scCODA is a
1190 Bayesian model for compositional single-cell data analysis. *Nat. Commun.* **12**, 1–10
1191 (2021).
1192 78. Ren, F. *et al.* A small-molecule TNIK inhibitor targets fibrosis in preclinical and
1193 clinical models. *Nat. Biotechnol.* (2024) doi:10.1038/s41587-024-02143-0.
1194 79. Masuda, M. *et al.* TNIK inhibition abrogates colorectal cancer stemness. *Nat.*
1195 *Commun.* **7**, 12586 (2016).

1196

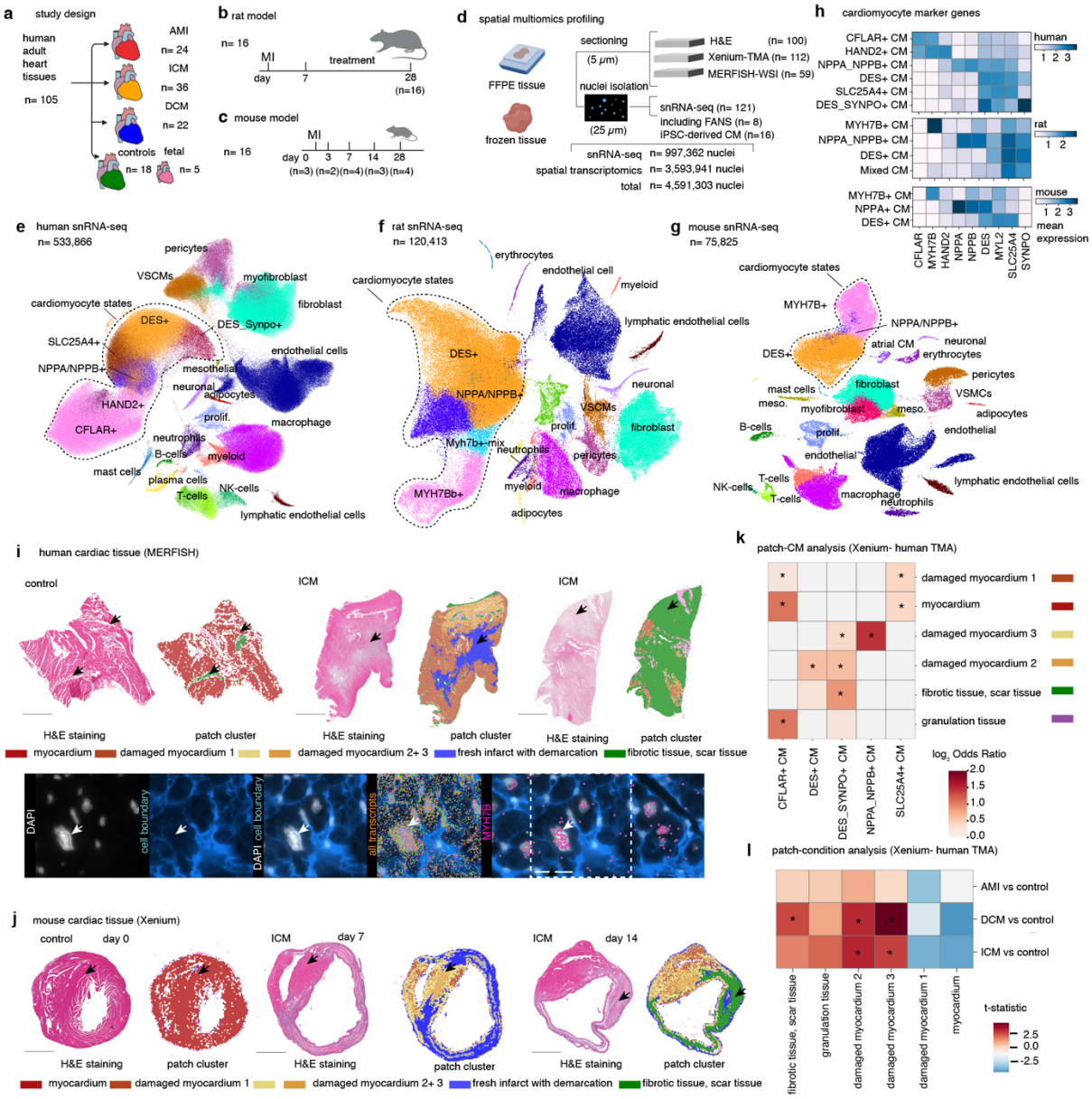

Figure 1 Cross-species single-nucleus and spatial multimodal atlas identifies conserved and human-specific cardiomyocyte states in heart disease. a, Study design and human cardiac tissue cohort. Adult human heart samples (n = 100) were obtained from non-failing controls, ischemic cardiomyopathy (ICM), dilated cardiomyopathy (DCM), and acute myocardial infarction (AMI), complemented by fetal heart samples (n = 5). **b,** Rat MI model. Hearts were harvested at day 7 post-MI and after treatment at day 28. **c,** Mouse myocardial infarction (MI) model. Hearts were collected at baseline and at multiple time points following MI (days 1, 3, 7, 14, and 28). **d,** Overview of spatial multimodal profiling. FFPE and frozen cardiac tissues were processed for histology (H&E), spatial transcriptomics (Xenium and MERFISH), and single-nucleus RNA sequencing (snRNA-seq). In total, 4,591,303 nuclei were profiled across snRNA-seq and spatial transcriptomics. **e,** UMAP embedding of human snRNA-seq data (n = 533,866 nuclei), colored by major cardiac cell types. Cardiomyocyte states are highlighted, including DES$^+$, NPPA/NPPB$^+$, SLC25A4$^+$, DES_SYNPO$^+$, HAND2$^+$, and CFLAR$^+$ cardiomyocytes. **f,** UMAP embedding of rat snRNA-seq data (n = 120,413 nuclei), revealing conserved cardiomyocyte states, including DES$^+$, NPPA/NPPB$^+$, MYH7B$^+$, and mixed cardiomyocyte populations. **g,** UMAP embedding of mouse snRNA-seq data (n = 75,825 nuclei), identifying DES$^+$, NPPA/NPPB$^+$, and MYH7B$^+$ cardiomyocyte states alongside non-myocyte populations. **h,** Heatmaps showing expression of selected cardiomyocyte marker genes across cardiomyocyte states in human (top), rat (middle), and mouse (bottom), highlighting conserved and species-specific transcriptional programs. Expression in logarithmic counts. **i,** Spatial mapping of cardiomyocyte patch clusters in human cardiac tissue using MERFISH. Representative H&E-stained sections and corresponding patch cluster annotations are shown for control and ICM samples. Bottom

panels show high-resolution MERFISH images with DAPI and selected marker genes (MYH7B). Scale bar indicates 1 mm. **j,** Spatial mapping of myocardial patch clusters in mouse hearts using Xenium across control, MI day 0, day 7, and day 14. H&E staining, patch cluster annotations, and spatial transcriptomic overlays are shown. Marker expression highlights cardiomyocyte and fibroblast-rich regions. Scale bar indicates 1 mm. **k,** Patch-level cardiomyocyte (path-CM) composition analysis in human Xenium tissue microarrays (TMAs), showing enrichment of cardiomyocyte states across myocardial, damaged myocardium, fibrotic/scar, and granulation tissue regions. Asterisks indicate statistically significant enrichments. Significance was determined by Fisher's exact test with adjusted p-values < 0.05. **l,** Patch-condition analysis comparing AMI, DCM, and ICM to controls in human Xenium TMAs, revealing condition-specific enrichment of myocardial damage and fibrotic tissue states. Significance was determined by t-test with adjusted p-values < 0.05. Asterisks denote statistically significant differences.

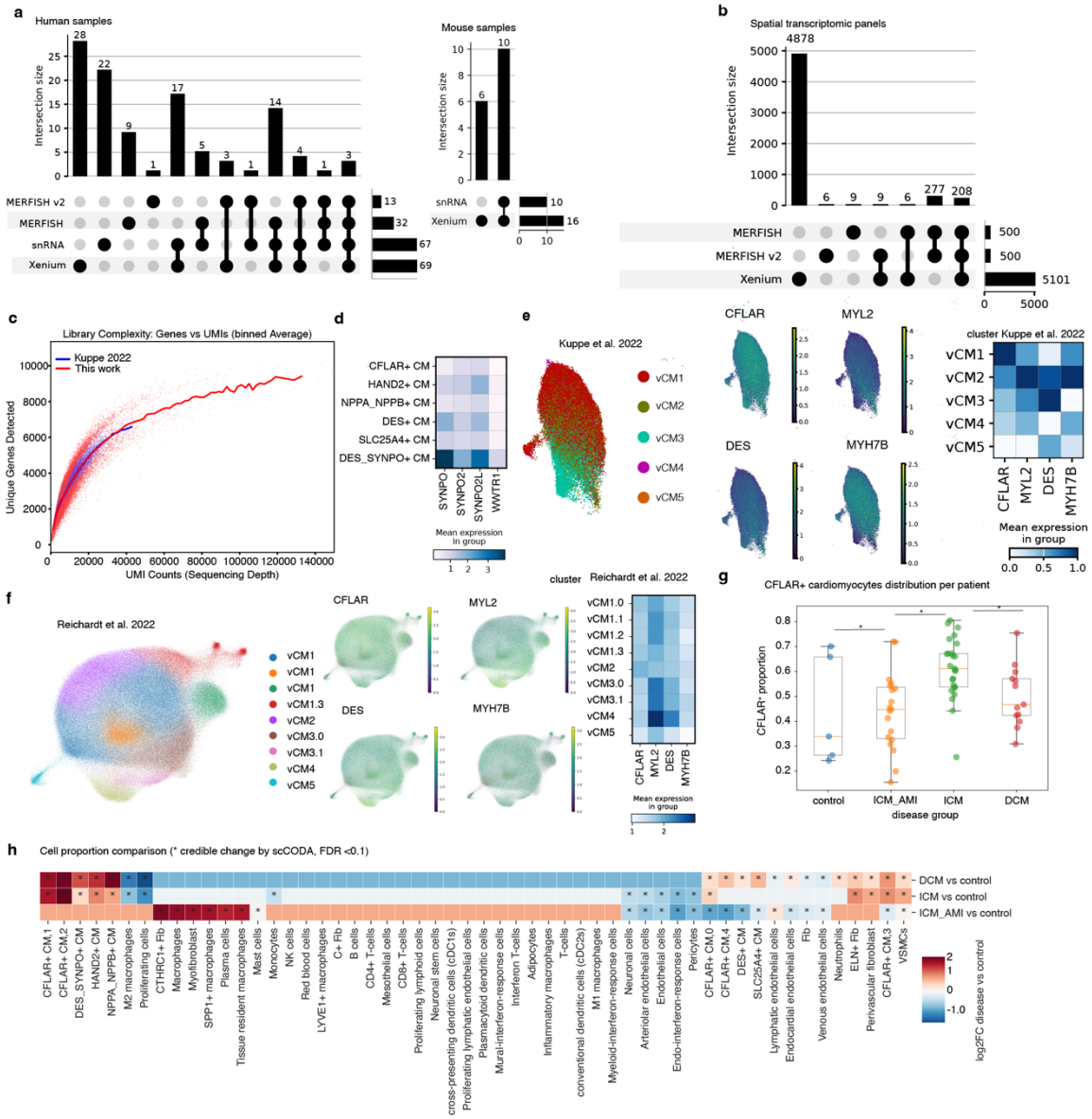

ED Data Figure 1 Cross-species identification and segregation analysis of CFLAR⁺ cardiomyocytes across spatial and single-nucleus datasets. a, Overview of human (left panel) and mouse (right panel) cardiac datasets used in this study. Bar plots indicate the number of samples per modality, including Xenium, snRNA-seq, MERFISH and MERFISH V2.0. UpSet-style plots summarize dataset overlap and availability across modalities in human and mouse hearts. **b,** Overview of the spatial transcriptomic panels used and their overlap. **c,** Comparison of library complexity with Kuppe et al., 2022. The gene detected by counts per nucleus slope is comparable, while this dataset shows a higher top end. **d,** Heatmaps showing mean expression of SYNPO, SYNPO2, SYNPO2L, and WIF1 across major cardiomyocyte (CM) subtypes in human. DES_SYNPO⁺ CMs display selective enrichment of SYNPO family genes, indicating a distinct cytoskeletal-associated CM program conserved across species. **e,** Projection of cardiomyocyte nuclei from Kuppe et al., 2022 onto a low-dimensional embedding, annotated by CM clusters. Feature plots illustrate expression of CFLAR, MYL2, DES, and MYH7B. The accompanying heatmap summarizes mean gene expression per CM cluster, highlighting segregation of CFLAR⁺ CMs from classical contractile CM states. **f,** Independent validation in the Reichardt et al., 2022 human ventricular cardiomyocyte dataset. Left, UMAP embedding of ventricular CM subclusters, where clusters are name as in the original publication (vCM0–vCM5). Middle, feature plots showing expression of CFLAR, MYL2, DES, and MYH7B. Right, heatmap of scaled mean

expression per vCM subtype, confirming selective enrichment of CFLAR and MYH7B in distinct CM populations. **g,** Quantification of the ratio of $CFLAR^+$ to DES^+ cardiomyocytes across disease conditions (control, ischemic cardiomyopathy with acute myocardial infarction (ICM_AMI), ischemic cardiomyopathy (ICM), and dilated cardiomyopathy (DCM)). Each dot represents one patient sample, illustrating disease-associated shifts in CM state composition. Stars indicate a FDR<0.1 based on scCODA abundance test. **h,** Differential cell-type proportion analysis across disease groups. Heatmap depicts log-fold changes in relative cell abundance between pairwise disease comparisons. Asterisks indicate credible changes by the scCODA test (False Discovery Rate=0.1). $CFLAR^+$ CM populations show selective expansion in cardiomyopathy compared to control hearts, while other CM and non-CM populations display distinct disease-specific remodeling patterns.

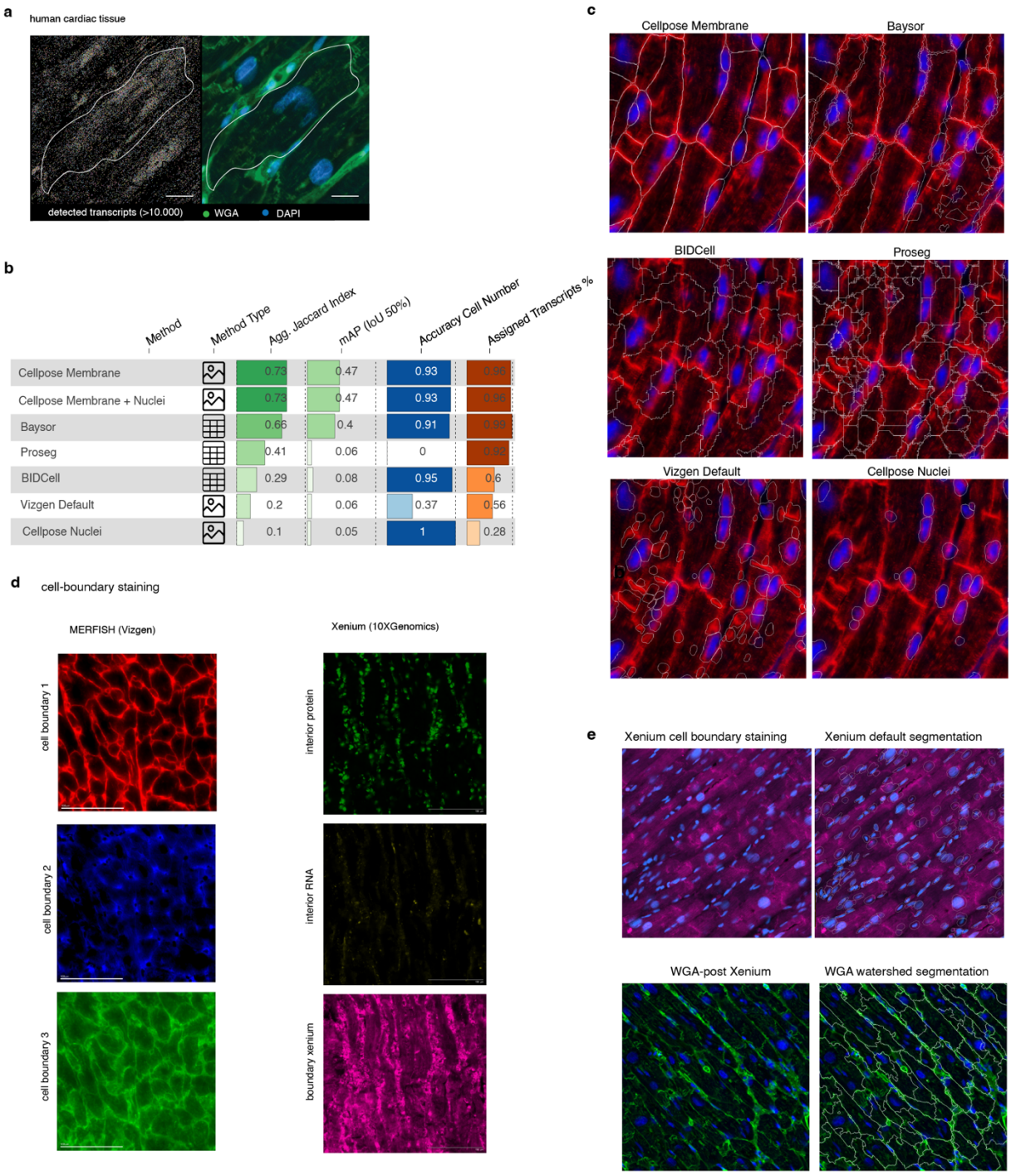

Extended Data Figure 2 Cardiac tissue segmentation optimization.

a, Representative human cardiac tissue section profiled by high-resolution spatial transcriptomics Xenium 5k. Left, spatial distribution of detected transcripts (>10,000) within a manually outlined cardiomyocyte. Right, corresponding immunofluorescence image showing wheat germ agglutinin (WGA, cell boundaries; green) and DAPI (nuclei; blue). Scale 10 um. **b,** Quantitative comparison of segmentation methods using image-based and feature-based metrics. Image metrics include aggregated Jaccard index and mean average precision (mAP, IoU ≥50%) relative to reference annotations. Feature metrics include accuracy of cell number estimation (vs nucleus segmentation) and fraction of assigned transcripts. Cellpose's membrane-based approaches achieve the best overall

balance between spatial accuracy and transcript assignment, whereas nucleus-only and default platform segmentations underperform in cardiomyocyte-dense tissue. **c,** Visual comparison of segmentation outputs overlaid on cardiac tissue images (segmented boundaries in white). Methods include Cellpose (membrane), Baysor, BIDCell, Proseg, Vizgen default segmentation, and Cellpose nuclei. Membrane-aware methods more accurately capture elongated cardiomyocyte morphology and reduce over-segmentation. **d,** Comparison of cell-boundary staining strategies for spatial transcriptomics platforms. MERFISH (Vizgen), left section, relies on intrinsic membrane signal, whereas Xenium (10X Genomics), right section, benefits from additional post-hoc membrane labeling to improve boundary definition in cardiomyocytes. **e,** Xenium cardiac tissue segmentation comparison. Top, default Xenium cell boundary staining and segmentation. Bottom, post-Xenium WGA staining followed by watershed segmentation, resulting in improved delineation of elongated cardiomyocytes and more accurate cell boundaries.

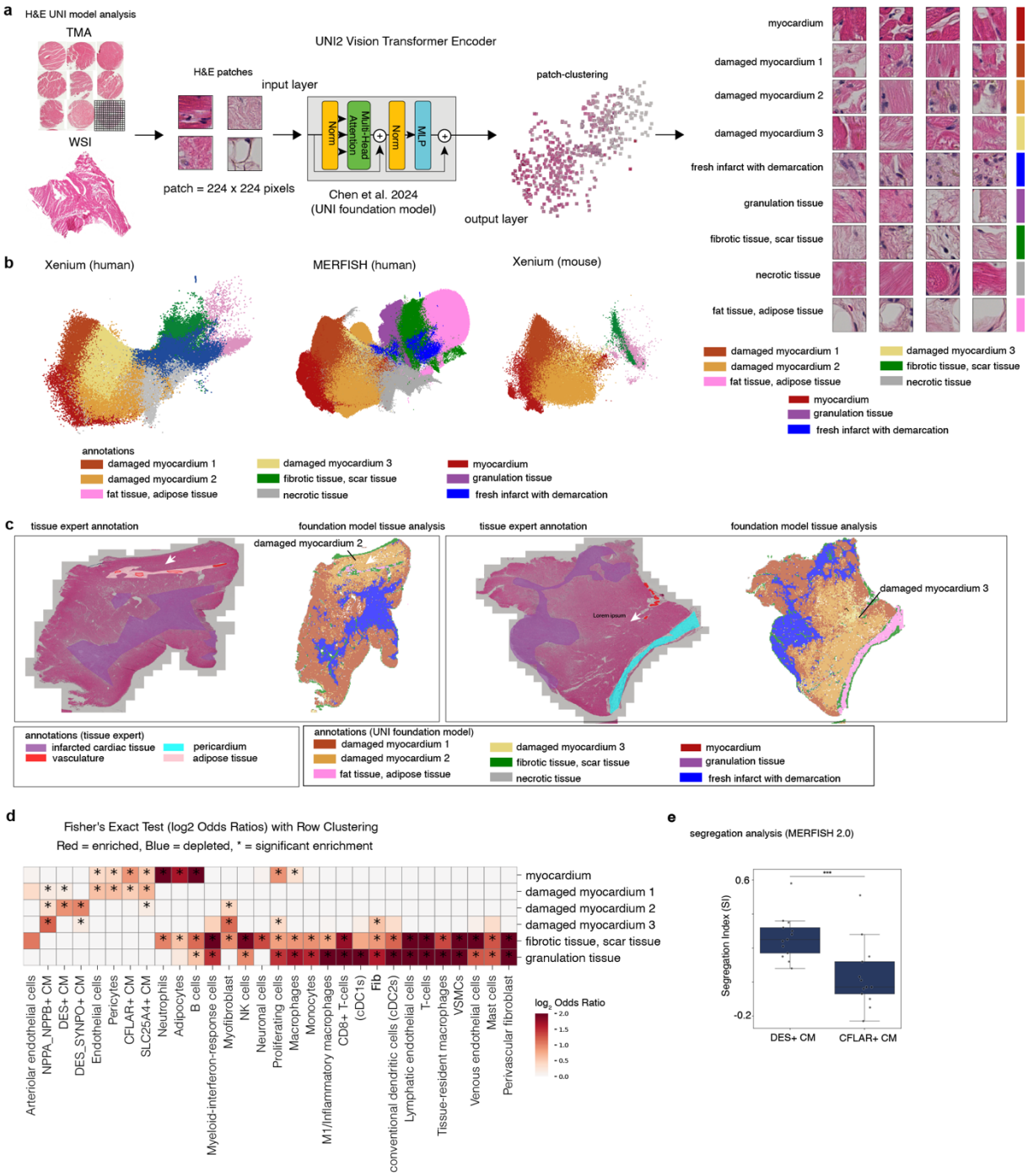

Extended Data Figure 3 Histopathology foundation model–based tissue state annotation across spatial transcriptomics platforms. a, Schematic overview of the histology-based tissue classification workflow using a deep learning foundation model. Whole-slide images (WSI) and tissue microarrays (TMA) stained with haematoxylin and eosin (H&E) were subdivided into non-overlapping image patches (224 × 224 pixels) and embedded using the UNI transformer foundation model (Chen *et al.*, 2024). Latent representations were clustered in an unsupervised manner to define recurrent myocardial tissue states, including intact myocardium, multiple damaged myocardium states, fresh infarct with demarcation, granulation tissue, fibrotic scar tissue, necrotic tissue, and adipose tissue. Representative image patches for each tissue state are shown. **b,** Joint embedding of spatial transcriptomics data annotated by foundation model–derived tissue classes across platforms and species. UMAP projections of Xenium (human), MERFISH (human), and Xenium (mouse) datasets demonstrate consistent

segregation of myocardial tissue states, indicating cross-platform and cross-species robustness of the histology-driven tissue classification. **c,** Comparison of expert tissue annotation and foundation model–based tissue analysis on whole heart sections. Left, tissue expert annotations highlighting infarcted cardiac tissue, vasculature, adipose tissue, and pericardium. Right, corresponding foundation model predictions resolving fine-grained myocardial damage states and infarct-associated tissue regions. Arrows indicate regions of concordance and refined subclassification by the model. **d,** Association between tissue states and cellular composition. Heatmap showing enrichment and depletion of cell types within foundation model–defined tissue regions using Fisher's exact test ($\log_2$ odds ratios). Red indicates enrichment, blue depletion; asterisks denote statistically significant associations after multiple-testing correction (adjusted p-values < 0.05). Fibrotic and granulation tissue regions are enriched for fibroblasts, macrophages, endothelial, and perivascular cells, whereas intact myocardium is selectively associated with cardiomyocyte populations. **e,** Segregation analysis of cardiomyocyte subtypes in MERFISH 2.0 data (n=13). Segregation index (SI) comparison shows significantly stronger spatial segregation (clumping) of DES^+ cardiomyocytes compared with $CFLAR^+$ cardiomyocytes, indicating differential spatial organization relative to tissue damage states. Box plots show median, interquartile range, and individual samples; *** p-value < 0.001 Wilcoxon rank-sum test.

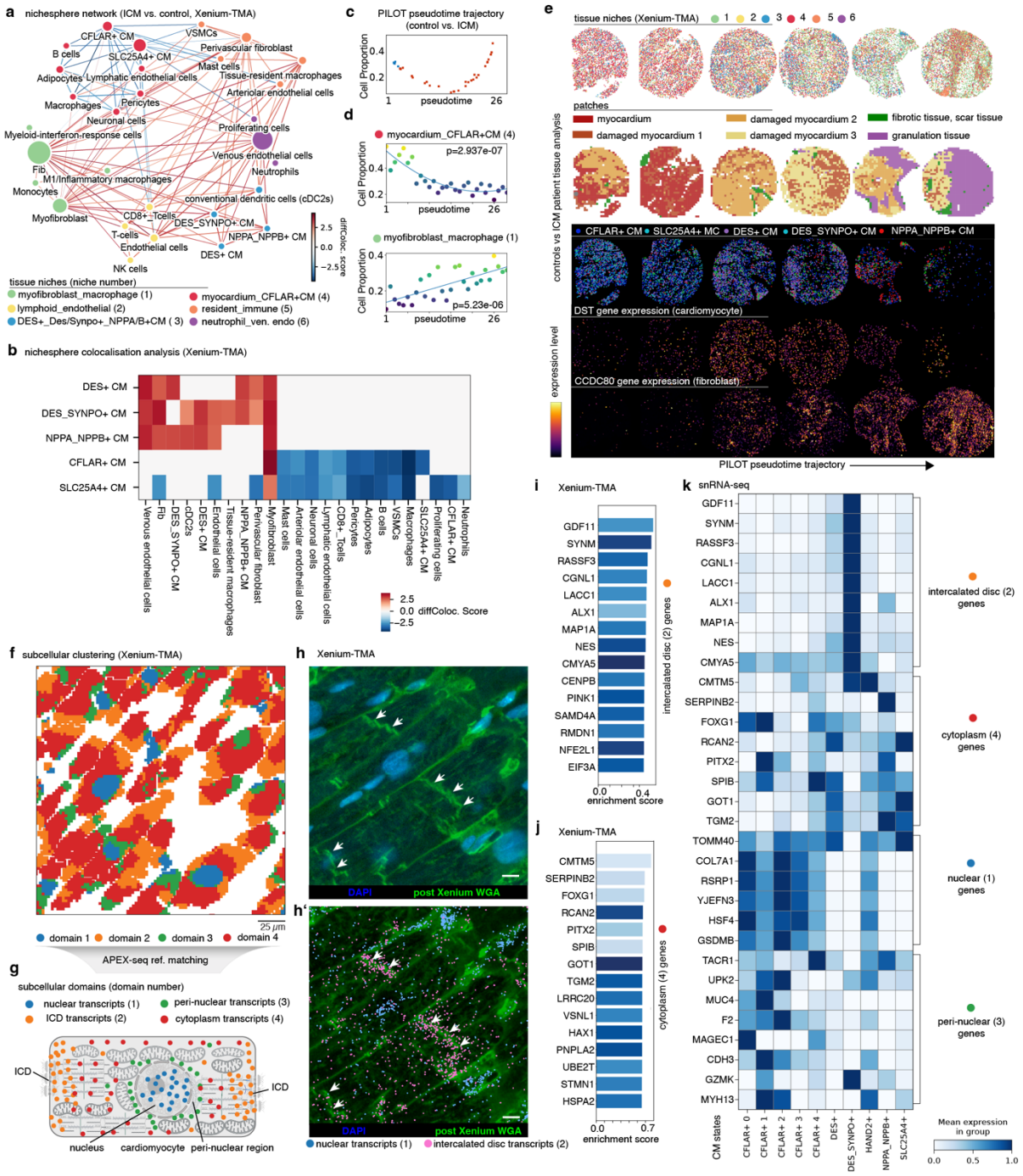

Figure 2 Spatial tissue niches and subcellular transcript organization reveal cardiomyocyte state–specific remodeling in cardiomyopathy. a, NicheSphere interaction network control vs. ICM. Network representation of spatial tissue niches inferred from Xenium-TMA sections comparing ischemic cardiomyopathy (ICM) with controls. Nodes represent cell-type–specific niches and edges indicate significantly altered spatial interactions, with red and blue edges denoting increased or decreased interactions in ICM, respectively. **b,** Spatial colocalization analysis. Heatmap of differential colocalization (diffColoc score) between cardiomyocyte (CM) states and other cardiac cell types across Xenium-TMA samples. For **a** and **b**, only statistically significant interactions are shown (adjusted Wilcoxon's rank sums test; p-value < 0.05). **c,** PILOT pseudotime trajectory (control as blue dots vs. ICM as red dots)**.** Trajectory of TMA samples illustrating progressive niche remodeling from control to ICM tissue states. **d,** Niche proportion changes along pseudotime. Changes in relative abundance (y-axis) of myocardium-associated CFLAR^{+} CMs (top) and myofibroblast–macrophage niches (bottom) along pseudotime (x-axis), indicating reciprocal dynamics during disease progression (p-value - goodness of fit test on the

regression of the cell proportion and pseudo-time). **e,** Tissue niche composition across six selected Xenium-TMA samples along the Trajectory from early to middle and late stages. Spatial maps showing niche assignments (top), histopathology-based tissue annotation (middle; myocardium, damaged myocardium, fibrotic and granulation tissue), and CM state distributions (bottom) across selected control and ICM samples. Representative gene expression patterns of genes with trajectory expressific changes are shown: DST (cardiomyocytes) and CCDC80 (fibroblasts) . **f,** Subcellular clustering. Spatial clustering of transcripts within cardiomyocytes identifies four recurrent subcellular domains across Xenium-TMA sections. Scale bar, 25 μm. **g,** Reference-based domain annotation**.** Mapping of Xenium-derived subcellular domains to APEX-seq reference signatures, assigning nuclear, intercalated disc (ICD), peri-nuclear, and cytoplasmic transcript compartments. **h,** Imaging validation of subcellular domains. Post-Xenium wheat germ agglutinin (WGA) staining and DAPI highlighting cardiomyocyte structure and nuclei, with arrows indicating enrichment of domain-specific transcripts. Bottom panel shows spatial localization of nuclear and ICD-associated transcripts. **i,** ICD-associated gene enrichment. Bar plot of genes enriched in intercalated disc–associated transcripts identified in Xenium-TMA data. **j,** Cytoplasmic gene enrichment. Bar plot of genes enriched in cytoplasmic transcript domains in Xenium-TMA data. **k,** snRNA-seq validation of subcellular gene programs. Heatmap showing mean expression of domain-specific genes across CM states in snRNA-seq data, confirming nuclear, peri-nuclear, cytoplasmic, and ICD-associated transcriptional programs. Particular enrichment is found of ICD domain 2 associated transcripts in DES_SYNPO+ CMs.

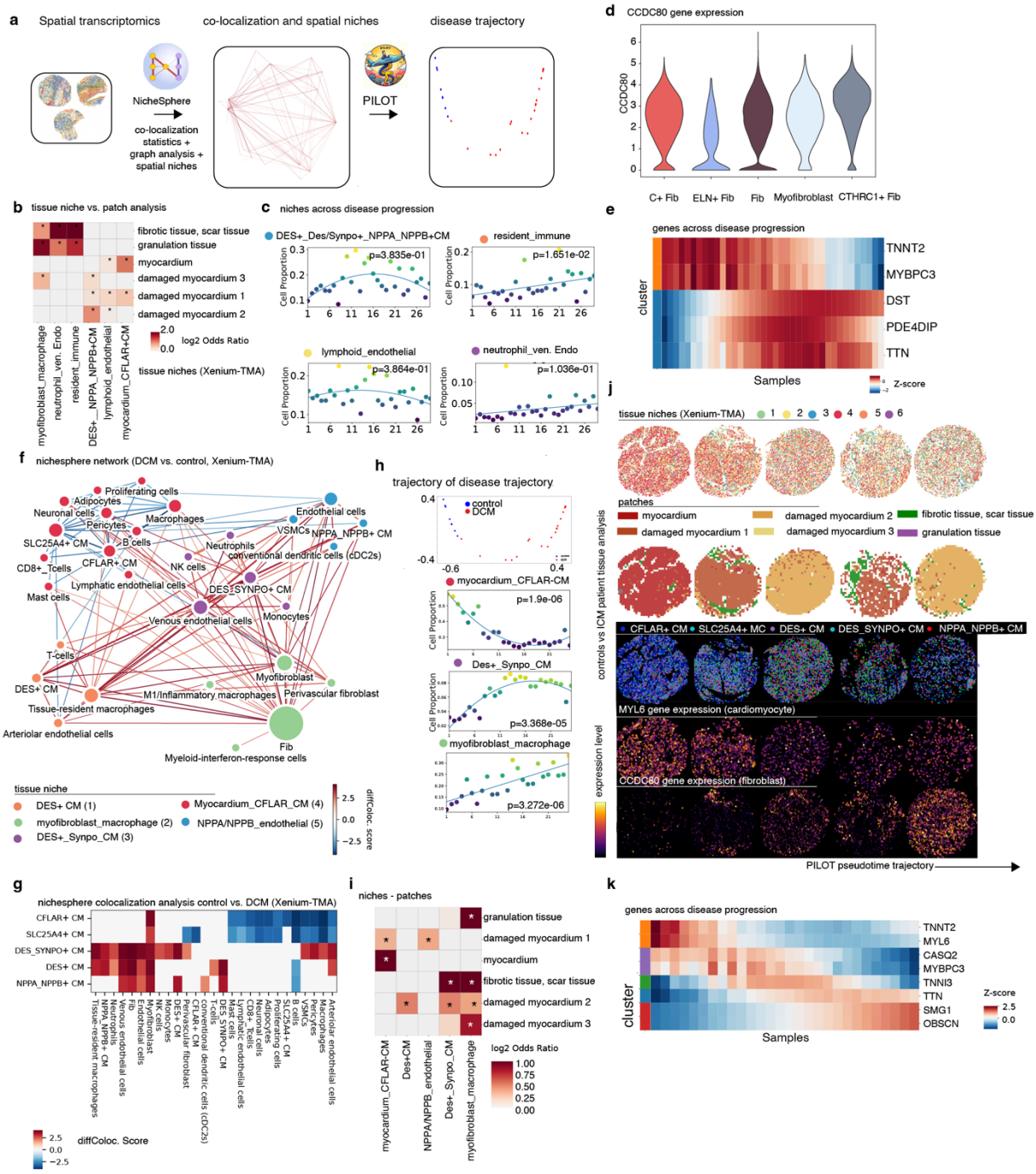

Extended Data Figure 4 Spatial niche remodeling and disease trajectory in human cardiomyopathy. a, Overview of the spatial transcriptomics workflow. Xenium spatial transcriptomic data from control and ischemic cardiomyopathy (ICM) samples were analyzed using the NicheSphere framework to quantify cell–cell colocalization, graph-based interactions, and to define spatial tissue niches. TMA samples were subsequently ordered along a disease trajectory using PILOT pseudotime analysis in accordance to their niches. **b,** Comparison of tissue niche composition versus patch-based histological annotation. Heatmap shows enrichment of defined tissue niches (Xenium-TMA) across histopathological regions, including myocardium, damaged myocardium (subtypes 1–3), fibrotic/scar tissue, and granulation tissue. Asterisks indicate statistical significance (adjusted p-value < 0.05; Fisher's exact test). **c,** Changes in niche composition (y-axis) across disease progression (x-axis). Scatter plots show proportions of selected niches along the inferred disease trajectory, including

DES$^+$/DES_SYNPO$^+$/NPPA_NPPB$^+$ cardiomyocytes, resident immune niches, lymphoid endothelial niches, and neutrophil–venous endothelial niches. Lines indicate smoothed trends; p-values from F statistic test denote significance of association with disease progression. **d,** Violin plots of CCDC80 gene expression (normalized log counts) across major fibroblast-related cell states in snRNA, including C7$^+$ fibroblasts, ELN$^+$ fibroblasts, general fibroblasts, myofibroblasts, and CTHRC1$^+$ fibroblasts. **e,** Heatmap with genes selected (by PILOT) to be associated with the trajectory in CFLAR CM cells. They include cardiomyocyte structural and cytoskeletal genes across disease progression, illustrating coordinated downregulation of sarcomeric genes (e.g., *TNNT2*, *MYBPC3*) and upregulation of remodeling-associated genes (e.g., *DST*, *PDE4DIP*, *TTN*). **f,** NicheSphere interaction network comparing DCM and control samples (Xenium-TMA). Nodes represent cell types or niches, edges represent differential co-localization scores, and edge color indicates increased (red) or decreased (blue) interactions in disease. **g,** Differential co-localization heatmap showing changes in spatial associations between cardiomyocyte states and surrounding cell types in control versus DCM samples. Color scale indicates diffColoc scores. For **f** and **g**, only statistically significant interactions are shown(adjusted Wilcoxon's rank sums test; p-value < 0.05). **h,** Top, disease trajectory using PILOT pseudotime analysis, Bottom, Proportional changes of selected cardiomyocyte-centered niches along disease progression, including myocardium_CFLAR$^+$ cardiomyocytes, DES_SYNPO$^+$ cardiomyocytes, and myofibroblast–macrophage niches. Trend lines and p-values indicate significant associations with pseudotime. **i,** Association between spatial niches and histological patches. Heatmap displays the fraction of each niche within defined tissue patches, highlighting preferential localization of cardiomyocyte niches to myocardium and damaged myocardium, and fibroblast–immune niches to fibrotic or granulation tissue. Significance was determined by Fisher's exact test with adjusted p-values ($p < 0.05$). **j,** Representative Xenium-TMA sections (five selected samples along the Trajectory from early to middle and late stages) illustrating (top) spatial distribution of tissue niches, (middle) corresponding histopathological patches, and (bottom) cardiomyocyte subtype localization and marker gene expression. MYL6 expression highlights cardiomyocytes, whereas CCDC80 expression marks fibroblast-rich regions. Arrow indicates progression along the PILOT pseudotime trajectory. **k,** Heatmap of cardiomyocyte gene expression dynamics across disease progression, showing gradual loss of contractile gene programs (e.g., *TNNT2*, *MYL6*, *CASQ2*, *MYBPC3*) and induction of stress and remodeling-associated genes (e.g., *SMG1*, *OBSCN*).

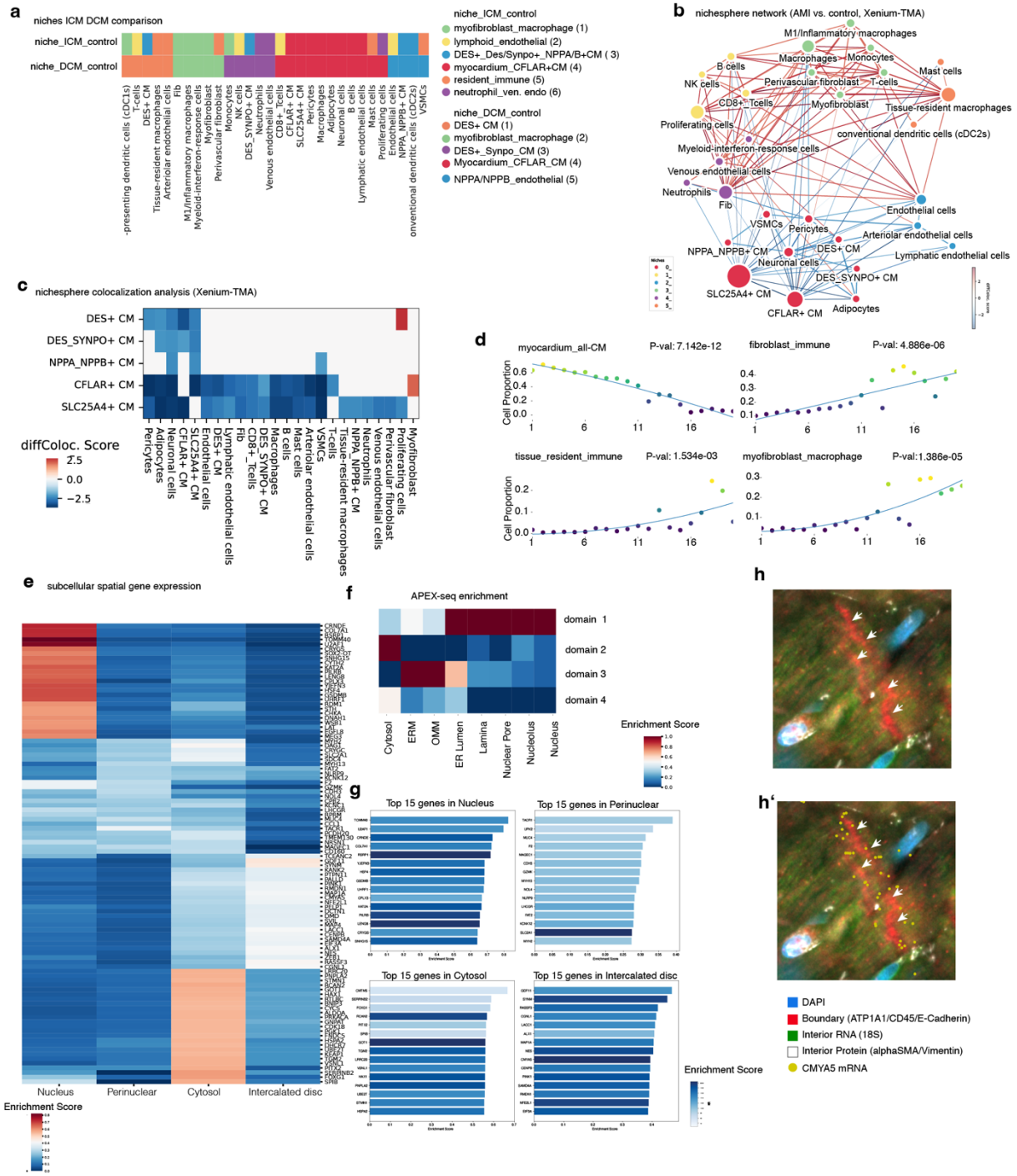

Extended Data Figure 5 Differential spatial niches and subcellular RNA organization in cardiomyopathy. a, Heatmap summarizing differences in spatial niche composition between ischemic cardiomyopathy (ICM)/DCM and control samples. Columns represent annotated cell types, rows indicate identified spatial niches. **b,** NicheSphere interaction network comparing acute myocardial infarction (AMI) with control samples (Xenium-TMA). Nodes represent cell types, edges indicate differential spatial co-localization, with red edges denoting increased and blue edges decreased interactions in disease. Edge thickness corresponds to the magnitude of the differential co-localization score. **c,** Differential co-localization analysis of cardiomyocyte subtypes in Xenium-TMA data. Heatmap displays diffColoc scores for DES^{+}, DES_SYNPO^{+}, NPPA_NPPB^{+}, CFLAR^{+}, and SLC25A4^{+} cardiomyocytes with surrounding cell types, highlighting disease-associated remodeling of cardiomyocyte neighborhoods. **d,** Proportional changes of niches along disease progression. **e,** Heatmap of subcellular spatial gene expression patterns in cardiomyocytes. Genes are ordered by preferential enrichment across four subcellular compartments—nucleus, perinuclear region, cytosol, and intercalated disc—revealing compartment-specific transcript localization programs. **f,** Enrichment of APEX-seq–derived subcellular reference signatures across the four identified RNA domains. Heatmap shows concordance of spatial transcript localization with known cytosolic, ER membrane (ERM), outer

mitochondrial membrane (OMM), ER lumen, lamina, nuclear pore, nucleolus, and nucleus-associated RNA signatures. **g,** Top 15 genes enriched in each subcellular compartment (nucleus, perinuclear region, cytosol, and intercalated disc), ranked by enrichment score, highlighting distinct functional gene sets underlying compartment-specific RNA localization. **h,** Representative high-resolution microscopy image illustrating cardiomyocyte subcellular architecture. White arrows indicate intercalated disc regions. Nuclei are counterstained with DAPI (blue). **h′,** Same field of view as in **h**, overlaid with detected CMYA5 mRNA molecules (yellow dots), demonstrating preferential localization of CMYA5 transcripts at intercalated disc regions. Boundary markers (ATP1A1/CD45/E-cadherin), interior RNA (18S), and interior protein markers (alphaSMA/Vimentin) are shown as indicated in the legend.

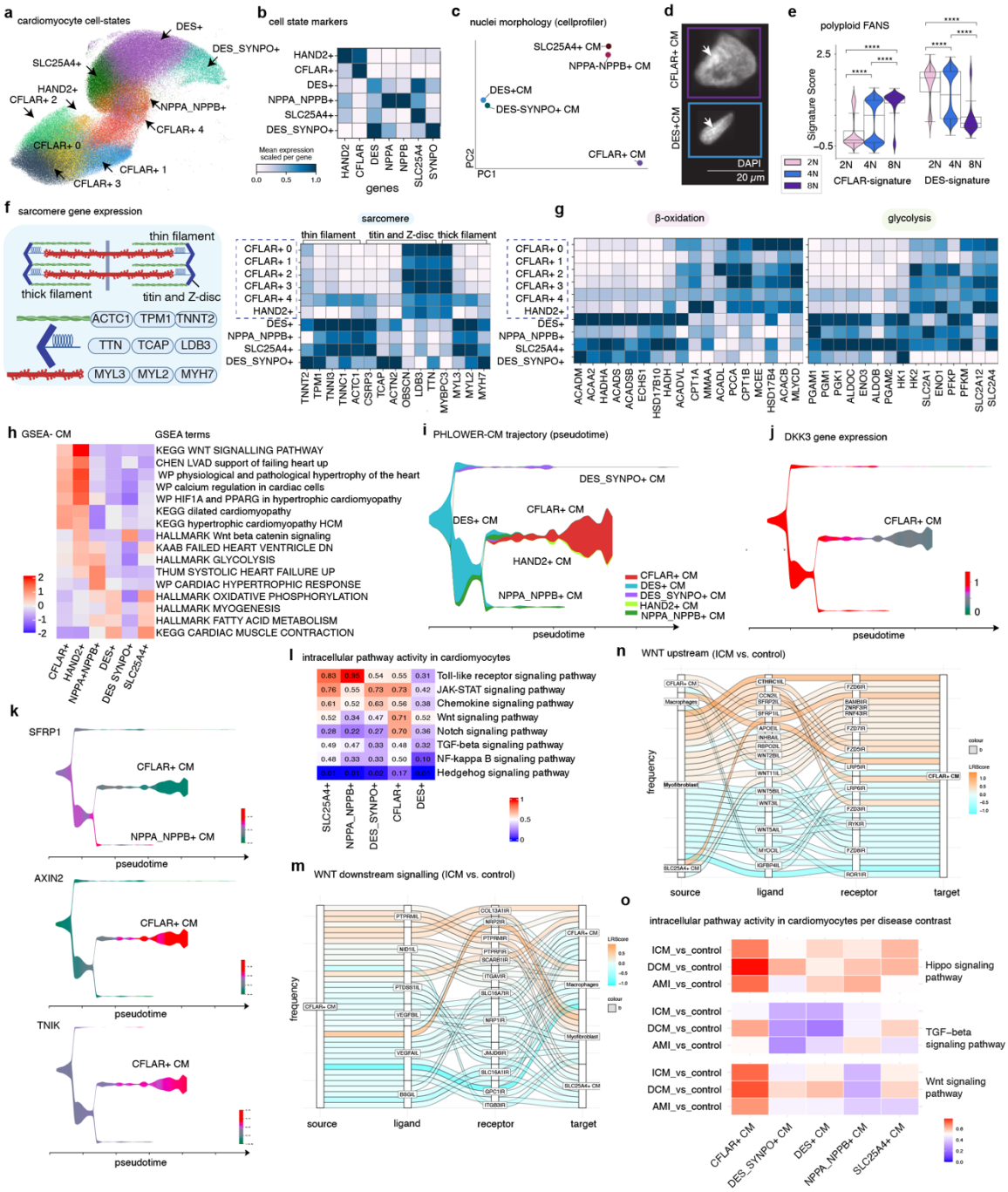

Figure 3 Molecular, structural, metabolic, and signaling features of novel human cardiomyocyte cell states. a, UMAP embedding of snRNA-seq highlighting distinct CM populations, including CFLAR^{+}, DES^{+}, DES_SYNPO^{+}, HAND2^{+}, NPPA_NPPB^{+}, and SLC25A4^{+} CMs. Arrows indicate cluster identities. **b,** Cell state marker genes. Heatmap showing scaled mean expression of representative marker genes across CM states, confirming transcriptional distinctions between CMs. **c,** Nuclei morphology analysis. PCA of CellProfiler-derived nuclear morphology features from DAPI staining separates CM states, indicating systematic differences in nuclear shape and size across transcriptional identities. **d,** Representative nuclei images. Immunofluorescence images of DES^{+} and CFLAR^{+} cardiomyocyte nuclei illustrating distinct nuclear morphologies (arrows). Scale bar, 20 µm. **e,** Polyploidy enrichment using FANS. Violin plots of cell-state signature scores across nuclei with different ploidy levels (2N, 4N, 8N) obtained by FANS. CFLAR and DES signature enrichment differs by ploidy state (p-value < 0.0001). **f,** Sarcomere gene expression. Schematic of sarcomeric organization (thin filaments, thick filaments, titin and Z-disc) and heatmap of corresponding gene expression across CM states, highlighting differential regulation of structural components. **g,** Metabolic gene programs. Heatmaps showing expression of

genes involved in β-oxidation (left) and glycolysis (right) across CM states, indicating metabolic specialization. **h,** Gene set enrichment analysis (GSEA) of hallmark, KEGG, and WikiPathways terms across CM states, revealing differences in hypertrophic signaling, metabolism, WNT signaling, and cardiac contraction programs. **i,** Differentiation trajectory of CM states. PHLOWER-based trajectory inference depicting transitions between CM states along pseudotime, with relative contributions of $CFLAR^+$, DES^+, DES_SYNPO^+, $HAND2^+$, and $NPPA_NPPB^+$ CMs. **j,** DKK3 expression dynamics. Smoothed expression of DKK3 along the CM pseudotime trajectory, highlighting state-specific regulation. **k,** WNT pathway–related genes along cardiomyocyte trajectories. Expression dynamics of SFRP1, AXIN2, and TNIK across CM states along pseudotime, illustrating coordinated regulation of WNT signaling components. **l,** Intracellular pathway activity (ICM vs. control). Heatmap summarizing inferred intracellular activity scores of key signaling pathways (e.g., Toll-like receptor, JAK–STAT, WNT, TGF-β, NF-κB, Hedgehog) across CM states, highlighting differential transcriptional response between ICM versus control hearts. **m,** WNT upstream signaling (ICM vs. control). Sankey plot display ligand-receptor interactions upstream of WNT signalling in CFLAR+ CM cells, comparing ICM with control hearts. Positive values indicate increased signaling strength in ICM, whereas negative values indicate reduced interaction strength. **n,** Cell-cell communication downstream of WNT signaling (ICM vs. control). Sankey plot displaying ligand–receptor interactions downstream of WNT pathway in CFLAR+ CM cells comparing ischemic cardiomyopathy (ICM) compared with controls; ligands correspond to transcriptional targets of WNT signaling. **o,** Disease-specific pathway activity. Heatmap of inferred intracellular pathway activity across CM states comparing ischemic cardiomyopathy (ICM), dilated cardiomyopathy (DCM), and acute myocardial infarction (AMI) with controls, focusing on Hippo, TGF-β, and WNT signaling pathways.

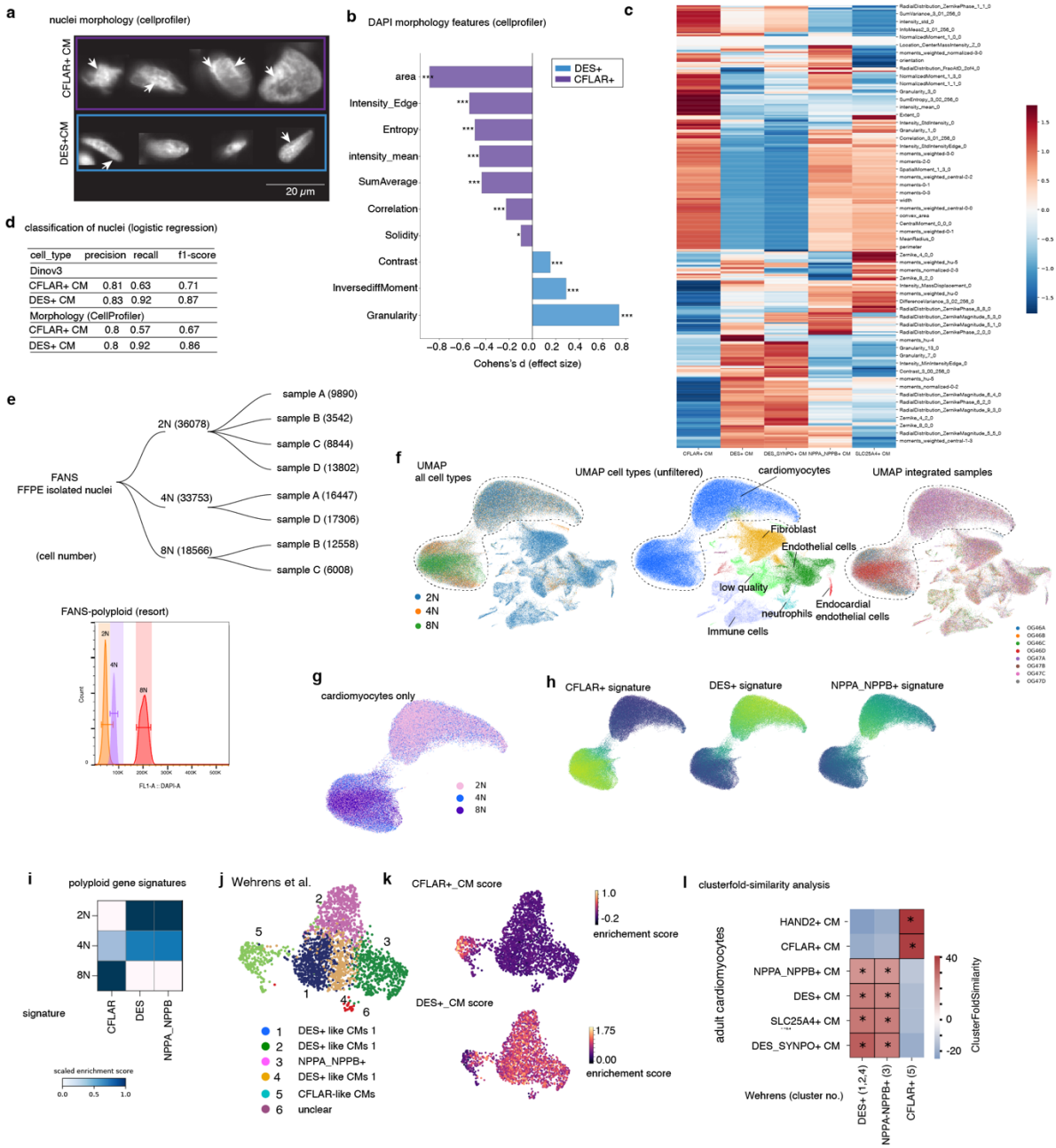

Extended Data Figure 6 Nuclear morphology–based classification and polyploidy-associated cardiomyocyte programs. a, Representative nuclear morphologies. DAPI images of isolated cardiomyocyte nuclei from CFLAR$^+$ and DES$^+$ CMs illustrating distinct nuclear shapes and texture features (arrows). Scale bar, 20 µm. **b,** Quantitative nuclear morphology features. Comparison of selected CellProfiler-derived DAPI morphology features between DES$^+$ and CFLAR$^+$ CM nuclei. Bars indicate Cohen's *d* effect size; positive values indicate enrichment in DES$^+$, negative values enrichment in CFLAR$^+$ nuclei. p-values from two-sided tests (p-value< 0.05; p-value < 0.001). **c,** Morphology feature heatmap. Heatmap of z-scored DAPI morphology features across cardiomyocyte states (DES$^+$, DES_SYNPO$^+$, CFLAR$^+$, NPPA_NPPB$^+$, SLC25A4$^+$), highlighting systematic differences in size, texture, shape, and Zernike moments. **d,** Performance of morphology-based classification (logistic regression). Precision, recall, and F1-score for distinguishing CFLAR$^+$ and DES$^+$ CMs using either DINOV3 feature vectors (top) or CellProfiler based nuclear morphology measurements (bottom). **e,** Polyploid nuclei isolation by FANS. Experimental overview and cell numbers of fluorescence-activated nuclei sorting (FANS) from FFPE samples into 2N, 4N, and 8N fractions, including sample-specific contributions. Bottom panel shows representative DNA content distributions. **f,** Integrated single-nucleus landscape. UMAP embedding of all cardiac cell types (left), annotated cell types with cardiomyocytes

highlighted (middle), and integrated samples colored by donor (right). **g,** Cardiomyocyte-only embedding. UMAP representation restricted to cardiomyocytes, capturing continuous transcriptional variation across CM states. **h,** Cell-state signature projection. UMAPs showing enrichment of CFLAR$^+$, DES$^+$, and NPPA_NPPB$^+$ gene signatures across cardiomyocytes. **i,** Polyploid gene signatures. Heatmap summarizing enrichment of CFLAR, DES, and NPPA_NPPB signatures across ploidy classes (2N, 4N, 8N). **j,** External CM classification reference Wehrens et al.. UMAP of cardiomyocytes annotated according to the classification by Wehrens *et al.*, showing correspondence to DES-like, NPPA_NPPB$^+$, CFLAR-like, and unclassified CM populations. **k,** Signature score validation. UMAPs displaying CFLAR$^+$ CM and DES$^+$ CM signature scores, confirming spatial separation of CM programs. **l,** Cluster fold-similarity analysis. Heatmap showing similarity between adult human CM states and reference DES$^+$ or CFLAR$^+$ programs. Asterisks denote significant enrichment ($P < 0.05$).

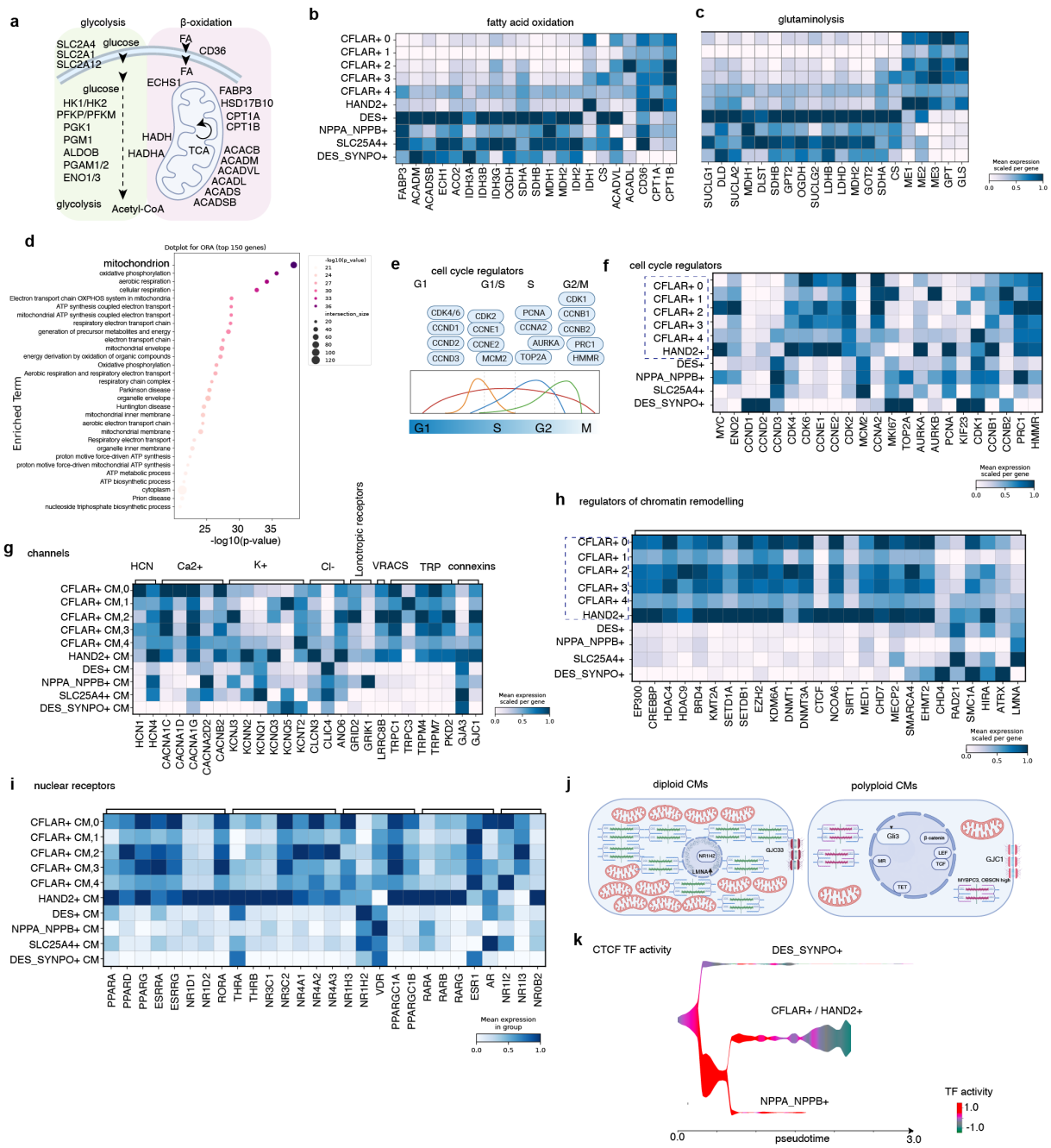

Extended Data Figure 7 Metabolic, cell-cycle, electrophysiological, and epigenetic programs distinguish diploid and polyploid cardiomyocyte states. a, Schematic overview of central metabolic pathways analyzed in cardiomyocytes, highlighting glycolysis, fatty acid uptake and β-oxidation, and mitochondrial acetyl-CoA entry into the tricarboxylic acid (TCA) cycle. Key transporters and enzymes are indicated. **b,** Heatmap showing expression of fatty acid uptake and β-oxidation–related genes across cardiomyocyte states, including CFLAR^{+} subclusters, HAND2^{+}, DES^{+}, NPPA_NPPB^{+}, SLC25A4^{+}, and DES_SYNPO^{+} cardiomyocytes. Values represent mean expression scaled per gene **c,** Heatmap of glutaminolysis and TCA cycle–associated genes across cardiomyocyte states, illustrating differential utilization of anaplerotic pathways. **d,** Dot plot of over-representation analysis (ORA) for differentially expressed genes (logFC: interval -3.5 to -2.5, top 150 genes). Enriched terms are dominated by mitochondrial respiration, oxidative phosphorylation, and ATP synthesis pathways. Dot size indicates gene set size; color denotes statistical significance (−log10 p-value). **e,** Conceptual schematic of core cell-cycle regulators and their activity across G1, S, G2, and M phases, including MYC, cyclins, CDKs, and mitotic regulators. **f,** Heatmap of cell-cycle regulator expression across cardiomyocyte states, revealing selective enrichment of G1/S and G2/M regulators in specific CFLAR^{+} subclusters relative to

other cardiomyocyte populations. **g,** Heatmap of ion channels, transporters, connexins, and receptors relevant for cardiomyocyte electrophysiology and intercellular coupling. Channels are grouped by functional class (e.g., HCN, Ca^{2+}, K^{+}, Cl^{-} channels, connexins). Mean expression is scaled per gene. **h,** Heatmap of genes involved in histone acetylation, histone/DNA methylation, chromatin remodeling, genome architecture, and nuclear stability across cardiomyocyte states, highlighting enhanced epigenetic and chromatin regulatory programs in $CFLAR^{+}$ cardiomyocytes. **i,** Heatmap summarizing higher-order functional programs across cardiomyocyte states, including metabolic maturation and mitochondrial programs, postnatal maturation and hypertrophy, lipid/cholesterol and inflammatory crosstalk, developmental/regenerative signaling axes, and xenobiotic/stress responses. **j,** Conceptual model contrasting diploid and polyploid cardiomyocytes. Diploid cardiomyocytes are characterized by preserved metabolic maturation, mitochondrial organization, and WNT antagonism (e.g., DKK3, SFRP1), whereas polyploid cardiomyocytes display activation of Hippo, WNT, TGFβ, and SHH signaling, altered genome architecture, and stress-adaptive transcriptional programs. **k**, TF Activity of CTCF within the PHLOWER estimated CM trajectory.

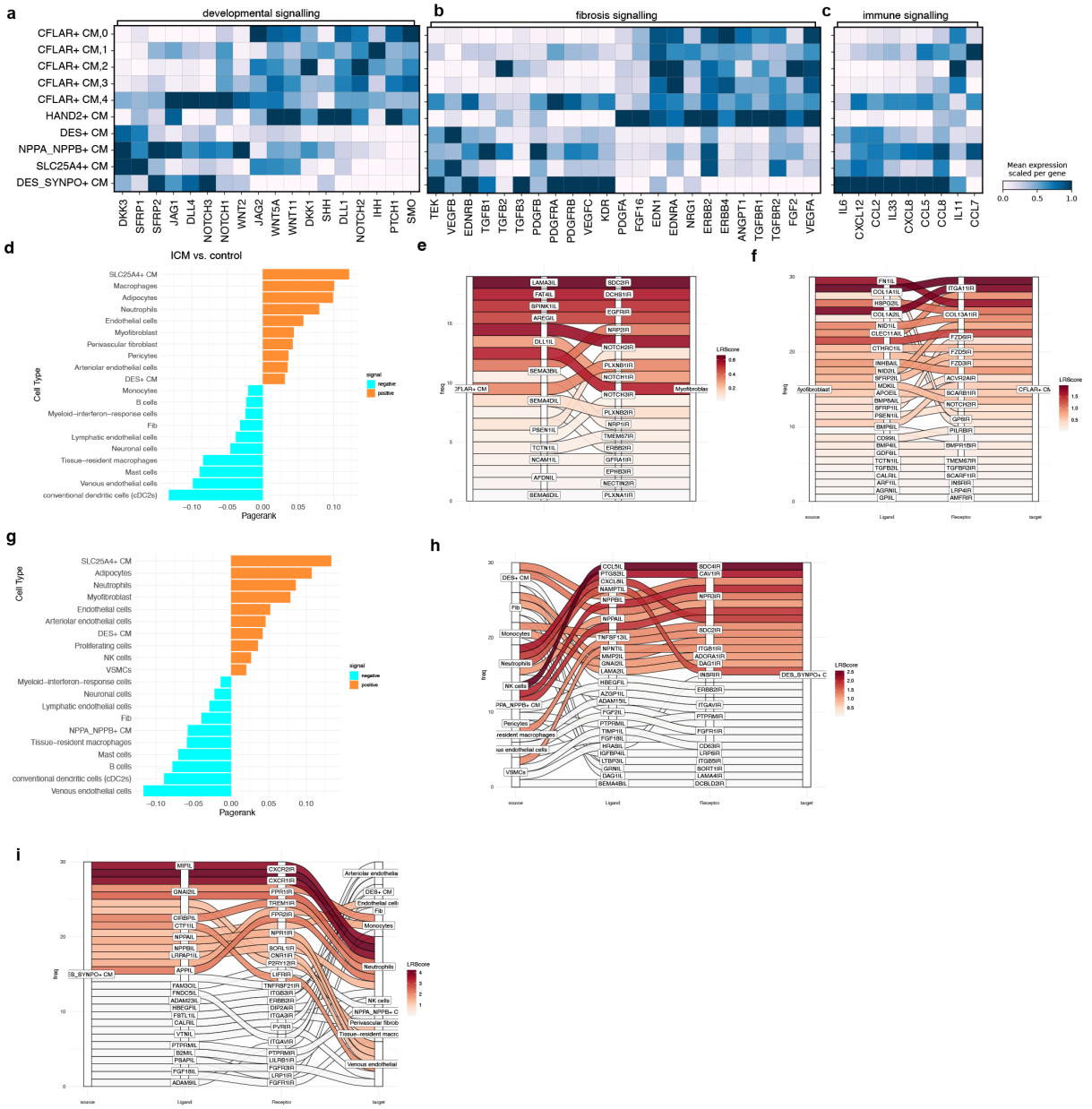

Extended Data Figure 8 Disease-specific intercellular signaling programs linking cardiomyocyte states to fibrosis and immune remodeling. a–c, Heatmaps showing mean scaled expression of pathway-associated genes across cardiomyocyte states. **a,** Developmental signaling pathways, including WNT, SHH, and NOTCH components, display selective activation in CFLAR^{+} and HAND2^{+} cardiomyocytes. **b,** Fibrosis-associated signaling genes (e.g. TGFβ, PDGF, VEGF, FGF pathways) highlight enhanced profibrotic communication potential of specific cardiomyocyte states. **c,** Immune signaling genes, including chemokines and cytokines, indicate differential immune-modulatory capacity across cardiomyocyte populations. **d,** PageRank analysis of cell–cell communication networks in ischemic cardiomyopathy (ICM) versus control. Positive values indicate increased signaling influence in disease, whereas negative values indicate reduced influence. **e–f,** Sankey plot with top ligand–receptor interaction highlighting ongoing CFLAR^{+}-myofibroblast specific communication relative to other cardiomyocyte states in ICM vs control. **e,** Sankey plot with top ligand-receptor interactions between CFLAR^{+} cardiomyocytes towards myofibroblasts, emphasizing fibrosis-related signaling axes. **f,** Reciprocal interactions from myofibroblasts, illustrating cardiomyocyte-driven profibrotic signaling. **g,** PageRank importance analysis of cell–cell communication changes in DCM versus control, highlighting cardiomyocyte subtypes and immune or stromal populations with altered network influence. **h,** Sankey diagram with top ligand-receptor interactions with DES_SYNPO^{+} as target cell in DCM versus control.

i, Sankey diagram with top ligand-receptor interactions with DES_SYNPO^{+} as source cell in DCM versus control.

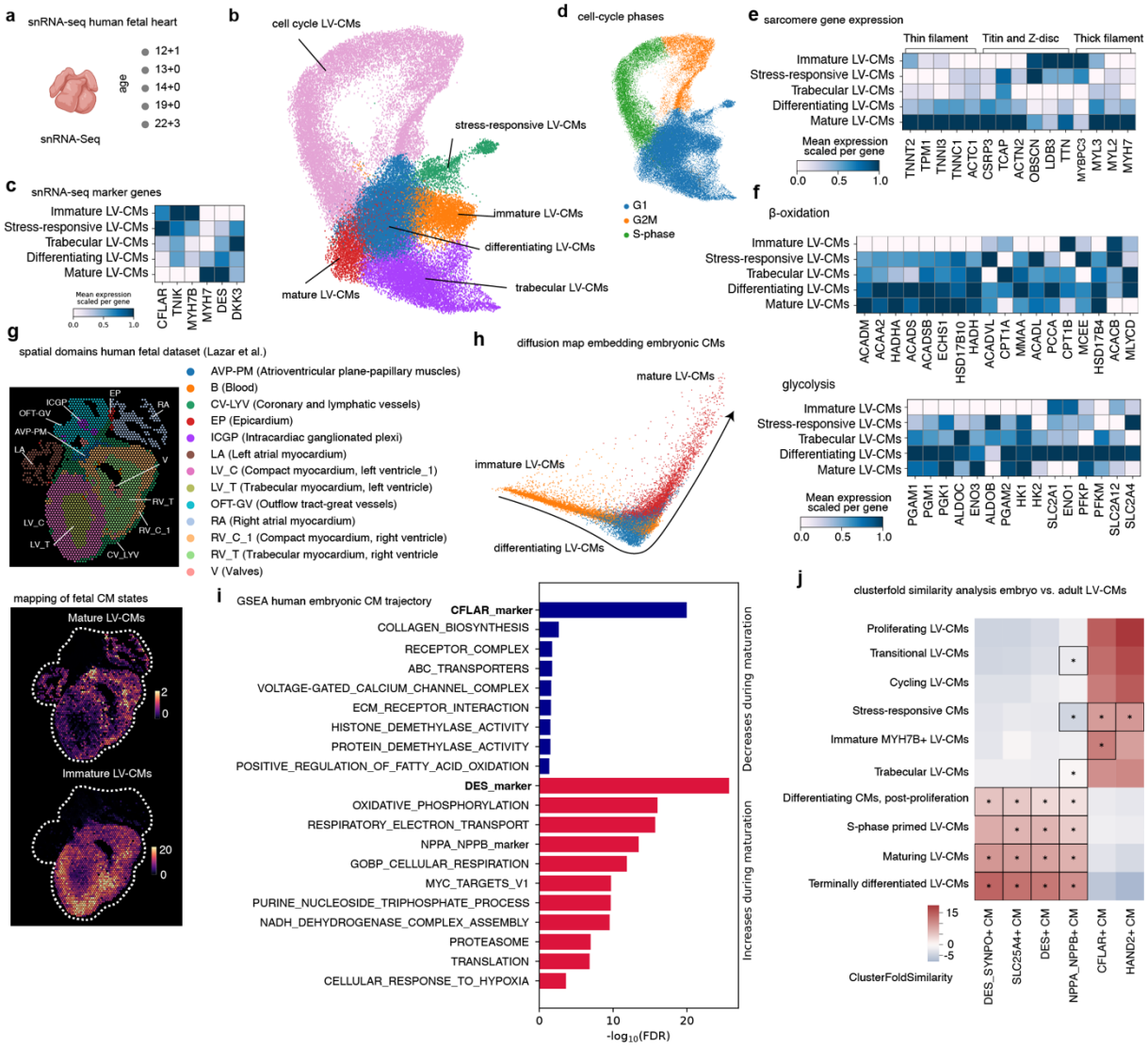

Figure 4 Single-nucleus and spatial dissection of human embryonic cardiomyocyte differentiation. a, Overview of human fetal heart samples profiled by snRNA-seq across developmental stages (12–22+ post-conception weeks, pcw). **b,** UMAP embedding of snRNA-seq data from human fetal hearts, revealing distinct cardiomyocyte (CM) populations including proliferating, cycling, differentiating, immature, stress-responsive, trabecular, and terminally differentiated left-ventricular (LV) CMs. **c,** Heatmap of selected marker genes defining major embryonic LV-CM states (scaled mean expression). **d,** Cell-cycle phase annotation of embryonic CMs projected onto the UMAP, highlighting G1, S-phase, and G2/M populations. **e,** Expression of sarcomeric gene modules (thin filament, titin/Z-disc, thick filament) across LV-CM maturation states. **f,** Metabolic gene expression programs associated with β-oxidation and glycolysis across LV-CM states. **g,** Reference spatial domains from the human embryonic heart dataset (Lazar et al.), annotated by anatomical and functional regions. Spatial mapping of embryonic CM states identified in this study onto the reference human embryonic heart sections, showing regional enrichment of immature, mature, and trabecular LV-CMs, alongside major non-CM lineages (estimated counts per Visium spot). **h,** Diffusion map embedding depicting the continuous differentiation trajectory from immature through differentiating to mature LV-CMs. **i,** Gene set enrichment analysis (GSEA) along the human embryonic CM trajectory, highlighting pathways decreasing (blue) or increasing (red) during maturation. **j,** Cluster-to-cluster similarity analysis comparing embryonic LV-CM states to adult human LV-CM populations, revealing selective correspondence between embryonic

differentiation states and adult CM phenotypes. Stars indicate significance (p-value <0.05) with an hypergeometric test.

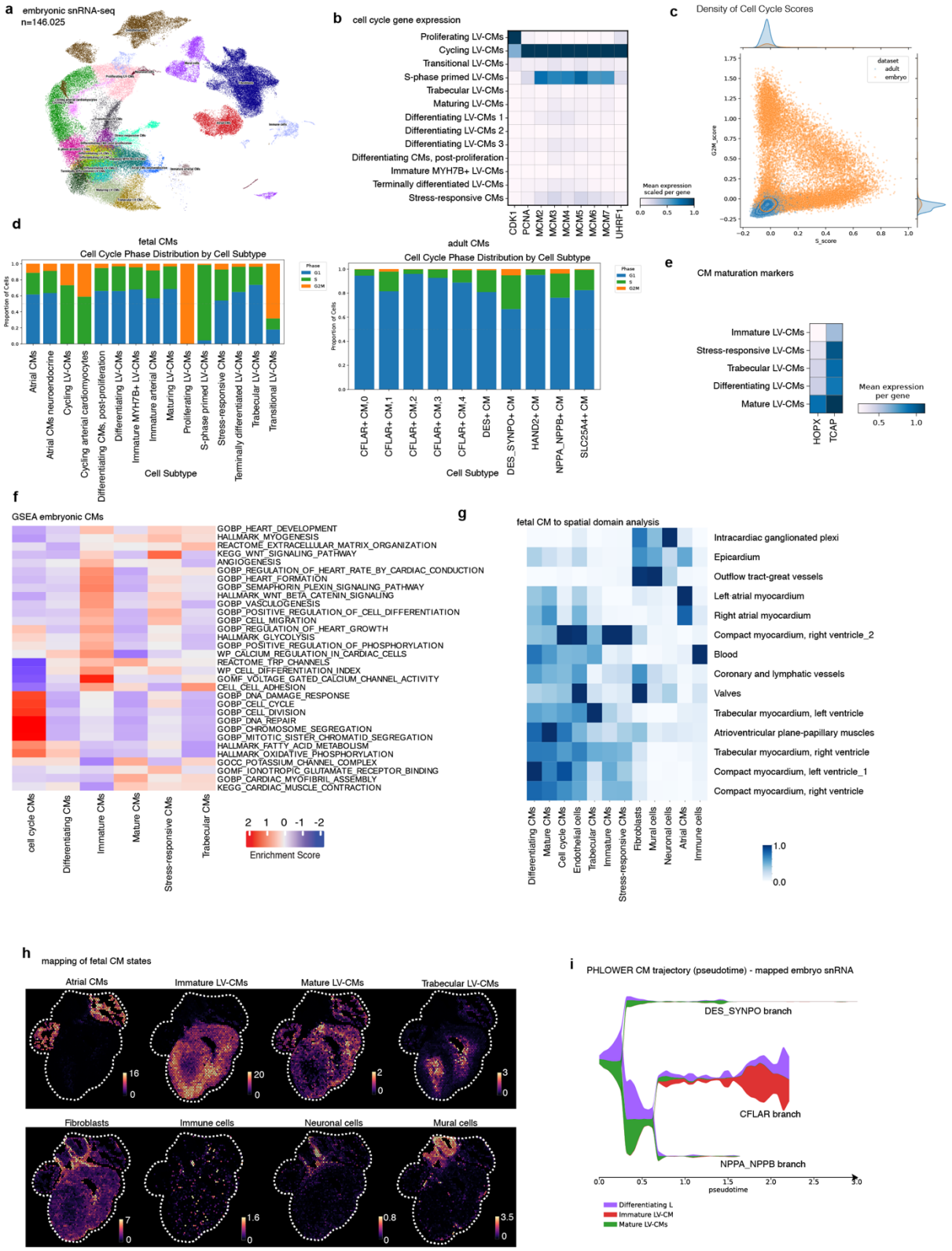

Extended Data Fig. 9 Cell-cycle activity and maturation trajectories of embryonic cardiomyocytes. a, UMAP of embryonic human snRNA-seq data highlighting cardiomyocyte differentiation states. **b**, Min-max scaled expression of canonical cell-cycle genes across embryonic LV-CM subtypes. **c**, Density and joint distribution of S- and G2/M-phase scores in embryonic versus adult cardiomyocytes. **d**, Cell-cycle phases across matched cardiomyocyte states in adult and embryonic datasets. **e**, Expression of cardiomyocyte maturation markers across embryonic LV-CM subsets. **f,** Gene set enrichment analysis (GSEA) of embryonic cardiomyocyte states highlighting developmental, metabolic, and cell-cycle programs. **g,** Quantitative association of embryonic CM states and non-CM

cell types with anatomical spatial domains, illustrating coordinated patterning of CM maturation with cardiac tissue architecture. **h,** Embryonic cell states mapped to Visium data (estimated counts per Visium spot) on a representative sample. **i,** PHLOWER trajectory with selected embryonic cardiomyocytes cells mapped onto adult CM branches, indicating immature LV-CMs to be related to the CFLAR branch.

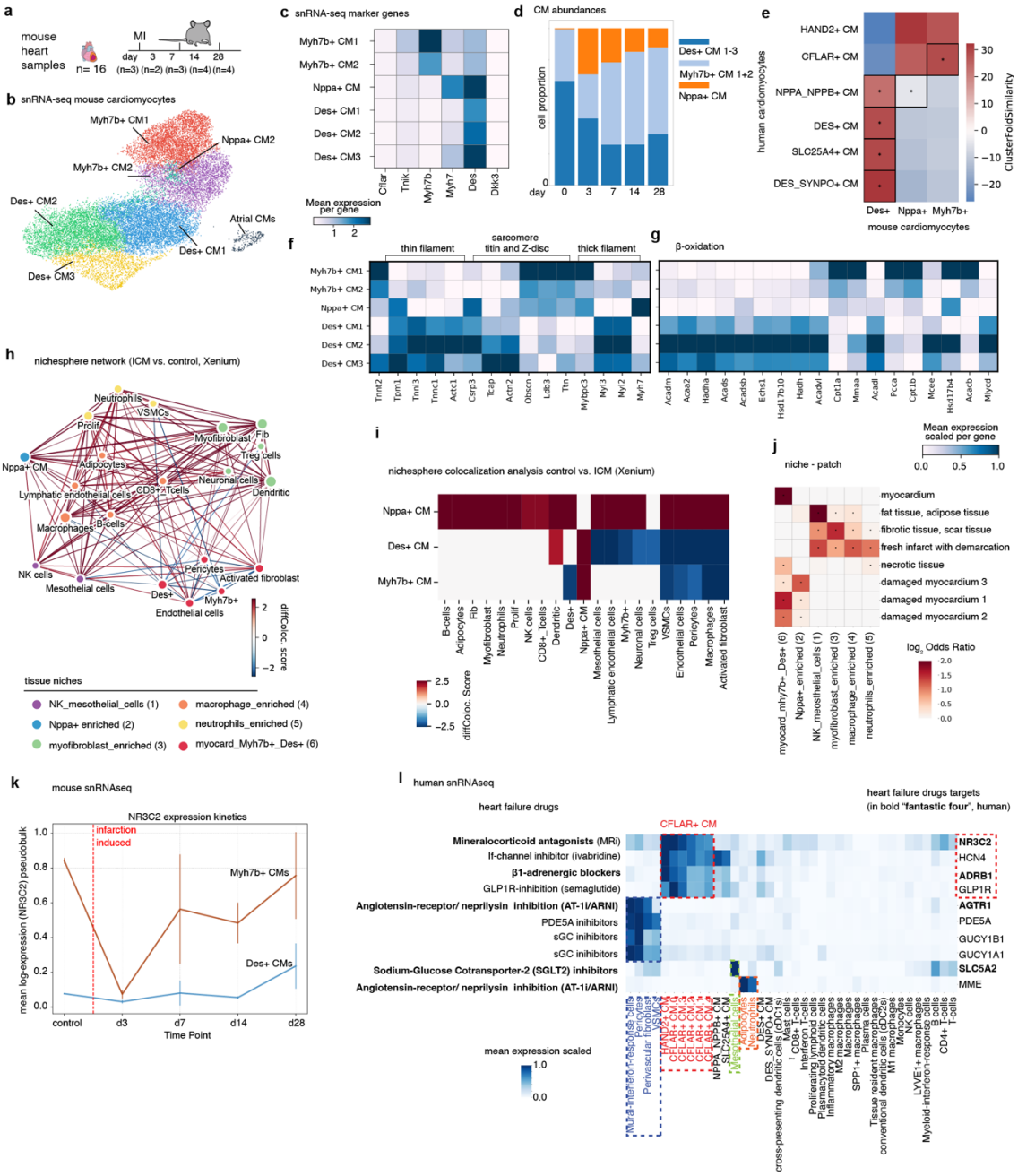

Figure 5 Spatiotemporal organization of cardiomyocyte states after myocardial infarction a, Experimental design and sampling scheme of murine hearts subjected to myocardial infarction (MI), with snRNA-seq performed at days 0, 3, 7, 14, and 28 post-MI. **b,** UMAP embedding of snRNA-seq profiles from murine cardiomyocytes, identifying Myh7b$^+$, Nppa$^+$, and Des$^+$ cardiomyocyte (CM) subclusters, as well as atrial CMs. **c,** Heatmap of marker gene expression defining CM subclusters, highlighting differential expression of contractile, stress-response, and cytoskeletal genes. **d,** Temporal dynamics of CM subcluster abundances following MI, showing early expansion of Nppa$^+$ CMs and progressive enrichment of Des$^+$ CM states during remodeling. **e,** Cross-species similarity analysis mapping murine CM subclusters to human CM states, including HAND2$^+$, CFLAR$^+$, NPPA/ NPPB$^+$, DES$^+$, SLC25A4$^+$, and DES_SYNPO$^+$ cardiomyocytes. **f,** Scaled mean expression of sarcomeric gene modules (thin filament, titin/Z-disc, thick filament) across CM subclusters, indicating progressive structural remodeling. **g,** Scaled mean expression of β-oxidation–related genes, revealing reduced oxidative metabolic signatures in Myh7b$^+$ and Nppa$^+$ CMs relative to Des$^+$ CM states. **h,** Nichesphere interaction network derived from Xenium spatial transcriptomics comparing ischemic cardiomyopathy (ICM) and control myocardium, highlighting CM-centered tissue niches enriched for immune, stromal, and vascular cell interactions. **i,** Differential spatial colocalization scores for CM subclusters with non-myocyte cell types

in ICM versus control hearts, indicating selective niche rewiring of Nppa^{+} and Des^{+} CMs. For **h** and **i**, only significant interactions are shown(adjusted Wilcoxon's rank sums test; p-value < 0.05). **j,** Enrichment of CM-associated tissue patches across anatomical and pathological regions, including fibrotic scar, infarct border zones, necrotic tissue, and damaged myocardium. Significance was determined by Fisher's exact test with adjusted p-values < 0.05. **k,** Temporal dynamics of heart-failure–relevant drug targets across murine CM states following MI. **l,** Expression landscape of clinically established heart-failure drug targets across human cardiac cell types, with the "fantastic four" therapeutic classes highlighted, demonstrating preferential target enrichment in distinct CM and non-CM compartments.

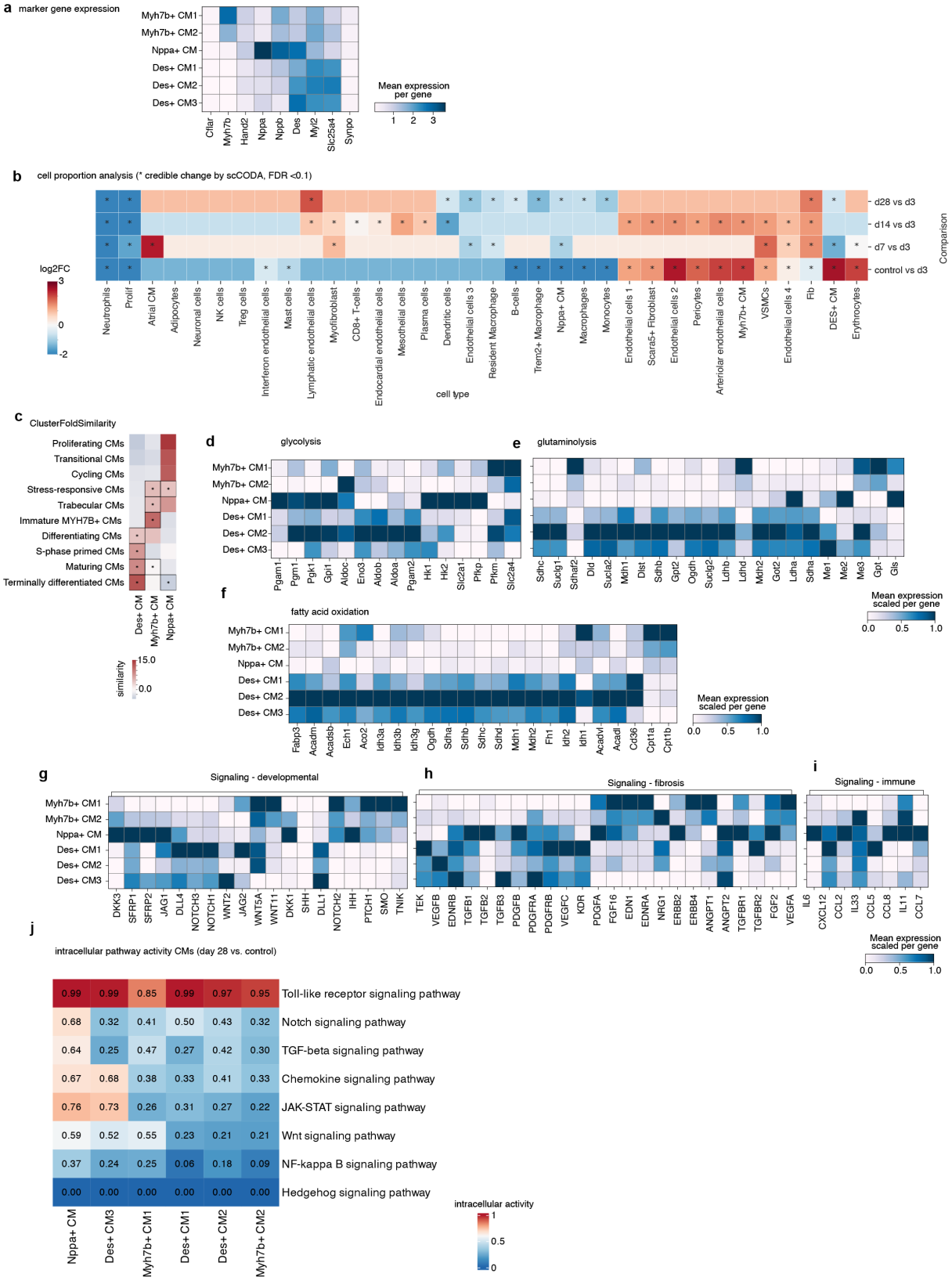

ED Figure 10 Cardiomyocyte state composition, metabolic rewiring, signaling programs, and spatial niches during disease progression in mice. a, Heatmap showing mean expression of selected cardiomyocyte (CM) marker genes across Myh7b$^+$, Nppa$^+$, and Des$^+$ CM subclusters, confirming transcriptional identity of polyploid (Myh7b$^+$, Nppa$^+$) and diploid (Des$^+$) CM states. Expression is scaled per gene. **b,** Differential cell proportion analysis across experimental conditions using scCODA. Heatmap indicates credible increases (blue) or decreases (red) in cell type abundance relative to control (FDR = 0.1). Asterisks denote statistically credible changes. Comparisons include control vs d3, d7 vs

d3, d14 vs d3, and d28 vs d3. **c,** Enrichment of CM differentiation and cell cycle–related gene signatures across CM states. Polyploid Myh7b$^+$ and Nppa$^+$ CMs show enrichment of immature, stress-responsive, and cycling programs, whereas Des$^+$ CMs align with terminal differentiation states. **d–f,** Heatmaps showing scaled mean expression of genes involved in **glycolysis** (d), **glutaminolysis** (e), and **fatty acid oxidation** (f) across CM subclusters. Polyploid CM states display increased glycolytic and glutaminolytic programs, while diploid Des$^+$ CM states retain higher fatty acid oxidation signatures. **g–i,** Expression of signaling pathway components across CM states. **g,** Developmental signaling pathways (e.g., WNT, NOTCH, Hedgehog). **h,** Fibrosis-associated signaling (e.g., TGF-β, PDGF, VEGF, EGFR). **i,** Immune-related signaling and chemokine expression. Polyploid CM states preferentially activate developmental and pro-fibrotic signaling programs. **j**, Heatmap of intracellular pathway activity scores in cardiomyocyte (CM) subtypes at day 28 post-injury compared with controls. Pathways include Toll-like receptor, Notch, TGF-β, chemokine, JAK–STAT, Wnt, NF-κB, and Hedgehog signaling. Values represent normalized pathway activity, with clustering revealing differential inflammatory and developmental signaling across CM states (Nppa$^+$, Des$^+$, and Myh7b$^+$ subsets).

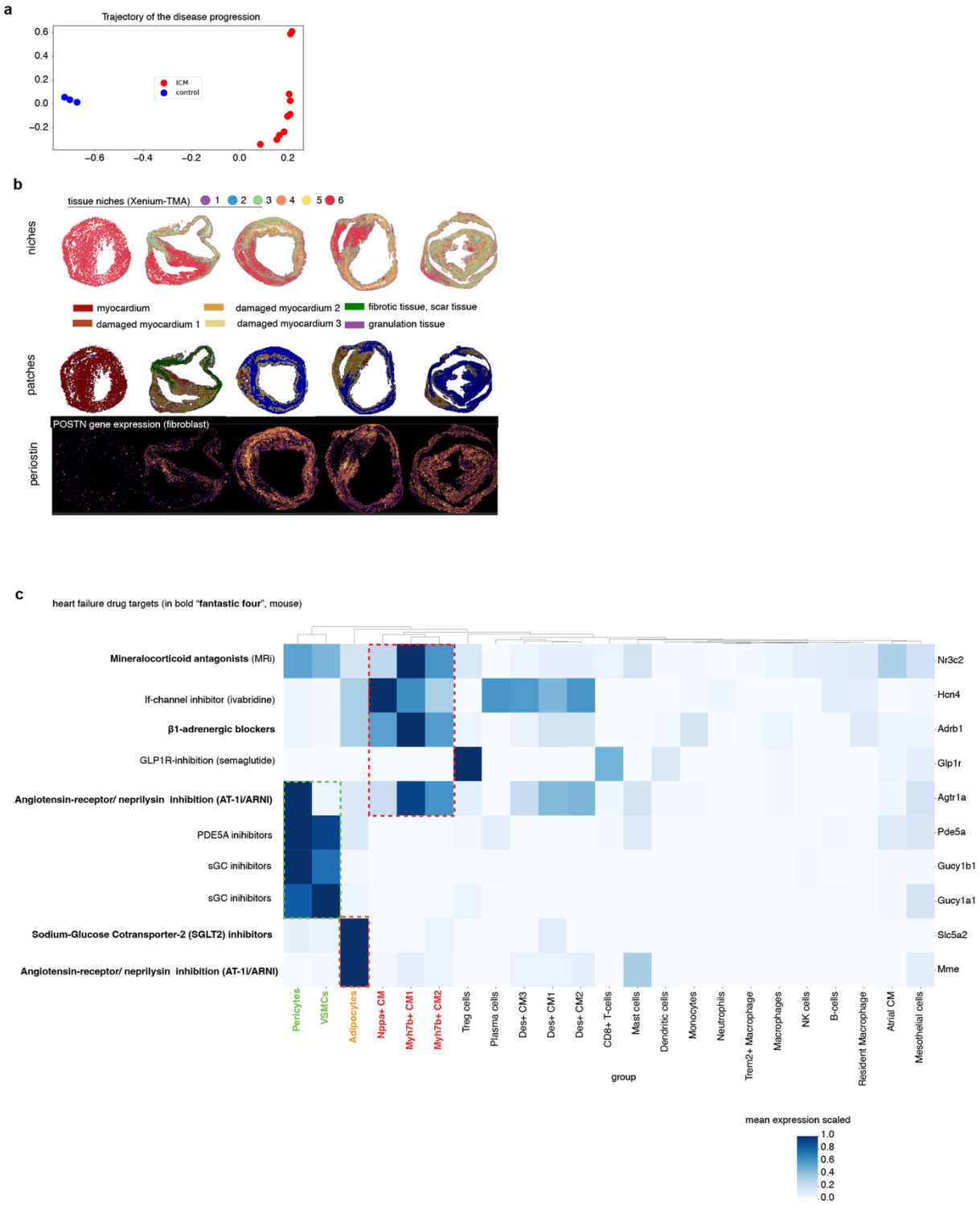

Extended Data Fig. 11 Spatial and transcriptional remodeling of cardiomyocyte states and therapeutic target engagement in ischemic cardiomyopathy. a, Low-dimensional embedding illustrating the trajectory of disease progression, separating control samples (blue) from ischemic cardiomyopathy (ICM; red), indicating a coordinated shift in global transcriptional states with disease. **b,** Spatial tissue organization inferred from five samples selected along the trajectory of **a**. Top: tissue niches (1–6) highlighting myocardium, damaged myocardium, fibrotic and scar tissue, and granulation tissue. Middle: spatial patches derived from unsupervised segmentation, reflecting recurrent micro-architectural patterns. Bottom: spatial expression of *Postn* in fibroblasts, illustrating fibrosis-associated gene expression across disease-affected regions. **c,** Cell type–resolved expression of major heart failure drug targets in mouse, including the "fantastic four" (β-blockers, MR antagonists, ARNI, and SGLT2

inhibitors; bold). Heatmap shows relative target gene expression across cardiomyocyte subtypes, vascular cells, adipocytes, and immune populations. Red dashed boxes highlight cardiomyocyte-enriched targets, while green dashed boxes indicate pericyte/VSMC-associated signaling nodes (e.g., PDE5A and sGC pathways), underscoring multicellular mechanisms of therapeutic action.

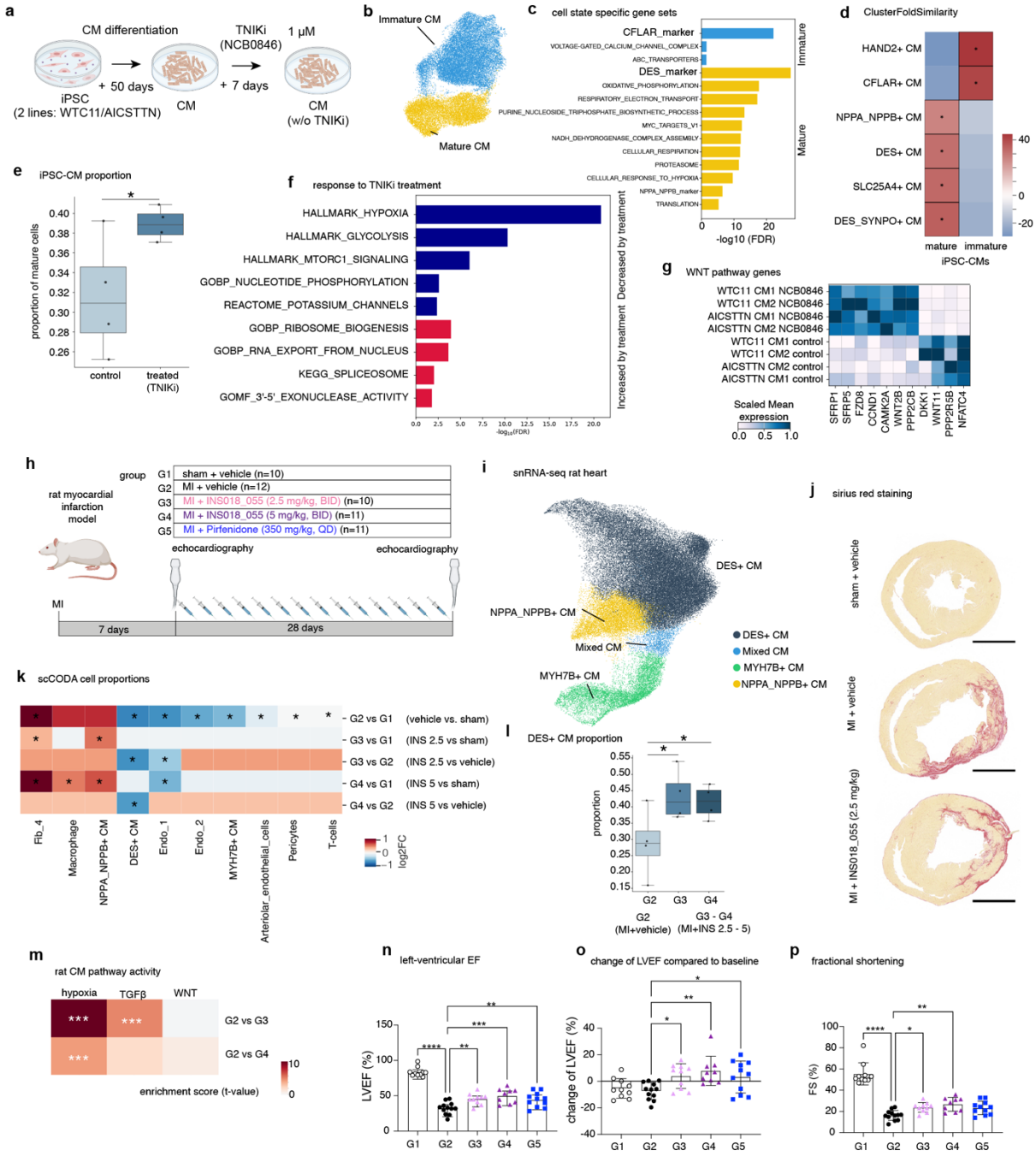

Fig. 6 TNIK inhibition promotes cardiomyocyte maturation and improves post-MI cardiac function. **a,** Experimental workflow for iPSC-derived cardiomyocyte (CM) differentiation and TNIK inhibition with NCB-0846. **b,** UMAP of iPSC-CMs showing segregation into immature and mature CM states. **c,** Gene set enrichment analysis highlighting immature (CFLAR-associated) versus mature (DES-associated) CM programs. **d,** Transcriptomic similarity between iPSC-CMs and adult clusters, color indicates ClusterFoldSimilarity, *p-value < 0.05 hypergeometric test. **e,** Increased proportion of mature CMs following TNIK inhibition in iPSC-CM, * indicates FDR < 0.1 for the scCODA abundance test. **f,** Pathways decreased or increased upon TNIK inhibition in iPSC-CMs. **g,** Expression of WNT pathway genes across control and TNIK-inhibited iPSC-CMs. **h,** Rat myocardial infarction (MI) study design and treatment groups. **i,** snRNA-seq of rat hearts identifying CM subpopulations after MI and treatment. **j,** Sirius Red staining and quantitative analysis demonstrating reduced fibrosis with TNIK inhibition, scale bars indicate 4 mm. **k)** Changes in cell abundance between treatment groups,* indicates FDR < 0.1 for the scCODA abundance test. **l)** Increased proportion of mature CMs following TNIK inhibition in rats , * indicates FDR < 0.1 for the scCODA abundance test. **m)** Compatarative

enrichment analysis of selected pathways. ***p-value < 0.001. **n-p),** Improved cardiac function following TNIK inhibition, including left ventricular ejection fraction, fractional shortening, ventricular mass, and wall thickness. Data are shown as mean ± s.e.m.; *p-value < 0.05, **p-value < 0.01, ***p-value < 0.001.

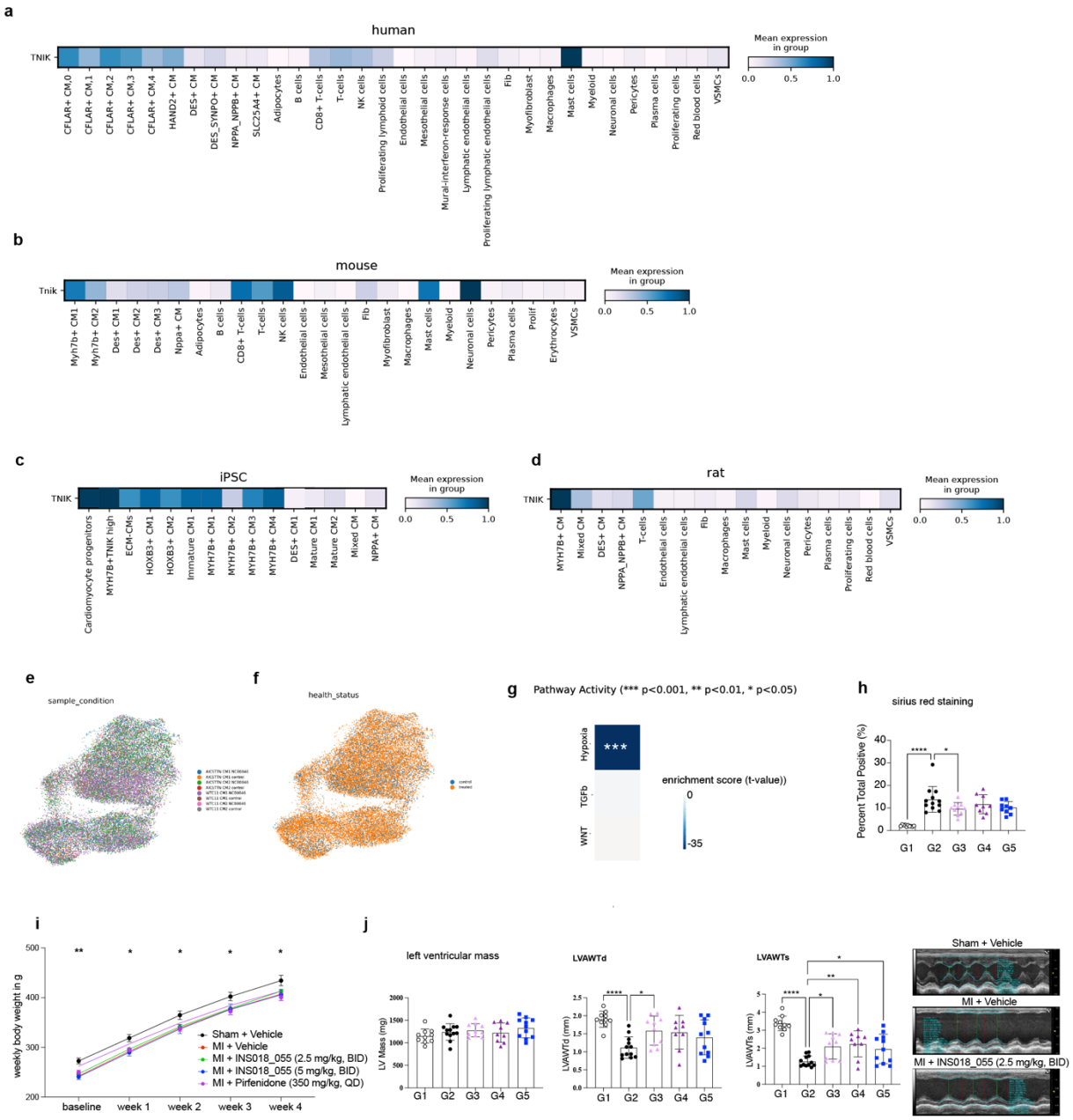

Extended Data Fig. 12 TNIK expression across species and models and functional effects of TNIK inhibition. a, Mean TNIK expression across human cardiac and non-cardiac cell types, highlighting enrichment in cardiomyocyte subpopulations, including CFLAR^{+} and HAND2^{+} cardiomyocytes, compared with stromal and immune compartments. **b,** Mean Tnik expression across mouse heart cell types, demonstrating conserved cardiomyocyte-biased expression relative to non-myocyte populations. **c,** TNIK expression across iPSC-derived cardiomyocyte differentiation stages and subtypes, with highest expression observed in immature and MYH7B^{+} cardiomyocyte states. **d,** Mean TNIK expression across rat cardiac cell populations, confirming cross-species conservation of cardiomyocyte-enriched TNIK expression. **e,** UMAP projection of iPSC cardiomyocytes colored by sample and experimental condition, showing robust integration across datasets. **f,** The same UMAP colored by health status, demonstrating overlap between control and diseased cardiomyocytes without condition-driven batch effects. **g,** Pathway enrichment scores inferred from cardiomyocyte transcriptomes of WTC11 and AICS-TTN iPSC-derived cardiomyocytes under control conditions or following TNIK inhibition (NCB-0846). *** p-value < 0.001 versus vehicle **i,** Weekly body weight trajectories following myocardial infarction (MI) and treatment with vehicle, INS018_055 (two doses), or pirfenidone. TNIK inhibition does not induce weight loss compared with vehicle or antifibrotic control. Data are shown as mean ± s.e.m.; * p-value < 0.05, ** p-value < 0.01 versus MI + vehicle. **j,**

Representative M-mode echocardiography images from sham-operated animals, MI + vehicle, and MI treated with INS018_055 (2.5 mg/kg, BID), illustrating improved cardiac contractile performance following TNIK inhibition.

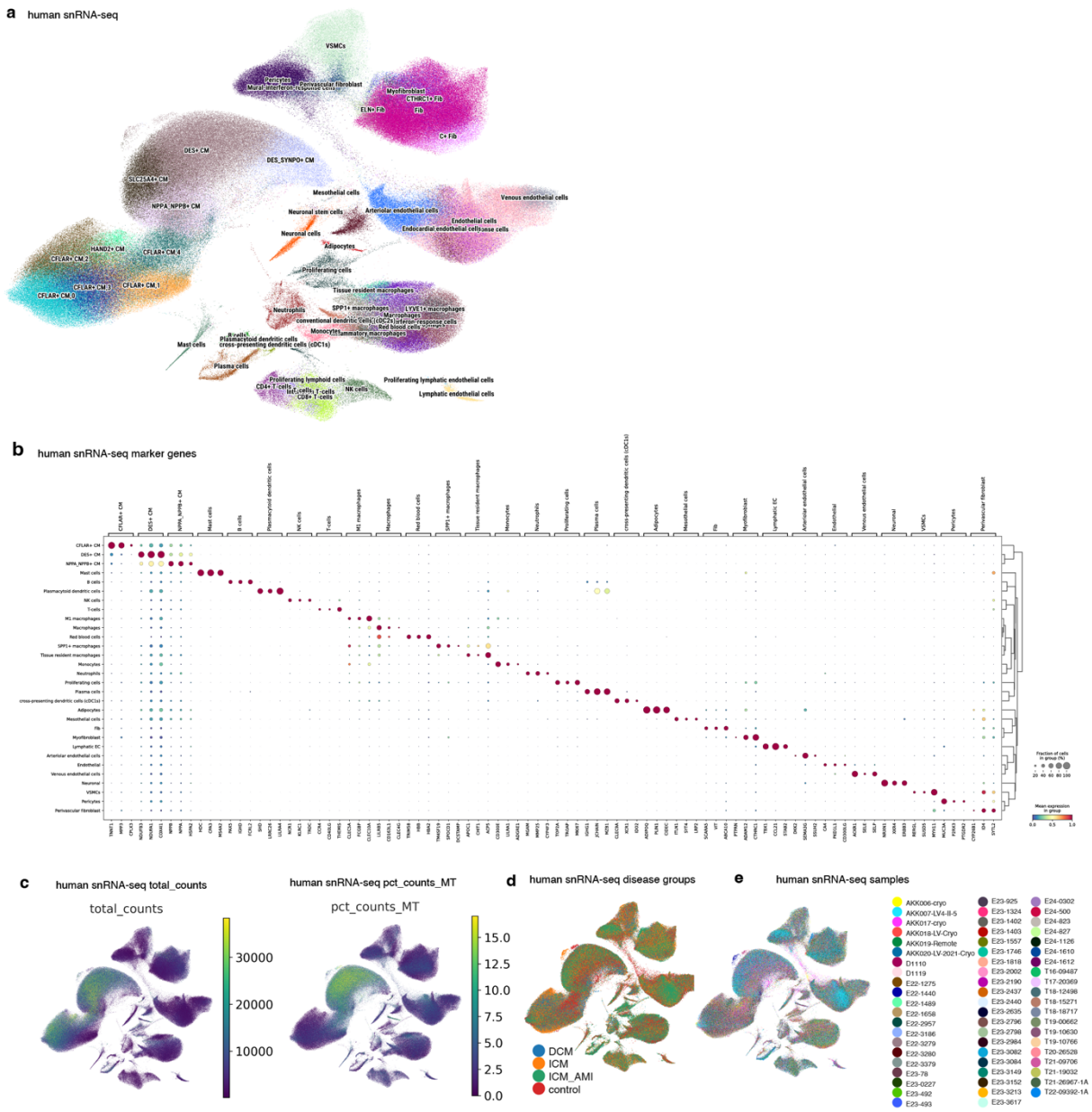

Supplementary Data Figure 1 Overview and quality control of the human cardiac snRNA-seq data **a,** Uniform Manifold Approximation and Projection (UMAP) of all nuclei profiled by single-nucleus RNA sequencing (snRNA-seq) from human cardiac tissue. Major cardiac cell types are annotated, including cardiomyocyte (CM) sub-states, fibroblast subsets, endothelial populations, vascular smooth muscle cells (VSMCs), immune cells, adipocytes, mesothelial cells, neuronal cells, and proliferating populations. **b,** Dot-plot showing canonical marker gene expression across annotated cardiac cell types identified in the human snRNA-seq dataset. Dot size represents the fraction of nuclei expressing the gene within each cell type, and color intensity indicates scaled average expression levels. Hierarchical clustering reflects transcriptional similarity between cell populations. **c,** Quality control metrics projected onto the UMAP embedding. Left: total UMI counts per nucleus (*total_counts*), illustrating sequencing depth distribution across cell populations. Right: percentage of mitochondrial transcripts (*pct_counts_MT*), indicating overall RNA integrity and low mitochondrial contamination across clusters. **d,** UMAP colored by disease group, including dilated cardiomyopathy (DCM), ischemic cardiomyopathy (ICM), ischemic cardiomyopathy with acute myocardial infarction (ICM_AMI), and non-failing control samples, demonstrating broad representation of disease states across all major cell types. **e,** UMAP colored by individual human samples, highlighting inter-sample integration and minimal batch effects following data harmonization.

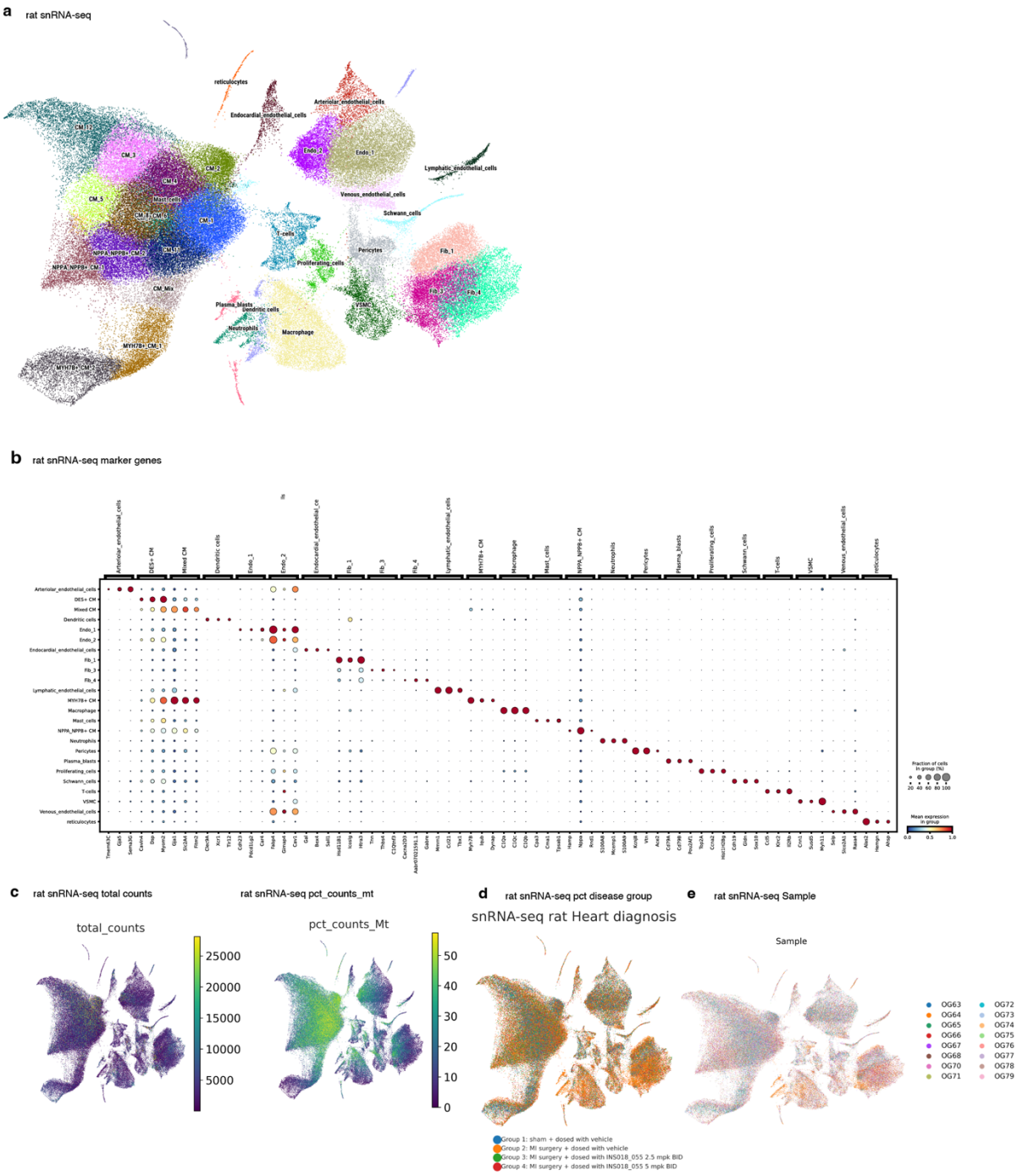

Supplementary Data Figure 2 Single-nucleus RNA-seq dataset and quality control rat a, Uniform Manifold Approximation and Projection (UMAP) of all nuclei profiled by single-nucleus RNA sequencing (snRNA-seq) from rat cardiac tissue. Major cardiac cell populations are annotated, including multiple cardiomyocyte (CM) sub-states, fibroblast subsets, endothelial cell types, vascular smooth muscle cells (VSMCs), pericytes, Schwann cells, immune populations, proliferating cells, and reticulocytes. **b,** Dot-plot showing expression of canonical marker genes used to annotate rat cardiac cell populations. Dot size represents the fraction of nuclei expressing each gene within a given cell type, while color intensity indicates scaled mean expression. Hierarchical clustering reflects transcriptional similarity among annotated cell types. **c,** Quality control metrics projected onto the UMAP embedding. Left: total UMI

counts per nucleus (*total_counts*), illustrating sequencing depth across rat cardiac cell populations. Right: percentage of mitochondrial transcripts (*pct_counts_mt*), indicating RNA quality and low levels of mitochondrial contamination across clusters. **d,** UMAP colored by experimental group, including sham-operated controls and myocardial injury groups with vehicle or pharmacological intervention, demonstrating balanced representation of experimental conditions across cell populations. **e,** UMAP colored by individual rat samples, highlighting inter-sample integration and minimal batch effects following data harmonization.

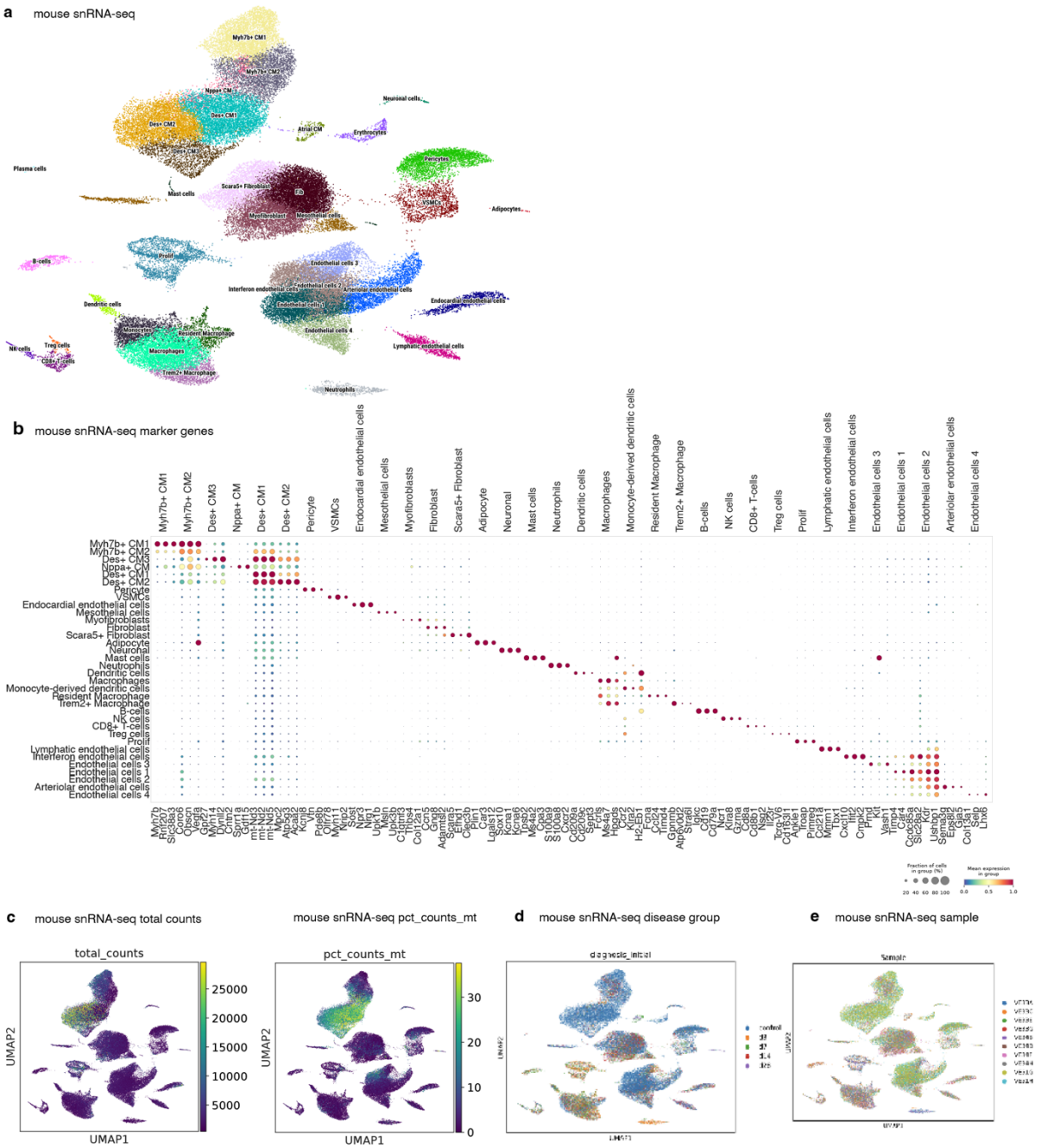

Supplementary Data Figure 3 Single-nucleus RNA-seq dataset and quality control mouse a, Uniform Manifold Approximation and Projection (UMAP) of all nuclei profiled by single-nucleus RNA sequencing (snRNA-seq) from rat cardiac tissue. Major cardiac cell populations are annotated, including multiple cardiomyocyte (CM) sub-states, fibroblast subsets, endothelial cell types, vascular smooth muscle cells (VSMCs), pericytes, Schwann cells, immune populations, proliferating cells, and reticulocytes. **b,** Dot-plot showing expression of canonical marker genes used to annotate rat cardiac cell populations. Dot size represents the fraction of nuclei expressing each gene within a given cell type, while color intensity indicates scaled mean expression. Hierarchical clustering reflects transcriptional similarity among annotated cell types. **c,** Quality control metrics projected onto the UMAP embedding. Left: total UMI counts per nucleus (*total_counts*), illustrating sequencing depth across rat cardiac cell populations. Right: percentage of mitochondrial transcripts (*pct_counts_mt*), indicating RNA quality and low levels of mitochondrial contamination across clusters. **d,** UMAP colored by experimental group and treatment condition, including sham-operated controls and myocardial injury groups with vehicle or pharmacological intervention, demonstrating balanced representation of experimental conditions across

cell populations.**e,** UMAP colored by individual mouse samples, highlighting inter-sample integration and minimal batch effects following data harmonization.

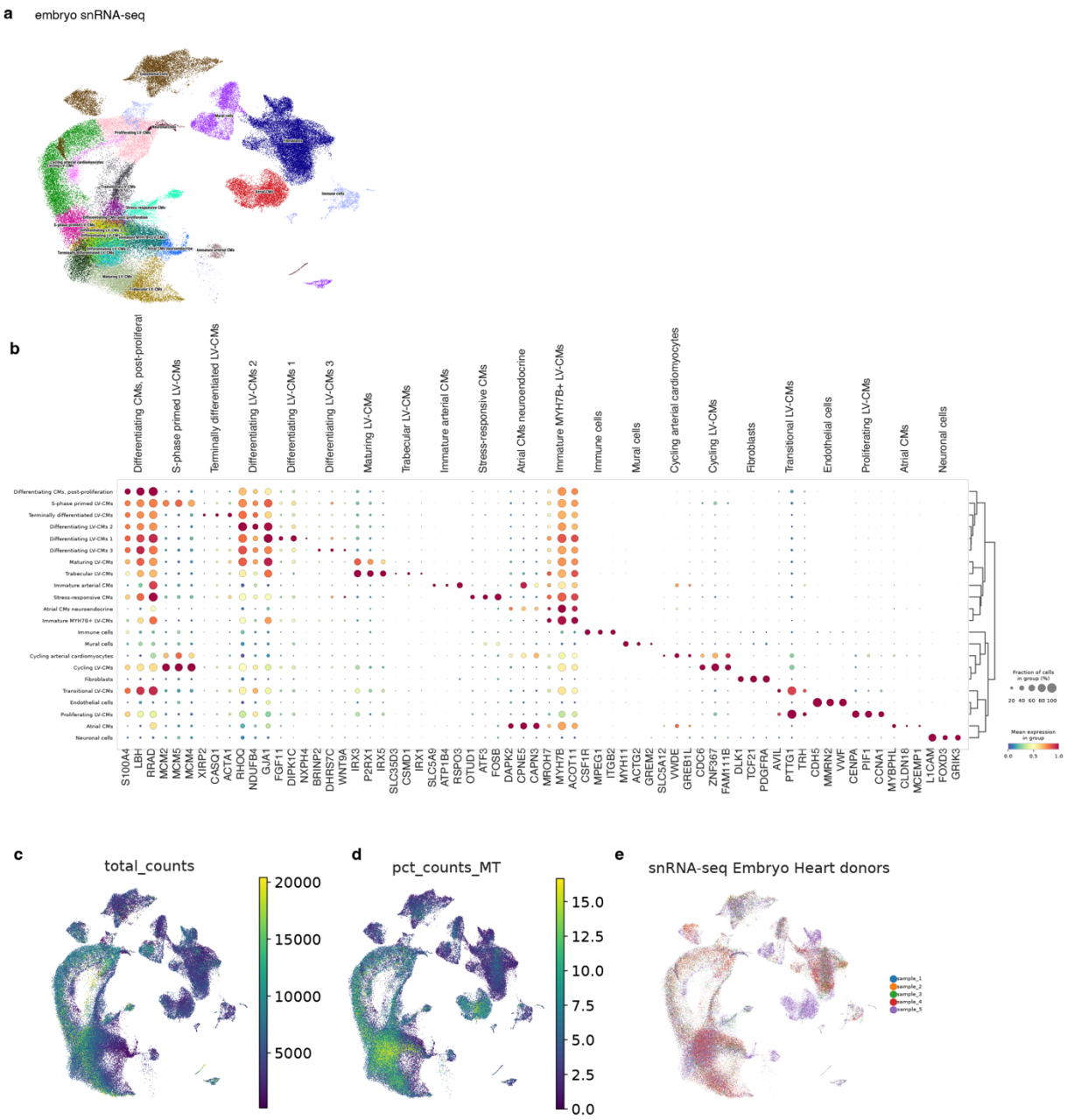

Supplementary Figure 4 Single-nucleus RNA-seq dataset and quality control human embryo a, Uniform Manifold Approximation and Projection (UMAP) of all nuclei profiled by single-nucleus RNA sequencing (snRNA-seq) from human embryo cardiac tissue. **b,** Dot-plot showing expression of canonical marker genes used to annotate rat cardiac cell populations. Dot size represents the fraction of nuclei expressing each gene within a given cell type, while color intensity indicates scaled mean expression. **c,** Quality control metrics projected onto the UMAP embedding. Total UMI counts per nucleus (*total_counts*), illustrating sequencing depth across rat cardiac cell populations. **d,** Percentage of mitochondrial transcripts (*pct_counts_mt*), indicating RNA quality and low levels of mitochondrial contamination across clusters. **e,** UMAP colored by snRNA-seq sample of the embryo human hearts.